Effect of Upstream Obstacles on Air Layer Regimes in a Turbulent Boundary Layer

An experimental study on the influence of obstacles' size and placement within a turbulent boundary layer on air lubrication.

Thibaut Wolfs

TU Delft

Effect of Upstream Obstacles on Air Layer Regimes in a Turbulent Boundary Layer

An experimental study on the influence of obstacles' size and placement within a turbulent boundary layer on air lubrication.

by

Thibaut Wolfs

Student Name	Student Number
Thibaut Wolfs	4556577

Daily Supervisor: Dr. Angeliki Laskari
Project Duration: September, 2023 - September, 2024
Faculty: Faculty of Mechaninical Engineering, Delft

TU Delft

Declaration

I, Thibaut Wolfs, confirm that this thesis, titled ”Effect of Upstream Obstacles on Air Layer Regimes in a Turbulent Boundary Layer”, is my own work. During writing and editing, I used AI tools to help with grammar and improve the clarity of the text. These tools were only used to check the writing and did not influence the research or the results in any way. All ideas and research presented here are my own.

Acknowledgements

First and foremost, I would like to thank my supervisor, Dr. Angeliki Laskari, for her constant support, guidance, and encouragement throughout this project. Her feedback and direction have been essential to the completion of this thesis.

I am also grateful to Lina Nikolaidou, Abirath Anand, and Abinash Mishra for their help and advice during the research process. Special thanks to Edwin Overmars for his assistance with the imaging, which was crucial for the experiments. I would like to specifically thank Jasper Ruijgrok for his help with the fabrication of the plate, as well as Gert Jan Mulder and his colleagues for their invaluable support with the LED panels, which played a key role in the success of the experiments.

Lastly, I want to express my appreciation to everyone who contributed in any way, whether directly or indirectly. Thank you all.

Abstract

Hydrodynamic drag significantly influences the fuel efficiency and operational performance of marine vessels. Gas Injection Drag Reduction (GIDR) techniques, such as Bubble Drag Reduction (BDR), Transitional Layer Drag Reduction (TLDR), and Air Layer Drag Reduction (ALDR), have shown promise in reducing skin friction drag by introducing gas into the boundary layer. However, the influence of hull protrusions, such as sacrificial anodes and fouling, on these techniques remains poorly understood. This research addresses the question: ***How do the placement and dimensions of upstream cylindrical obstacles affect the formation and stability of gas phases (bubbly, transitional, and air layer) in a turbulent boundary layer (TBL)?*** To investigate this, protrusions are represented as cylindrical objects placed upstream of the gas injector, exploring their effects on the gas injection regimes in a TBL.

The study examines three gas injection regimes: bubbly, transitional, and air layer. In the bubbly regime, the focus is on bubble morphology and velocity distributions. The transitional regime investigates non-wetted areas and air layer morphology. For the air layer regime, the study examines the length and stability of the air layer near the injector. Image processing techniques are used to distinguish the air layer from the surrounding fluid, providing accurate assessments of the properties of the air layer.

The results demonstrate that cylindrical obstacles have a significant effect on the gas phases. In the bubbly regime, they alter bubble morphology and velocity, producing localized velocity peaks. In the transitional regime, obstacles lead to the formation of non-wetted areas and funnel-shaped regions. For the air layer regime, although the length of the air layer remains mostly unaffected, its stability near the injector is disrupted by upstream obstacles due to wake-induced instabilities. These findings highlight the critical role of obstacle placement and dimensions in shaping gas injection regimes.

Future research is needed to enhance understanding in areas such as the integration of velocity measurements (e.g., Particle Image Velocimetry), widening the experimental field of view to capture more comprehensive flow dynamics, and exploring the impact of various obstacle sizes and geometries. These investigations will be crucial for refining gas injection drag reduction strategies and advancing practical marine applications.

Contents

List of Figures

List of Tables

Nomenclature

Abbreviations

Abbreviation	Definition
ALDR	Air Layer Drag Reduction
Anw	Non-wetted Area
BDR	Bubble Drag Reduction
CFD	Computational Fluid Dynamics
FOV	Field of View
ISA	International Standard Atmosphere
LED	Light-Emitting Diode
PIV	Particle Image Velocimetry
Re	Reynolds Number
TBL	Turbulent Boundary Layer
ZOI	Zone of Influence

Symbols

Symbol	Definition	Unit
Anw	Non-wetted area	[-]
C_f	Skin friction coefficient	[-]
D	Obstacle diameter	[m]
d_B	Bubble diameter	[m]
f	Frequency	[Hz]
h	Obstacle height	[m]
h^+	Non-dimensional obstacle height	[-]
l^*	Length scale	[m]
L_{air}	Length of the air layer	[m]
$\overline{L}_{\text{air}}/D$	Non-dimensional air layer length	[-]
Q_{air}	Air flow rate	[l/min]
Re	Reynolds number	[-]
Re_D	Reynolds number based on cylinder diameter	[-]
Re_k	Reynolds number based on roughness height	[-]
Re_τ	Reynolds number based on friction velocity	[-]
Rex	Reynolds number based on distance from the leading edge	[-]
St	Strouhal number	[-]
U_∞	Free-stream velocity	[m/s]
U_b	Streamwise bubble velocity	[m/s]
U_k	Velocity at tripping roughness height	[m/s]
V	Velocity	[m/s]
W_b	Spanwise bubble velocity	[m/s]
z_{gap}	Spanwise gap between ZOI edges	[m]
δ	Boundary layer thickness	[m]
δ_{99}	Boundary layer thickness at 99% of U_∞	[m]
κ	Von Kármán constant	[-]
μ	Dynamic viscosity	[Pa·s]

Symbol	Definition	Unit
ν	Kinematic viscosity	[m^2/s]
ρ	Density	[kg/m^3]
σ	Surface tension	[N/m]
τ	Shear stress	[Pa]
τ_s	Surface shear stress	[Pa]
θ	Momentum thickness	[m]
u_τ	Friction velocity	[m/s]
y^+	Non-dimensional wall-normal coordinate	[-]

1

Introduction

Reducing hydrodynamic drag stands as a critical pursuit in the maritime industry, impacting the efficiency and performance of ships and watercraft. This resistance to movement through water significantly influences fuel consumption, making drag reduction an important element for achieving energy savings and meeting emission regulations. In line with the International Maritime Organization's (IMO) and the European Union's directives, there is a global commitment to reduce greenhouse gas (GHG) emissions by 80%–95% by 2050 (Jinghzen and Hanwei 2017; Psaraftis and Kontovas 2020). A substantial portion of hydrodynamic drag is attributed to skin friction, which accounts for 60%–70% of a vessel's total drag. As a result, reducing skin friction drag becomes a primary target in efforts to enhance ship performance and reduce both fuel consumption and emissions (Larsson, Raven, and Paulling 2010; Ceccio, Perlin, and Elbing 2012).

To address this, various drag reduction techniques have been developed, broadly categorized into passive and active methods. Passive techniques, such as advanced coatings and biomimetic surfaces, aim to reduce drag without external energy input (Ahmadzadehtalatapeh and Mousavi 2015; Domel et al. 2018). In contrast, active methods, such as gas injection drag reduction (GIDR), involve manipulating the flow around the vessel using external energy. GIDR is particularly promising as it introduces gas into the boundary layer to create a lubricating air layer along the hull, significantly reducing frictional resistance (Kim 2003).

A critical aspect of optimizing GIDR is understanding the interactions between the turbulent boundary layer (TBL), where most drag forces originate, and the gas layer. The introduction of gas into the TBL alters its dynamics, particularly in the log layer, where coherent structures such as low-speed streaks and vortical motions are prevalent. However, the effectiveness of this technique can be complicated by the presence of obstacles on a ship's hull, such as sacrificial anodes, hull fins, and fouling like algae and barnacles. These obstacles may disrupt the interactions between the gas layer and the TBL by causing flow separation, vortex shedding, and turbulent wakes, potentially reducing the overall drag reduction achieved.

While previous research has provided insights into the interaction between microbubbles and the TBL, a significant research gap remains in understanding how upstream obstacles, specifically circular cylindrical obstacles, influence the formation and stability of the air layer. For instance, Tan and Longmire (2017) studied the recovery of vortex packet organization in turbulent boundary layers perturbed by cylindrical arrays, demonstrating the complexities involved in wake recovery and flow stability. However, the specific interaction between such obstacles and air layer regimes within the TBL remains unexplored. This thesis seeks to fill this gap by investigating how the placement and dimensions of circular cylindrical obstacles affect the air layer, with a focus on experimental analysis. By studying the streamwise-spanwise plane (x-z), this research will explore the complex dynamics between the TBL, the air layer, and the obstacles, aiming to optimize configurations for practical marine applications.

The primary research question guiding this thesis is:

"How does the placement and the dimensions of upstream circular cylindrical obstacles affect the formation and characteristics of different gas phases (bubbly, transitional, air layer) in a turbulent boundary layer?"

To address this question, the thesis will investigate the following subquestions:

1. "How do the height and distance of upstream circular cylindrical obstacles from the injector influence the formation and behavior of the bubbly regime, particularly in terms of bubble morphology and velocity distributions in a turbulent boundary layer?"
2. "How do the height and distance of upstream circular cylindrical obstacles from the injector affect the transitional regime, specifically in relation to the stability and structure of the air layer in a turbulent boundary layer?"
3. "How do the height and distance of upstream circular cylindrical obstacles from the injector impact the air layer regime, particularly with regard to its length and the formation of breakups near the injector in a turbulent boundary layer?"

The structure of this thesis begins with Chapter 2, which provides the theoretical background and a comprehensive literature review, covering turbulent boundary layer theory and the current understanding of gas injection techniques, with a discussion on how circular cylindrical obstacles influence flow dynamics. Chapter 3 details the methodology, including the experimental setup and procedures used to study the impact of these obstacles on air layer formation. Chapter 4 describes the image processing techniques applied to the experimental data, crucial for extracting meaningful information from the observations. Chapter 5 presents and analyzes the experimental results, emphasizing the interactions between obstacles, the turbulent boundary layer, and the air layer, and includes a thorough discussion of these findings. Finally, Chapter 6 concludes the thesis by summarizing the key findings, discussing their broader implications, and suggesting potential directions for future research.

2

Literature Review

This chapter provides a comprehensive overview of the theoretical background and current research on modifying turbulent boundary layers (TBLs) through gas injection techniques. The chapter begins with a brief review of the state-of-the-art drag reduction techniques, which are categorized into passive and active methods. This overview sets the stage for a more in-depth examination of boundary layers (BLs), particularly TBLs and their coherent structures, which play a significant role in the drag forces acting on a vessel. Understanding these structures is crucial because they directly influence how gas or air layers interact with the TBL, thereby affecting drag reduction.

Given that gas injection drag reduction is primarily applied to marine vessels, which often encounter protrusions and fouling on their hulls, it is essential to explore the flow around obstacles to gain a deeper understanding of these interactions. Therefore, this literature review will pay particular attention to cylindrical objects, serving as models for typical hull obstacles. The review then shifts focus to the detailed exploration of gas injection drag reduction techniques, specifically Bubble Drag Reduction (BDR) and Air Layer Drag Reduction (ALDR), examining how these methods work by altering the behavior of air and bubble layers within the TBL.

The review concludes by identifying a significant research gap: the impact of upstream obstacles on the formation and stability of air layers within the TBL, particularly within the streamwise-spanwise plane (x-z). This gap underscores the necessity for the current research, which aims to provide new insights into the interactions between air layers, TBLs, and upstream obstacles, ultimately guiding the development of more effective drag reduction strategies.

2.1. State of the art: Drag reduction techniques

Drag is a significant force that opposes the motion of an object through a fluid, affecting energy efficiency and operational costs, particularly in the maritime industry. According to Larsson, Raven, and Paulling (2010), friction drag represents approximately 70% of the total resistance encountered by maritime vessels. Thus, effective drag reduction strategies are important to improve operational efficiency and promote environmental sustainability in maritime transport. This section presents an overview of the latest drag reduction techniques, which are vital to reducing energy consumption and mitigating greenhouse gas emissions. These techniques are categorized into two main types: passive and active drag reduction strategies.

2.1.1. Passive Drag Reduction Techniques

Passive drag reduction techniques use inherent properties and design features to minimize drag without the need for external energy input. One of the primary methods is the optimization of vessel shapes to achieve streamlined flow, significantly reducing turbulence and BL separation, thus lowering drag forces. A prominent example is the bulbous bow, an extension located at the ship's bow that modifies the wave patterns surrounding the hull, thereby decreasing drag. In addition, the use of specialized coatings and materials that reduce surface friction has proven effective. In particular, bio-inspired

surfaces, such as those mimicking shark skin, utilize riblet textures to alter the fluid dynamics at the surface, thus decreasing resistance (Domel et al. 2018). These passive approaches are beneficial due to their low maintenance and sustainable advantages, offering long-term benefits without ongoing energy expenditures (Yifeng, Yuan, and Bai 2017; Stenzel, Wilke, and Hage 2010).

2.1.2. Active Drag Reduction Techniques

Active drag reduction techniques require external energy inputs or control mechanisms to effectively manage and minimize drag. These methods are particularly valuable in dynamic environments where real-time adjustments to drag levels are essential. Active techniques are crucial in various industries, including the aviation, automotive, and maritime sectors. One significant method that is used in the maritime sector involves manipulating the BL to optimize flow characteristics, thereby substantially reducing drag. Kim (2003) provides a comprehensive overview of successful strategies for controlling the TBL and achieving drag reduction. Prominent examples include BL suction, vortex generators, and air jets. This thesis focuses on the gas injection drag reduction technique, discussed in detail in Section 2.4.

2.2. Boundary layers

he study of fluid motion, particularly in boundary layers (BL), is crucial to understanding various fluid dynamics processes. The Navier-Stokes equations provide the foundational mathematical framework for modeling these processes, but they have limitations when applied to complex flows. Ludwig Prandtl's BL theory, introduced in the early twentieth century, simplified the analysis of fluid dynamics by dividing the flow into two distinct regions: the outer flow and the inner flow, known as the BL.

In the outer flow, viscous effects are negligible, and the flow is often treated as inviscid and irrotational. In contrast, within the BL, which is a narrow zone close to solid surfaces, viscous forces become significant, and the flow adheres to surfaces. In this region, fluid properties such as velocity, pressure, and turbulence transition from their values at the surface to those in the free stream.

The synergy of the BL approximation with the Navier-Stokes equations has become a cornerstone for solving complicated flows. The effectiveness of the BL approximation hinges on the crucial assumption that the BL thickness is exceedingly thin. This thickness, δ_{99}, is generally described as the distance from the wall to the location where the velocity attains 99% of the velocity in the outer flow region. In particular, the thickness of the BL varies with distance x, as illustrated in Figure (2.1). The thickness of the BL on a flat plate can be calculated using the Blasius solution Equation (2.1) if it is laminar. If the BL is turbulent, it should be calculated using Equation (2.2). In these equations, ν is the kinematic viscosity, x is the length of the BL and U_∞ is the free-stream velocity.

$$\delta_{99} = 4.92\sqrt{\frac{\nu x}{U_\infty}} \tag{2.1}$$

$$\delta_{99} = 0.37x\left(\frac{U_\infty x}{\nu}\right)^{-1/5} \tag{2.2}$$

The Reynolds number, denoted as Re and defined in Equation (2.3), is a non-dimensional number representing the ratio of inertial forces to viscous forces within a fluid. It is a crucial parameter that governs BL flow. The method for calculating the Reynolds number can vary depending on the physical situation or the characteristics of the flow. For instance, when considering flow through a pipe, L might be the diameter of the pipe, while for flow over an airfoil, L would be the chord length of the airfoil. These variations ensure that the calculation accurately reflects the dominant physical scales and flow dynamics specific to each scenario. The thickness of the BL can be calculated using Equations (2.1) and (2.2). Equation (2.1) is used for a laminar BL and Equation (2.2) for a TBL.

$$Re = \frac{\rho U_\infty L}{\mu} = \frac{U_\infty L}{\nu} \tag{2.3}$$

At a certain critical Reynolds number, which is approximately $Re_{x,cr} \approx 10^5$, small disturbances in the flow over a flat plate start to grow, which changes the behavior of the BL. It transitions from being laminar to becoming turbulent. The BL is fully turbulent at the transition Reynolds number, $Re_{x,transition} \approx 3 \times 10^6$. This is visualized in Figure (2.1). Given that the flow beneath a ship's hull typically involves Reynolds numbers surpassing 10^9, this paper will specifically focus on TBLs.

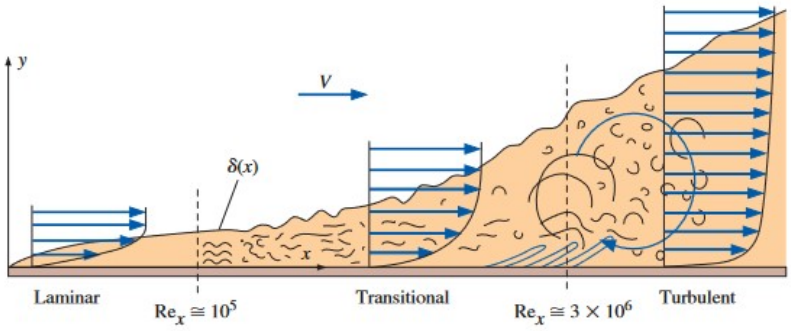

Figure 2.1: Transition of the laminar BL over a flat plate into a fully TBL (White 2011)

.

2.2.1. Turbulent boundary layers

Turbulent boundary layers (TBLs) are characterized by complex interactions between fluid layers with varying velocities and spatial scales, leading to the formation of vortices and irregularities that contribute to the chaotic nature of the flow. This turbulence within boundary layers is driven by several key mechanisms, each playing a significant role in shaping the flow dynamics.

One significant source of turbulence is the Kelvin-Helmholtz Instability, which occurs at the interface between the faster-moving outer layer of the boundary layer and the slower-moving layer near the surface. The resulting velocity differences create large-scale eddies that contribute significantly to the overall turbulence. Another source of turbulence is wall roughness; irregularities or roughness on a surface disrupt the smooth flow of fluid, increasing friction and intensifying turbulence.

Pressure gradients also contribute to turbulence within boundary layers. Variations in pressure along the surface of a solid object disturb the flow, forcing the fluid to adapt and leading to increased turbulence. Additionally, turbulence present in the incoming flow, known as free stream turbulence, can amplify the turbulence within the boundary layer. This effect is especially relevant in engineering applications, where external factors like atmospheric turbulence or ocean currents can significantly influence flow dynamics.

Distinct from laminar boundary layers, TBLs exhibit unique characteristics, particularly in their streamwise mean velocity distribution. This profile arises due to the specific structure of the TBL, where increased momentum near the wall allows the boundary layer to handle stronger adverse pressure gradients without separating. However, this also leads to higher wall shear stress, τ_w, which is a major contributor to drag. Understanding wall shear stress is critical for studying wall-bounded turbulence, as the average wall shear stress, $\bar{\tau}_w$, determines the friction velocity, u_τ, and the inner length scale of turbulent motions, or wall unit, l^*, as shown in Equation (2.4).

$$u_\tau = \sqrt{\frac{\bar{\tau}_w}{\rho}} \quad \text{and:} \quad l^* = \frac{\nu}{u_\tau} \tag{2.4}$$

A TBL can be divided into several regions, which will be examined in detail in Section 2.2.1.

Turbulent boundary layer regions

In earlier studies, researchers often represented the mean velocity profile in a turbulent channel or flat plate flow using a $1/n$th power law, where n was typically set to 7 (Nieuwstadt, Boersma, and Westerweel 2016). To further analyze the characteristics of such flows, the TBL is often divided into four

distinct regions based on equations of motion and physically reasonable closure models (Nieuwstadt, Boersma, and Westerweel 2016). These regions include the core region, logarithmic layer, buffer layer, and viscous sublayer. The positions of these layers, relative to each other and the wall, are illustrated in Figure (2.2).

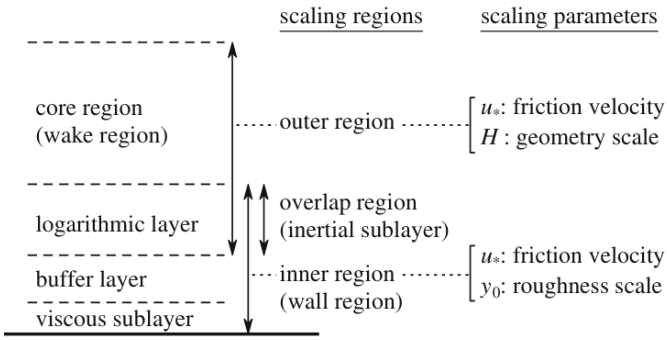

Figure 2.2: Scaling regions in turbulent wall flow (Nieuwstadt, Boersma, and Westerweel 2016).

The primary scaling regions are the outer layer and the inner layer. In the outer layer, the scaling parameters are the wall friction velocity, u_τ, and the geometry scale, H, where $u_\tau = \sqrt{\frac{\tau_s}{\rho_0}}$. τ_s represents the wall shear stress. In the inner region, the scaling parameters are the wall friction velocity, u_τ, and the roughness scale, y_0. A third scaling region, the inertial sublayer, exists where the inner and outer regions intersect. This alignment is achieved by introducing wall units, represented by dimensionless variables: y^+ and u^+, indicating the normalized length and velocity scale, as detailed in Equation (2.5).

$$y^+ = y\frac{u_\tau}{\nu} \quad \text{and:} \quad u^+ = \frac{\bar{u}}{u_\tau} \tag{2.5}$$

These wall units are used to further segment the scaling regions. Near the wall, we encounter the viscous sublayer, where turbulent stresses are negligible, and $y^+ = u^+$. This sublayer holds for $y^+ < 5$. Moving outward, the logarithmic profile dominates for $y^+ > 30$ until $y \leq 0.2\delta$. In this range, the velocity profile follows a logarithmic pattern, commonly referred to as the 'log-law,' as shown in Equation (2.6). The intermediate region, known as the buffer layer, is valid for $5 < y^+ < 30$, where both viscous stress and turbulent shear stress play significant roles.

$$U^+ = \frac{1}{\kappa}(\ln(y^+) + B) \tag{2.6}$$

To understand how these regions affect TBLs, we now turn to an exploration of coherent structures within this complex flow setup. These structures, such as vortices and eddies, play a crucial role in shaping momentum, heat transfer, and turbulent kinetic energy generation in turbulent flows. Investigating these structures builds on the foundational understanding of TBL regions, helping us unravel the intricate workings of turbulent flows.

Coherent structures in turbulent boundary layers

Turbulence is often viewed as random and chaotic, but certain structures exhibit organization and persistence over time. These structures, which vary in size from large-scale patterns spanning the entire boundary layer to smaller formations, are responsible for energy transport and transfer within the boundary layer and contribute to the production of turbulent kinetic energy. In the following sections, we will examine some of these structures to enhance our understanding of TBLs.

Vortical structures

Vortical structures, such as hairpin vortices—a concept introduced by Theodorsen (1952)—are key coherent structures in TBLs. Hairpin vortices form during the bursting process, which is visualized in

Figure (2.3). This process is characterized by localized bursts of intensified turbulence, triggered by the instability and non-uniformity of turbulent flow. The bursting process includes distinct events: ejection (Q2) and sweep (Q4). Ejection events involve the upward movement of low-speed fluid from near the wall towards the outer layer, creating low-speed streaks (discussed further in Section 2.2.1). The legs of a hairpin vortex align with these low-speed streaks, while the head, with higher vorticity concentration, lies at a higher wall-normal position and moves faster downstream than its legs. This difference in speed stretches the vortex. After a hairpin vortex forms, a sweep event often follows, characterized by the downward movement of faster-moving fluid towards the wall, contributing to overall turbulence and momentum transfer (Adrian 2007).

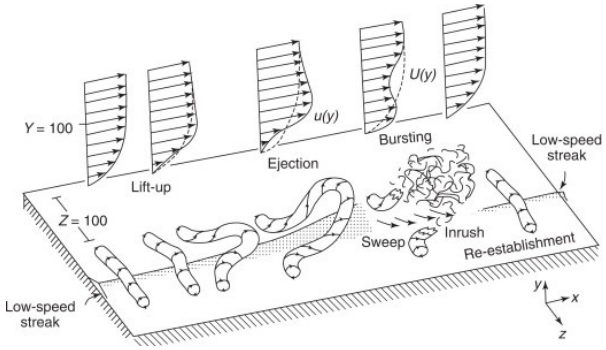

Figure 2.3: Schematic of the turbulent bursting process (Allen 1985).

Low-speed streaks

Low-speed streaks are integral components of TBLs and have been extensively studied in fluid dynamics by researchers such as Kline et al. (1967), Schoppa and Hussain (2002), and Adrian (2007). These streamwise-oriented regions of decreased flow velocity play a significant role in shaping turbulence near walls. It is important to distinguish between near-wall low-speed streaks, which are narrower and shorter, and those in the logarithmic region, which are part of longer, meandering features. Some of the first visualizations of near-wall low-speed streaks were made by Kline et al. (1967), as shown in Figure (2.4). These streaks are formed during the bursting process in ejection events, characterized by the upward movement of low-speed fluid.

Understanding low-speed streaks is crucial due to their connection with wall shear stress distribution. While studies by Adrian (2007) and Schoppa and Hussain (2002) have provided insights into the characteristics and generation of turbulent structures near the wall, further research is needed to understand how low-speed streaks influence momentum transfer between near-wall and outer fluid layers.

Low-speed streaks also affect skin friction drag by altering the velocity profile near the surface. As fluid flows over an object, these streaks modify the distribution of shear stress on the surface. Drag reduction strategies often target manipulating these streaks. By controlling or altering them, significant drag reduction can be achieved. Therefore, a comprehensive understanding of low-speed streaks, especially in different regions of the TBL, is essential for optimizing flow and reducing drag.

Long meandering features

Long meandering features, often referred to as ”superstructures,” represent coherent and elongated structures within TBLs. These features exhibit extended streamwise velocity fluctuations and persist over large spatial scales. Hutchins and Marusic (2006a) identified a zone where these meandering features persist, particularly in the logarithmic and lower wake regions of TBLs. These superstructures can extend beyond 20δ, where δ represents the boundary layer thickness.

These structures play a significant role in turbulent flow dynamics, particularly due to the spanwise inhomogeneity they introduce. Hutchins and Marusic (2006b) observed that these features are not only present in laboratory studies but also extend to the atmospheric surface layer (Phillips 2003). The spanwise variation they introduce creates localized zones of varying velocity, which can significantly affect downstream flow behavior, especially when interacting with obstacles.

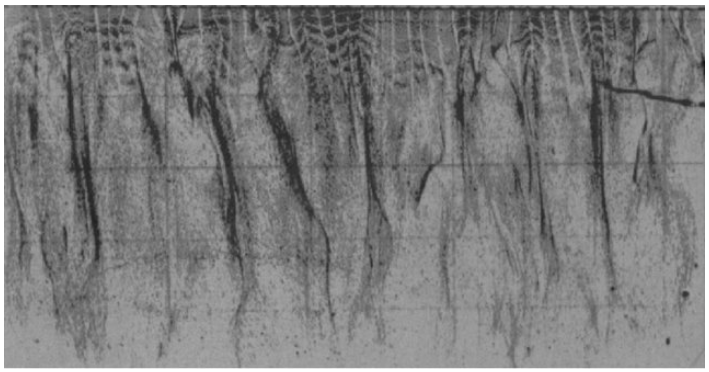

Figure 2.4: Hydrogen bubble visualization, x-z plane view of low-speed streaks; flow is from top to bottom (Kline et al. 1967).

Ganapathisubramani, Longmire, and Marusic (2003) highlighted that these superstructures contribute substantially to Reynolds shear stress, particularly in the logarithmic region of the TBL. This shear stress and associated spanwise inhomogeneity become critical when obstacles are added to the flow. For instance, when an obstacle is introduced, the pre-existing inhomogeneity due to these features can interact with the obstacle, leading to complex downstream flow patterns.

J.C. Del Álamo and J. Jiménez (2003) observed similar superstructures in pipe flows, emphasizing their generality across different turbulent flow configurations. The interaction between these large-scale structures and obstacles can have significant implications for air injection strategies. The spanwise inhomogeneity, combined with the disruption caused by an obstacle, may influence the distribution and effectiveness of air injection downstream, potentially altering drag reduction effectiveness or mixing efficiency. Understanding these long meandering features is essential for optimizing flow control strategies, such as air injection in TBLs.

2.3. Flow around an obstacle

The effectiveness of gas injection techniques like Bubble Drag Reduction (BDR) and Air Layer Drag Reduction (ALDR) heavily relies on the stability and maintenance of air and bubble layers within the TBL. However, the presence of obstacles on a ship's hull, such as sacrificial anodes, hull fins, or biological fouling, can significantly disrupt these layers. Understanding the flow dynamics around these obstacles is crucial for optimizing the application of gas injection techniques in practical marine environments.

This section focuses on the flow around bluff bodies, particularly cylinders, which serve as representative models for various hull obstacles. These obstacles can alter the TBL and the formation of air or bubble layers, potentially affecting the overall drag reduction achieved. By examining the phenomena of flow separation, vortex shedding, and turbulent wakes associated with cylinders, this section aims to provide insights into how such disruptions occur and how they might be mitigated in the context of gas injection drag reduction strategies.

In fluid dynamics, the study of flow separation around bluff bodies like cylinders reveals intricate interactions between the fluid and the body it flows around. Unlike streamlined bodies, which are designed to minimize resistance and drag, bluff bodies have broad, non-streamlined shapes that induce significant flow separation. As fluid flows over these bodies, a boundary layer forms immediately at the surface, encountering a high-pressure region at the front and decreasing pressure toward the rear. When the boundary layer faces an adverse pressure gradient strong enough to overcome the flow's momentum, it detaches from the surface, marking the flow separation point (White 2011). This separation creates a turbulent wake, which is a major source of drag due to the mixing of the turbulent flow with lower pressure regions compared to the undisturbed flow.

The pressure difference between the front and back of the cylinder generates a drag force that opposes the direction of motion. Additionally, the turbulent nature of the wake leads to vortex shedding, where swirling vortices are alternately shed from either side of the cylinder. The dynamics of this flow separation are influenced by factors such as the Reynolds number, the cylinder's shape, and the flow

conditions. The Strouhal number (St), a dimensionless number describing the frequency of vortex shedding relative to the cylinder's characteristic length and the flow velocity, is used to characterize this phenomenon. The equation for the Strouhal number is given in Equation (2.7), where f_s is the shedding frequency, and D is the cylinder diameter. The Strouhal number helps predict the vortex shedding frequency and understand flow-induced vibrations.

$$St = \frac{f_s D}{U_\infty} \tag{2.7}$$

$$Re_D = \frac{\rho U_\infty D}{\mu} = \frac{U_\infty D}{\nu} \tag{2.8}$$

The Reynolds number for a cylinder, Re_D, can be calculated using Equation (2.8), where D is the cylinder diameter. The wake and separation pattern are strongly dependent on Re_D. At $Re_D \leq 5$, no flow separation occurs, and the streamlines differ from those in an inviscid fluid due to viscous forces that cause them to spread further apart downstream. In the Reynolds number range of $5 - 15 \leq Re_D \leq 40$, flow separates from the rear of the cylinder, forming a symmetric pair of vortices whose length increases linearly with the Reynolds number. As Re_D increases further ($40 < Re_D < 150$), the wake becomes unstable, initiating vortex shedding. Initially, one vortex breaks away, followed by the other, due to nonsymmetric pressure, forming a laminar periodic wake known as the Von Karman vortex street. Von Karman demonstrated that the vortex pattern in this street follows a specific mathematical relationship.

In the range of $150 < Re_D < 300$, periodic irregular disturbances appear in the wake, indicating a transitional flow that gradually becomes turbulent with increasing Reynolds number. The subcritical range ($300 < Re_D < 3 \cdot 10^5$) is characterized by the laminar boundary layer separating at about 80 degrees downstream from the front stagnation point, leading to strong, periodic vortex shedding.

As Re_D increases further, the flow enters the critical regime. Here, the laminar boundary layer separates on the front side, forming a separation bubble, and reattaches on the cylinder surface. This reattachment is followed by a turbulent boundary layer, moving the separation point to about 140 degrees downstream, significantly reducing the drag coefficient. For $Re_D \geq 6 \times 10^5$, the transition from laminar to turbulent occurs in a non-separated boundary layer, with the transition point shifting upstream.

The transitional range ($3 \cdot 10^5 < Re_D < 3.5 \cdot 10^6$) is marked by three-dimensional effects that disrupt the regular shedding process and broaden the spectrum of shedding frequencies. In the supercritical range ($Re_D > 3.5 \cdot 10^6$), regular vortex shedding that is narrower re-establishes with a turbulent boundary layer on the surface (Blevins 1990; ANSYS, 2024). All of this is visualized in Figure (2.5).

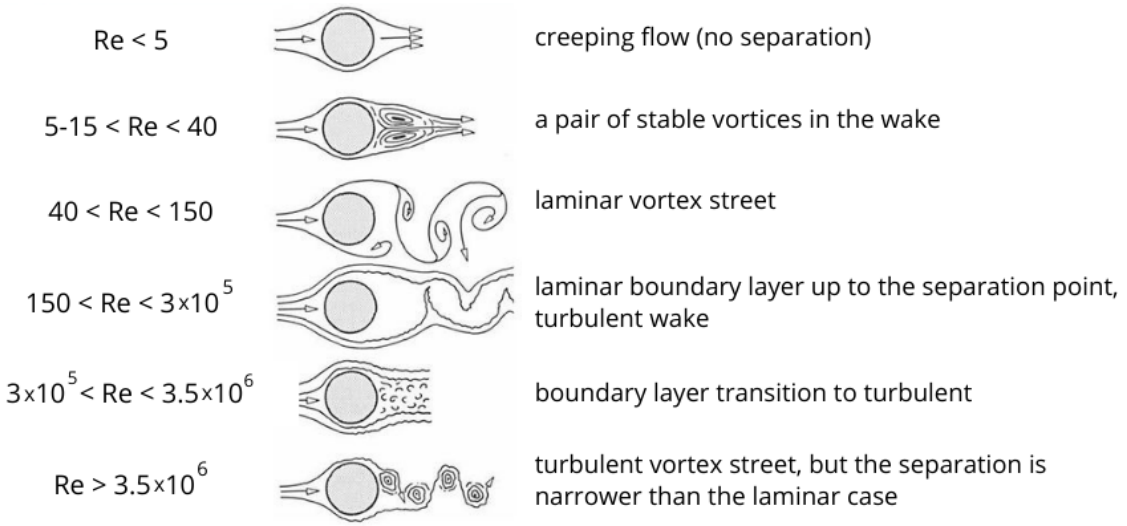

Figure 2.5: Effect of Reynolds number of a cylinder on the separation and wake behind a cylinder (ANSYS, 2024).

This study involves placing a finite circular cylinder in the TBL mounted on a wall, also called a finite wall-mounted cylinder (FWMC). In this study, the ratio between the height and the TBL thickness is $h/\delta < 0.1$. Reviewing existing research on this topic is crucial because the flow conditions within a TBL add further complexities, and these complexities can significantly impact the formation and stability of air layers used in drag reduction techniques.

2.3.1. Finite wall-mounted cylinder

The flow surrounding a finite wall-mounted cylinder (FWMC) is characterized by complex 3D flow patterns influenced by the interaction between the free end of the cylinder and the bottom wall. These interactions significantly alter the quasi-periodic Von Karman vortex shedding observed in infinite or 2D cylinders, making the flow physics around FWMCs more intricate. In this study, the cylinder will be fully immersed in a TBL where $\delta >> h$, which introduces additional complexities that are less prominent in uniform flow or thin TBL scenarios.

The flow behavior around FWMCs is governed by three main parameters: the Reynolds number (Re_D), the aspect ratio (h/D), and the submergence ratio (h/δ). The Reynolds number, already discussed in Section 2.3, plays a crucial role in determining the wake structure and vortex shedding patterns around the cylinder. While the general effects of Re_D are well-documented for 2D cylinders, FWMCs experience modifications due to 3D effects. These effects arise from the finite length of the cylinder and its interaction with the wall and free end, leading to a more complex wake structure than that observed in 2D cases.

The aspect ratio (h/D) of the cylinder is another critical parameter influencing the wake dynamics. Prior research has indicated that at certain aspect ratios, the typical Von Karman vortex shedding pattern is disrupted or inhibited, leading to a transformation in the wake structure. This transformation occurs at what is known as the ”critical aspect ratio,” a value that varies depending on flow conditions and the cylinder’s submergence. In the case of FWMCs, the critical aspect ratio is not consistently identified across studies, with values ranging from $h/D = 1$ to 7. This inconsistency is largely due to the submergence ratio (h/δ), which plays a pivotal role in influencing the flow around the cylinder but has not been thoroughly explored in the literature. For this study, where $h/D = 0.1 - 0.5$, it is assumed that the aspect ratio is below the critical value, leading to a flow regime characterized by more complex interactions and modified vortex shedding patterns, as illustrated in Figure (2.6).

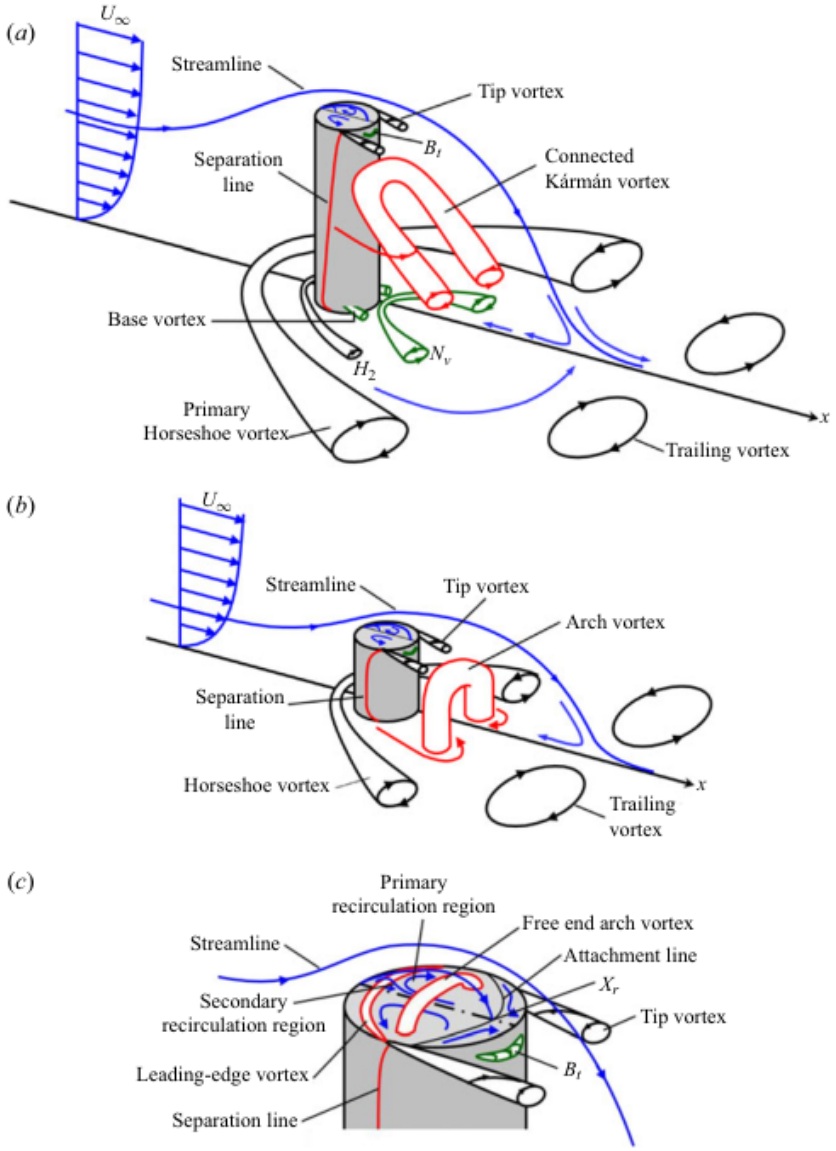

Figure 2.6: Diagram showing the time-averaged flow structure of a circular FWMC with (a) aspect ratio, h/d greater than the critical value and (b) h/d less than the critical value. (c) Illustration of prominent flow features at the free end of a circular FWMC. The labels are B_t – upper near-wake cross-stream vortex, N_v – near-wake base vortex, H_2 – secondary horseshoe vortex, and X_r – mean attachment length on the cylinder's top surface (Essel, Tachie, and Balachandar 2021).

Essel, Tachie, and Balachandar (2021) conducted experiments at a constant subcritical Reynolds number of $Re_D = 5540$ and a relative BL thickness of $\delta/d = 8.7$. The cylinder's height was varied to achieve five different aspect ratios: $h/d = 0.7,\ 1.8,\ 3.5,\ 5.3$ and 7.0 and corresponding submergence ratios that ranged from $\delta/h = 1.2-12.4$. Essel, Tachie, and Balachandar (2021) stated that this is the first extensive study to investigate the impacts of a submergence ratio of $\delta/h > 1$ on the wake flow around cylinders with a diverse set of aspect ratios, using time-resolved PIV measurements. Their findings revealed complex vortex dynamics, particularly in the spanwise plane, where quasi-symmetric vortex shedding near the free end of the cylinder and antisymmetric vortex shedding, accompanied by the flapping of the separated shear layers in the lower section of the cylinder, were observed.

These observations provide valuable insights into the flow behavior in the spanwise plane, which is crucial for understanding the formation and stability of the air layer downstream of the obstacle. The quasi-symmetric and antisymmetric vortex patterns identified by Essel, Tachie, and Balachandar (2021) suggest that similar instabilities could influence the distribution and behavior of the air layer in experiments focusing on gas injection drag reduction. Understanding these vortex dynamics is essential

for predicting how the coherent structures within the TBL, such as low-speed streaks, might interact with the air layer, thereby affecting its stability and effectiveness in reducing drag. This connection highlights the significance of investigating these flow structures in the context of air lubrication drag reduction strategies.

2.4. Gas injection drag reduction

The term gas injection drag reduction encompasses a range of techniques that involve injecting gas, such as air or other gases, into the BL of a fluid flow to reduce drag. Bubble drag reduction (BDR), transitional layer drag reduction (TLDR), and air layer drag reduction (ALDR) are specific methods within this broader category and are depicted in Figure (2.7). The primary goal of gas injection drag reduction is to alter the dynamics of the BL, thereby reducing friction and minimizing drag force on an object moving through the fluid, such as water or air. This technique is particularly significant in applications where minimizing drag is critical, as it can lead to energy savings, increased efficiency, and improved performance. According to Kim and Moin (2010), Bubble drag reduction could result in power savings of 2-5% on a net percentage basis, whereas air layer drag reduction could yield savings of 8-14% (Kim and Steen 2023).

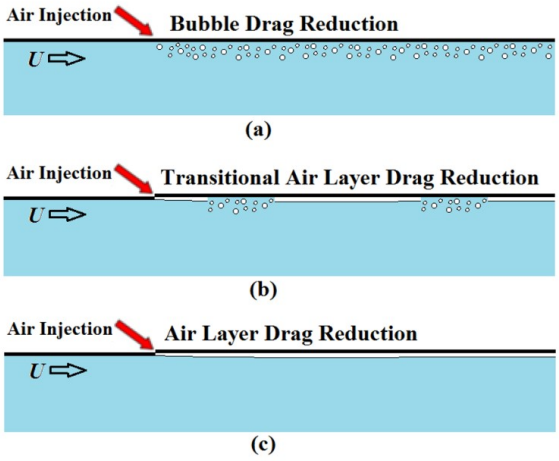

Figure 2.7: Possible gas injection drag reduction phases. a) Bubble drag reduction. b) Transitional layer drag reduction. c) Air layer drag reduction (Mäkiharju, Perlin, and Ceccio 2012).

2.4.1. Bubble Drag Reduction

Bubble Drag Reduction (BDR) involves the injection of gas bubbles into the TBL to reduce skin friction drag. Unlike Transitional Layer Drag Reduction (TLDR) and Air Layer Drag Reduction (ALDR), BDR relies on the dispersed phase of gas bubbles within the liquid flow, which interact with the TBL to alter its structure and dynamics. The effectiveness of BDR is significantly influenced by the size of the bubbles relative to the turbulent structures within the TBL.

The mechanism of drag reduction in BDR primarily involves the modification of the near-wall turbulent structures. Smaller bubbles, especially those smaller than 10 wall units (where wall units are defined as $l^* = \frac{\nu}{u_\tau}$), tend to reside within the low-speed streaks of the near-wall region. These microbubbles can dampen the intensity of turbulence by altering the local viscosity and density, leading to a reduction in the momentum transfer towards the wall. This contrasts with TLDR, where a transitional air layer begins to form, leading to changes in the BLs characteristics.

In the case of mesoscopic bubbles, which are comparable in size to the coherent structures in the TBL, the interaction is more dynamic. These bubbles can deform and oscillate due to the surrounding turbulent flow, absorbing kinetic energy from the turbulence and releasing it with a time delay. This energy exchange process reduces the intensity of turbulence, thereby lowering drag. This mechanism differs from ALDR, where the goal is to create a continuous gas layer that physically separates the liquid flow from the solid surface, nearly eliminating the interaction with the TBL and achieving higher

drag reduction efficiency.

Larger bubbles in BDR, which exceed the scale of the turbulent structures but remain smaller than the BL thickness, introduce high slip velocities between the gas and liquid phases. This slip reduces drag by decreasing the shear stresses within the TBL. However, the efficacy of BDR is often limited to a certain downstream length, as the bubbles tend to migrate away from the wall due to the shear forces, reducing their effectiveness over time. In contrast, ALDR, once established, provides a more stable and long-lasting drag reduction effect by maintaining a continuous air layer.

The comparison between BDR, TLDR, and ALDR highlights the unique role of bubble size and distribution in determining the effectiveness of drag reduction. While TLDR represents a transitional phase where bubbles begin to coalesce and form a partial air layer, ALDR achieves a fully developed air layer that decouples the liquid flow from the surface. BDR leverages the interaction between dispersed gas bubbles and the turbulent structures within the BL, providing a complementary approach to the other drag reduction techniques.

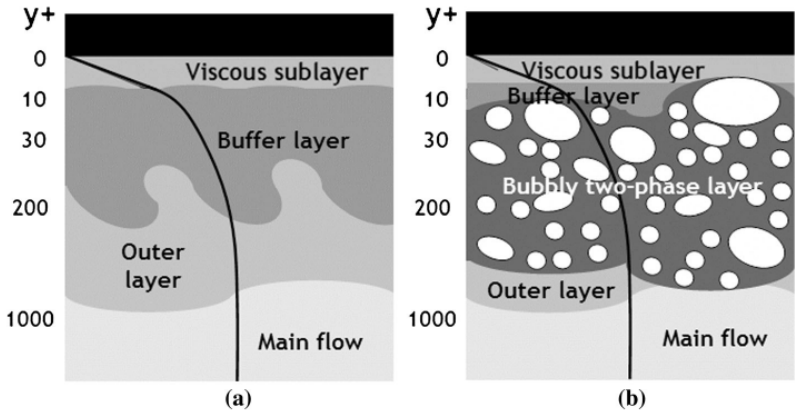

Figure 2.8: a) View of the TBL decomposition. b) Depiction of bubbles creating a two-phase flow and altering the TBL (Murai 2014).

BDR was first examined and studied in the mid 20th century. McCormick and Battacharyya (1973), were successful in using electrolysis to create hydrogen bubbles on the hull of a fully submerged body to demonstrate the drag-reducing properties of BDR. To gain a better understanding of BDR, multiple experiments in water tunnels and channels were done in the '80s and '90s (Madavan, Deutsch, and Merkle 1984, 1985) and (Merkle and Deutsch 1990, 1992). Because BDR showed promise, researchers tried to find the reason for the decrease in skin friction. Legner (1984) said that an increase in local effective viscosity due to shear thickening reduces wall shear stress, while Marie (1987) assumed a local reduction in density was responsible for a lower Reynolds shear stress. These early theories about drag reduction through microbubbles were challenged and refined by subsequent experimental and numerical studies, which leveraged advanced measurement techniques such as particle image velocimetry (PIV), laser Doppler velocimetry (LDV), and direct numerical simulations (DNS). For instance, numerical simulations conducted by Xu, Maxey, and Karniadakis (2002) demonstrated that small, spherical bubbles could sustain drag reduction by reducing the turbulent momentum transfer. The simulations revealed that the presence of microbubbles in the flow leads to a local positive divergence of fluid velocity, creating a velocity component normal to the wall. This effect displaces the quasi-streamwise vortical structures away from the wall, thereby increasing the spanwise gaps between low-speed streaks and reducing their coherence. As a result, the skin friction is reduced significantly. Ferrante and Elghobashi (2004) further supported these findings, showing that microbubbles can reduce the production of turbulence kinetic energy by shifting the location of peak Reynolds stress production away from the wall, where the transverse gradient of the mean streamwise velocity is smaller. These mechanisms collectively explain the sustained drag reduction observed in microbubble-laden TBLs, moving beyond the early theories that lacked such detailed understanding.

Murai (2014) conducted an extensive review on Bubble Drag Reduction (BDR), synthesizing research

from multiple studies to optimize drag reduction through the use of bubbles. As shown in Figure (2.9), he classified the data from previous campaigns into four groups based on bubble size: the microbubble regime, mesoscopic bubble regime, large bubble regime, and the rheological effect regime. This thesis will focus on the first three regimes, excluding the rheological effect regime.

In the microbubble regime, where bubbles are smaller than the coherent structures in the TBL, further distinction can be made between bubbles smaller than 10 wall units and those larger than 10 wall units, with wall units defined as $l^* = \frac{\nu}{u_\tau}$. According to Murai (2014), bubbles smaller than $10l^*$ primarily alter the internal fluid properties of the flow, while larger bubbles have a direct impact on the coherent structures within the BL, modifying them and thereby influencing drag reduction.

To better understand the interaction between microbubbles and the TBL, it is helpful to examine the impact of turbulence modulation by spherical particles, which serves as an analog for bubble behavior. Zhao, Andersson, and Gillissen (2010) and Zhao, Andersson, and Marchioli (2012) explored this phenomenon and found that smaller particles, much like microbubbles, tend to remain within low-speed streaks, which are key coherent structures contributing to skin friction drag. By altering the dynamics of these low-speed streaks, microbubbles can effectively modify the coherent structures in the flow, leading to a reduction in drag. This connection underscores the importance of further investigating how particles and bubbles influence these critical structures within the TBL.

Building on this understanding, Boris Jacob et al. (2010) conducted experiments to elucidate the mechanisms behind drag reduction by microbubbles in a TBL (TBL). Using Particle Image Velocimetry (PIV) to measure velocity in the wall-normal plane (x-y) beneath a flat plate, they investigated the impact of microbubbles with a small bulk concentration. Their findings indicated a decrease in momentum flux within the inner region of the TBL, suggesting that the presence of microbubbles might diminish the coherence of near-wall structures.

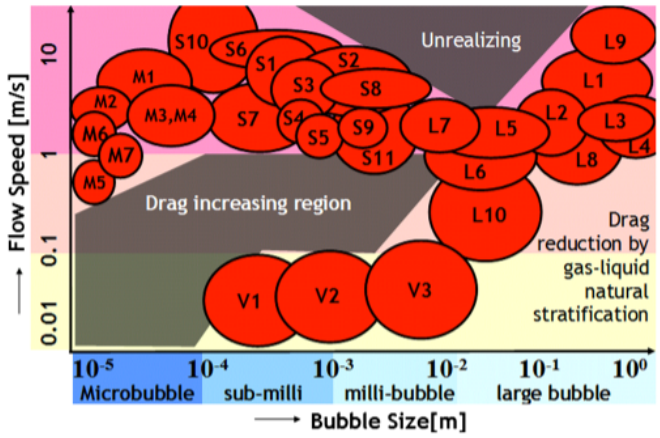

Figure 2.9: Results of published papers on a two-parameter domain on the experimental success of drag reduction (Murai 2014).

Mesoscopic bubbles, which are bubbles of the same length scale as the coherent structure in the flow, is the bubble size that appears most during experiments and appears most commonly in bubbly flow in nature. Kitagawa, Hishida, and Kodama (2005) made bubbles of $500\mu m$ in a flow of $5\frac{m}{s}$. This is the largest bubble that can exist when not going above the critical Weber number. The Weber number, $We = \frac{U}{\sqrt{\sigma/\rho L}}$, where U is the velocity, σ is the surface tension, ρ is the mass density, and L the characteristic length. If a bubble has a Weber number that is larger than the critical Weber number, it becomes unstable and can burst into smaller bubbles. Drag reduction by using mesoscopic bubbles can be contributed due to the deformability of the bubble (Serizawa and Kataoka 1990). In their research, they found that the deformability of the bubble was an absorber of kinetic energy which was then released with a time delay. Due to this time delay, the local acceleration of the turbulence was lessened, which in turn reduced the drag. This was also confirmed by (Lu, Fernandez, and Tryggvason 2005), also stating that non-deforming bubbles increase the drag.

In the large bubble regime, the bubbles are larger than the coherent structures, but still smaller than the BL thickness. In this regime, the high slip velocities between the gas phase and the liquid reduce the drag. This high slip velocity is obtained by seven force components; drag, lift, buoyancy, pressure gradient, inertia, and history forces (Murai 2014). Guin et al. (1996) implied that the spatially developing bubbly flow in the TBL characterized the drag reduction. Murai, Fujii, et al. (2006) and Murai, Oishi, et al. (2006) also saw that their bubbles oscillated in the wall-normal direction and attributed a decrease in local turbulent shear stress to this phenomenon.

A study done by Elbing et al. (2008) showed that most of the drag reduction achieved by BDR was limited to a couple of meters downstream of the injection, which was also found by Sanders et al. (2006). The latter stated that this could be due to bubble migration, which occurs when the near-wall shear causes the bubbles to move away from the surface of the plate. The majority of BDR experiments conducted so far have been at low Reynolds numbers and small scales; the appropriate scaling laws also remain uncertain. Numerous studies, such as the one by Elbing et al. (2008), have revealed that ALDR is more efficient in reducing drag. As a result, current drag reduction techniques tend to gravitate towards ALDR.

2.4.2. Air layer drag reduction

ALDR is similar to BDR, but when a critical volumetric flux of air is achieved, the bubbles coalesce, and a continuous air layer is formed between a solid surface and the liquid flow. Sanders et al. (2006) found that at optimal conditions, a nearly continuous gas film had a near-100% skin-friction drag reduction. In Figure (2.10), it can be seen that once the ALDR was achieved, the drag reduction is also near-100%. According to Elbing et al. (2008), the critical volumetric flux, q_{crit}, required to achieve air layer drag reduction was approximately proportional to the square of the free-stream speed or linearly proportional to the nominal air-layer thickness, $t_a = \frac{Q_A}{BU_\infty}$. Here U_∞ is the free-stream velocity, Q_A is the airflow rate, B is the injector span, and t_a is the air layer thickness.

However, this proportionality was not observed in the study by Nikolaidou et al. (2024), which highlights the influence of different flow characteristics, such as freestream velocity and TBL development length, on the formation of the air layer. The author's findings suggest that while increasing the freestream velocity extended the air layer length, the maximum thickness remained relatively unchanged. Conversely, a longer TBL development length resulted in a shorter air layer length, likely due to the decrease in local mean velocity as the TBL grew. This discrepancy underscores the need for further investigation into how TBL conditions influence the stability and effectiveness of ALDR, particularly in the context of varying upstream flow conditions.

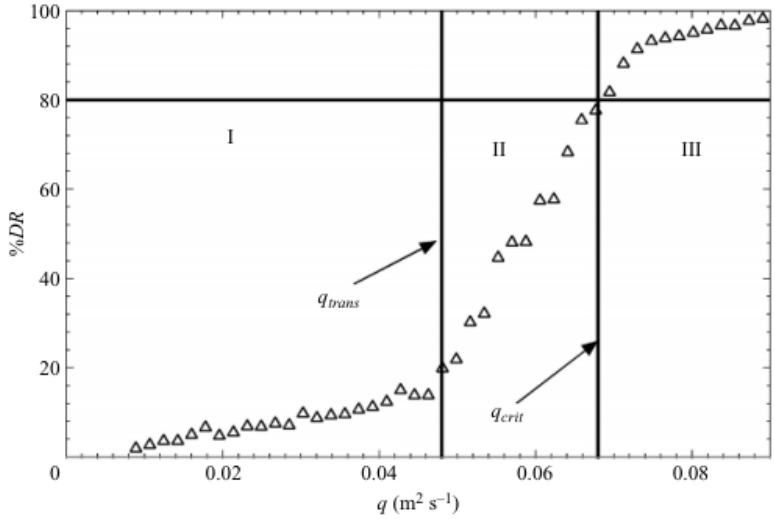

Figure 2.10: Three regimes of gas injection drag reduction: I, BDR regime; II, a transitional regime; and III, an ALDR regime with a near-100% drag reduction (Elbing et al. 2008).

Zverkhovskyi (2014) performed a study on the hydrodynamic properties of air cavities and their potential for ship drag reduction. In this study, a cavitator was used to gain a more stable air layer at the cost of disturbing the incoming flow (Figure (2.11)). The amount of drag reduction achieved was dependent on the cavity length and thickness. The author showed that these parameters were influenced by initial flow conditions, but he also noted that the gravity wave was the dominant factor in defining the cavity length. This finding suggests that the maximum cavity length is constrained by the gravity wavelength, with the cavity tending to break up when wave amplitudes at the free surface closely match the cavity's thickness. Although the author observed changes in the BL due to the air cavity, leading to variations in frictional drag, a comprehensive understanding of their dependence on various parameters still requires further investigation.

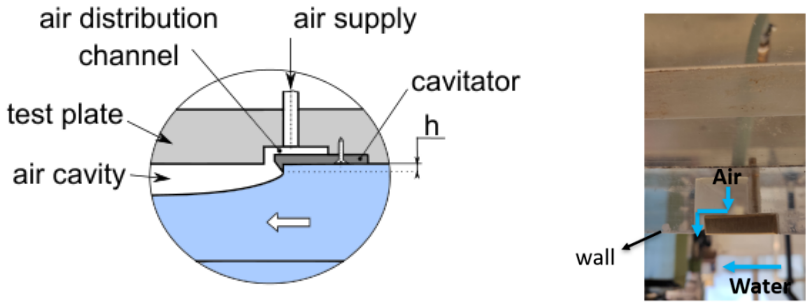

Figure 2.11: Schematic of Zverkhovskyi (2014) (left) and Anand (2021) (right) injector

Further investigations into the influence of an air cavity on a TBL were conducted by Anand (2021). His study focused on identifying the shape of the air cavity and examining the development of the TBL in its vicinity. A slot-type injector was used to inject air under the plate (Figure (2.11)), minimizing disturbances to the incoming flow and maintaining a canonical BL as much as possible. The author found similarities between the flow geometry of a TBL below an air cavity and flow over a solid bump, providing insights into the potential impact of such cavities on the BL.

Nikolaidou et al. (2024) expanded on these findings by studying the effect of different flow characteristics on the air layer, specifically by varying the streamwise development length and freestream velocity. Using a setup similar to Anand (2021), Nikolaidou investigated the changes in air layer thickness and length under different TBL conditions. Her results, shown in Figure (2.12), indicated that the maximum air layer thickness remained consistent across different velocities, while the air layer length varied with the streamwise development length. These findings underscore the importance of considering the incoming TBL characteristics in optimizing air layer formation and stability. Given that we know the incoming flow conditions have a significant impact on the air layer, it becomes equally important to understand the effects of obstacles on these conditions. This is particularly relevant for the current research's focus on the effect of upstream obstacles on air lubrication regimes, as these obstacles can potentially alter the incoming flow and, consequently, the air layer's characteristics.

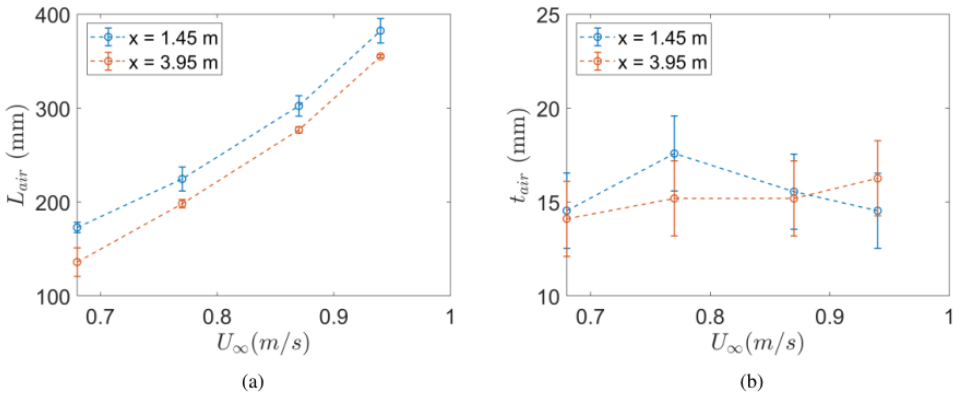

Figure 2.12: (a) Air cavity length and (b) maximum air layer thickness at different streamwise velocities and streamwise development lengths (Nikolaidou et al. 2024).

Nikolaidou et al. (2024) expanded on the findings of Anand (2021) by studying the effect of different flow characteristics on the air layer, specifically by varying the streamwise development length and freestream velocity. Anand utilized a setup similar to that originally developed by Nikolaidou. In her study, Nikolaidou investigated the changes in air layer thickness and length under different TBL conditions. Her results, shown in Figure (2.12), indicated that the maximum air layer thickness remained consistent across different velocities, while the air layer length varied with the streamwise development length. This highlights the critical influence of incoming TBL characteristics on air layer formation and stability. Given the significant role that incoming flow conditions play in determining air layer behavior, it is equally important to understand how obstacles upstream might affect these conditions. Addressing this research gap is the primary focus of the current study, which seeks to explore the interaction between upstream obstacles and the air layer, potentially altering the incoming flow and the resulting air layer characteristics.

2.5. Research Questions

The maritime industry continuously seeks innovative methods to reduce fuel consumption, with drag reduction being a primary focus. Gas injection has emerged as a promising technique, forming a lubricating air layer along the hull of marine vessels to minimize frictional resistance. However, achieving the most effective configuration requires a deeper understanding of the interaction between the gas layer and possible obstacles that may hinder its effectiveness. This research aims to address this need by exploring the effect of an upstream finite wall-mounted cylinder (FWMC) on the behavior of the air layer formed through gas injection.

Previous studies have primarily focused on confirming the drag-reducing effects of gas injection and identifying optimal setups. While Murai (2014) compiled valuable research data on Bubble Drag Reduction (BDR), the literature on Air Layer Drag Reduction (ALDR) by researchers such as Sanders et al. (2006), Elbing et al. (2008), and Elbing et al. (2013) has largely concentrated on verifying the phenomenon itself. Anand (2021) and Nikolaidou et al. (2024) explored the impact of gas injection on the TBL, focusing specifically on the x-y plane.

Direct Numerical Simulations (DNS) conducted by Xu, Maxey, and Karniadakis (2002), Ferrante and Elghobashi (2004), and Pang, Wei, and Yu (2013) have provided insights into bubble injection in a TBL. However, DNS's limitations at high Reynolds numbers and the need for well-defined boundary conditions make experimental measurements more preferable for practical applications. Given the potential application of gas injection in high Reynolds number scenarios, this research emphasizes experimental investigation.

Building on insights from Boris Jacob et al. (2010) and Murai (2014), who highlighted the interaction between microbubbles and coherent structures leading to drag reduction, previous studies raised questions about their influence on near-wall turbulence. However, this study does not focus on drag re-

duction or the interaction between microbubbles and coherent structures. Instead, it concentrates on the behavior of air layers in the presence of upstream obstacles, particularly within the streamwise-spanwise plane (x-z), an area where significant research gaps remain.

A significant research gap exists in understanding the impact of upstream obstacles on the air layer within the streamwise-spanwise plane (x-z). While the x-y plane has been studied, less is known about the effects in the x-z plane, particularly how obstacles placed upstream affect the formation and stability of the air layer. The presence of an obstacle can introduce complex flow dynamics and interactions that are not well-documented. This thesis seeks to fill this void by offering valuable insights into the interaction between the air layer, the TBL, and upstream obstacles. Additionally, no prior research has investigated the effect of an upstream finite wall-mounted cylinder on the behavior of the air layer, making this study novel and essential.

The main research question guiding this thesis is:

"How does the placement and the dimensions of an upstream finite wall-mounted cylinder affect the formation and characteristics of different gas phases (bubbly, transitional, air layer) in a turbulent boundary layer?"

The subquestions are:

1. "How do the height and distance of upstream circular cylindrical obstacles from the injector influence the formation and behavior of the bubbly regime, particularly in terms of bubble morphology and velocity distributions in a turbulent boundary layer?"
2. "How do the height and distance of upstream circular cylindrical obstacles from the injector affect the transitional regime, specifically in relation to the stability and structure of the air layer in a turbulent boundary layer?"
3. "How do the height and distance of upstream circular cylindrical obstacles from the injector impact the air layer regime, particularly with regard to its length and the formation of breakups near the injector in a turbulent boundary layer?"

This research will focus on imaging the bubbles and studying the effect of upstream obstacles on these air layers. Experiments will be conducted at different object heights and distances from the air injector, as well as at varying free-stream velocities. By analyzing the streamwise-spanwise plane (x-z), this study aims to provide a comprehensive understanding of the dynamic interactions between the air layer and the turbulent BL.

Addressing this research gap is crucial for advancing the field of drag reduction, optimizing configurations, and gaining valuable insights into the complex dynamics of gas layer and TBL interactions. By understanding the interaction between FWMCs and the behavior of the air layer, this research will contribute both to theoretical understanding and practical applications in high Reynolds number situations, ultimately aiding in the development of more efficient drag reduction techniques for marine vessels and other engineering applications.

3

Experimental setup and data acquisition

In this chapter, the experimental setup, selected flow cases, and data acquisition methodologies used in this study are presented. The primary objective of this setup is to investigate the effects of upstream obstacles on air layer formation and stability within a TBL. The experimental setup is designed to systematically study these effects under varying flow conditions and obstacle configurations.

3.1. Experimental setup

The experimental setup was installed in the water tunnel at the Process and Energy facilities at TU Delft. The test section of the water tunnel features a 0.6×0.6 m^2 cross-sectional area and extends over a length of 5 m. To allow for optical access, the walls of the test section are made from Plexiglas. Upstream, a contraction accelerates the flow, preceded by a honeycomb structure and multiple screens to ensure isotropy and minimize the intensity of turbulence, which is less than 1% (tudelft.nl 2004). The closed-loop water tunnel system operates with a pump to drive the flow, recirculating it through a tube that runs underneath the tunnel. The pump frequency can be adjusted to control the flow velocity, which can reach a maximum of 1 m/s.

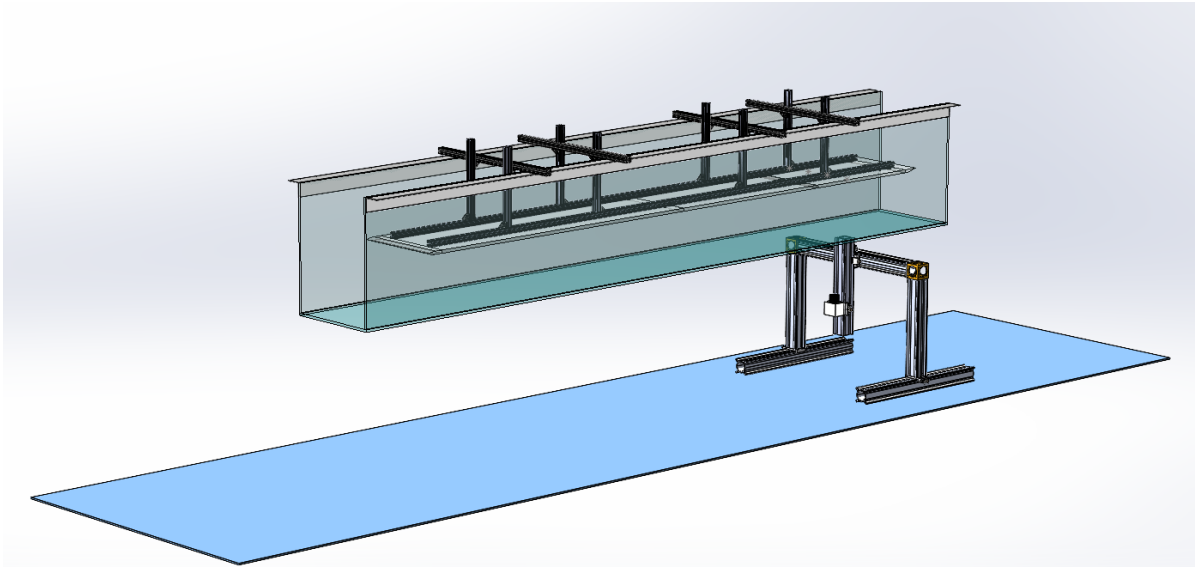

Figure 3.1: SolidWorks model of the experimental setup. The flow direction is from left to right.

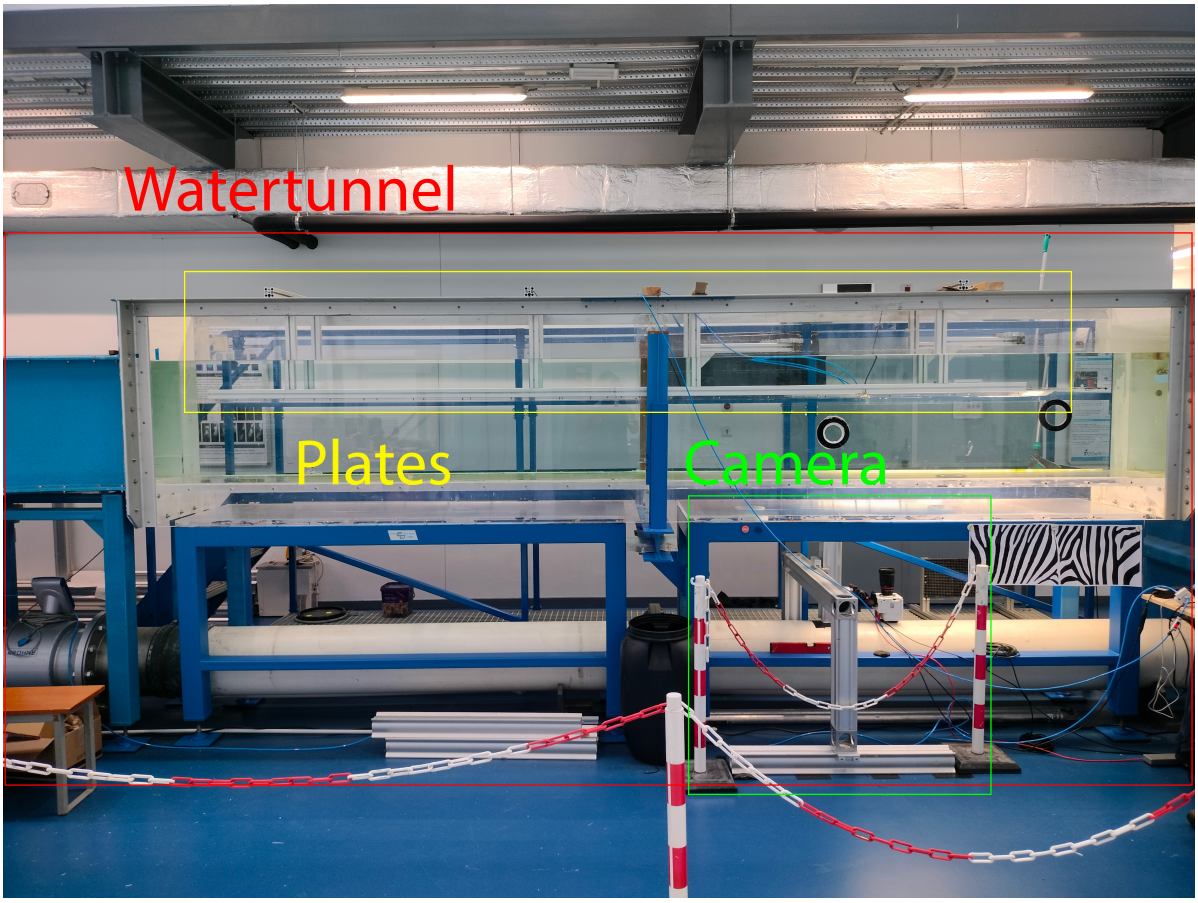

Figure 3.2: Photograph of the experimental setup at TU Delft, showing the placement of the flat plates and camera mount within the water tunnel.

As shown in Figure (3.1), the experimental setup consists of three main components: the water tunnel, two flat plates, and a support structure for the camera mount. The camera mount is designed for controlled horizontal and vertical adjustments, allowing precise positioning for image capture. The two flat plates rest on support brackets within the water tunnel, submerged 30 cm above the tunnel's bottom. This positioning is critical as it allows a fresh BL to develop at the leading edge of the upstream plate, ensuring that the BL is fully developed by the time it reaches the area of interest (Nikolaidou et al. 2024; Harleman et al. 2011).

Each plate measures 2 m (length) × 0.58 m (width) with a thickness of 2 cm, providing a total length of 4 m. To ensure the formation of a fully developed TBL, the flow was tripped at a specific location. Tripping is essential for transitioning the BL from laminar to turbulent, which is necessary for studying the effects of obstacles on air layer formation. The optimal trip for the free-stream velocities used in the experiments was determined to be 0.4 mm at a distance of 10 cm from the leading edge. The calculations supporting this choice are presented in Table 3.1.

Tripping the BL was achieved using a triangular shaped strip. The effectiveness of BL tripping depends on factors like the size, shape, and placement of the tripping devices, as well as flow conditions such as free-stream velocity and fluid viscosity. Preston (1957) determined that the BL transition occurs at $Re_\theta \approx 100$. The value of Re_θ can be determined using the following equations:

$$\theta = 0.664\sqrt{\frac{\nu x}{U_\infty}} \tag{3.1}$$

$$Re_\theta = \frac{U_\infty \theta}{\nu} \tag{3.2}$$

Braslow and Knox (1957) provided an empirical relationship that links the flow conditions within an undisturbed laminar boundary to the critical roughness height, k_{cr}, required to trigger transition. This relationship is represented by the Reynolds number, Re_k, which is based on the trip roughness height and the flow velocity at the trip height:

$$Re_k = \frac{U_k k}{\nu_k} \tag{3.3}$$

The velocity at the tripping roughness height, U_k, can be determined using the Blasius solution:

$$U_k = y\frac{u}{\kappa}f'(\eta) \quad \text{where:} \quad f'(\eta) = \kappa \cdot \eta^{-0.5} \quad \text{and,} \quad \eta = \frac{k}{\delta} \tag{3.4}$$

U_∞ (m/s)	k (mm)	Re_k	Re_θ
0.94	0.4	759	204
	0.5	848	
	0.8	1073	
0.68	0.4	595	173
	0.5	665	
	0.8	842	
0.49	0.4	465	147
	0.5	520	
	0.8	658	

Table 3.1: Tripping properties for different velocities and roughness heights.

The tripping distance was determined using Equation (3.2), where Re_θ was found to be between 147 and 204. The tripping heights and their corresponding Re_k values are listed in Table 3.1. By carefully managing the tripping process, a fully developed TBL was established, which is crucial for studying the impact of obstacles on the formation of air layer regimes. This process is foundational to the experiments conducted in this thesis, ensuring that the BL conditions are appropriate for investigating gas injection drag reduction techniques.

The slot-type air injector used in this study was modeled after designs utilized by Nikolaidou et al. (2024) and Anand (2021) due to its minimal intrusiveness on the flow conditions. This injector spans the entire width of the downstream plate, with a slot measuring 4 mm in width and positioned 3.2 meters from the plate's leading edge. To ensure uniform air distribution across the span, the injector was equipped with three air intake points. Compressed air was pumped into these intakes, increasing the pressure within a chamber before being delivered perpendicular to the flow. By modifying the free-stream velocity, U_∞, and the airflow rate, Q_{air}, three distinct air regimes could be achieved: bubbly, transitional, and air layer regimes. Q_{air} was manually controlled with a pressure regulator, and flow was measured digitally with a flow rate meter, as shown in Figure (3.3).

(a) (b) (c)

Figure 3.3: **(a)** Pressure regulator, **(b)** flow meter and **(c)** injector (dimensions in mm, flow goes from right to left) (Nikolaidou et al. 2024) used in the experiments (rs-online 2024; Corporation, n.d.).

The gas regimes under the flat plate were imaged in the streamwise-spanwise (x-z) plane using a LaVision Phantom VEO 640L camera. This camera was placed in a down-up configuration and fitted with a 35 mm lens. The camera has a 2560x1600 pix^2 sensor and supports a frame rate of up to 1.4 kHz. Two different fields of view (FOV) were used depending on the flow velocities to capture different aspects of the air layer formation. The specific details of the FOVs used in the experiments are summarized in Table 3.2 and can be seen in Figure (3.4).

U_∞ (m/s)	Field of View	Extents (mm^2)	Extents (δ)	Magnification (px/mm)
0.94	FOV1	365 x 230	6 x 3.8	7
0.68	FOV1	365 x 230	5.8 x 3.65	7
0.49	FOV2	545 x 340	8 x 5.7	5

Table 3.2: Details of the fields of view (FOV) used in the experiments.

The experimental campaign was designed to systematically investigate the effects of upstream obstacles on the formation of air layer regimes in a TBL. The primary goal of these experiments was to explore how variations in freestream velocity, obstacle height, and obstacle distance from the air injector influence the behavior of the gas phases.

3.2. Obstacle variation

The main focus of this experimental study was to examine the effects of upstream obstacles on the air layer created by gas injection. Cylindrical barriers with a diameter of 1 cm and heights of 1 mm, 3 mm, and 5 mm, referred to as h_1, h_2, and h_3 respectively, were utilized. These heights were chosen so that the obstacle does not traverse the estimated log layer. These obstacles were positioned at various upstream distances from the air injector, specifically -1.5 cm, -3.5 cm, and -5.5 cm, denoted as L_1, L_2, and L_3. For comparison, a control scenario without any obstacle was also included in the study. Illustrations of the obstacle positions are available in Figure (3.4). The three heights were tested at the three different locations, resulting in a total of ten distinct cases. The Reynolds number based on obstacle diameter (Re_D) was calculated for each configuration to characterize the flow regimes around the cylinders and can be found in Table 3.3. An illustration of the experimental setup, including the two fields of view (FOVs) used for imaging, is presented in Figure (3.4), showing both the side (a) and top (b) views, with the FOVs clearly marked for clarity, detailed information can be found in Table 3.3.

U_∞ (m/s)	Re_D	L (cm)	h (mm)	h/δ	h^+	TBL region
0.94, 0.68, 0.49	9400	-1.5	1	0.017	35	Buffer / Log Layer
			3	0.050	110	Log Layer
			5	0.084	180	Log Layer
0.94, 0.68, 0.49	6800	-3.5	1	0.016	27	Buffer Layer
			3	0.048	80	Log Layer
			5	0.079	135	Log Layer
0.94, 0.68, 0.49	4900	-5.5	1	0.015	20	Buffer Layer
			3	0.044	60	Log Layer
			5	0.073	100	Log Layer

Table 3.3: Obstacle properties for different velocities and heights, including Reynolds numbers and their relation to TBL regions.

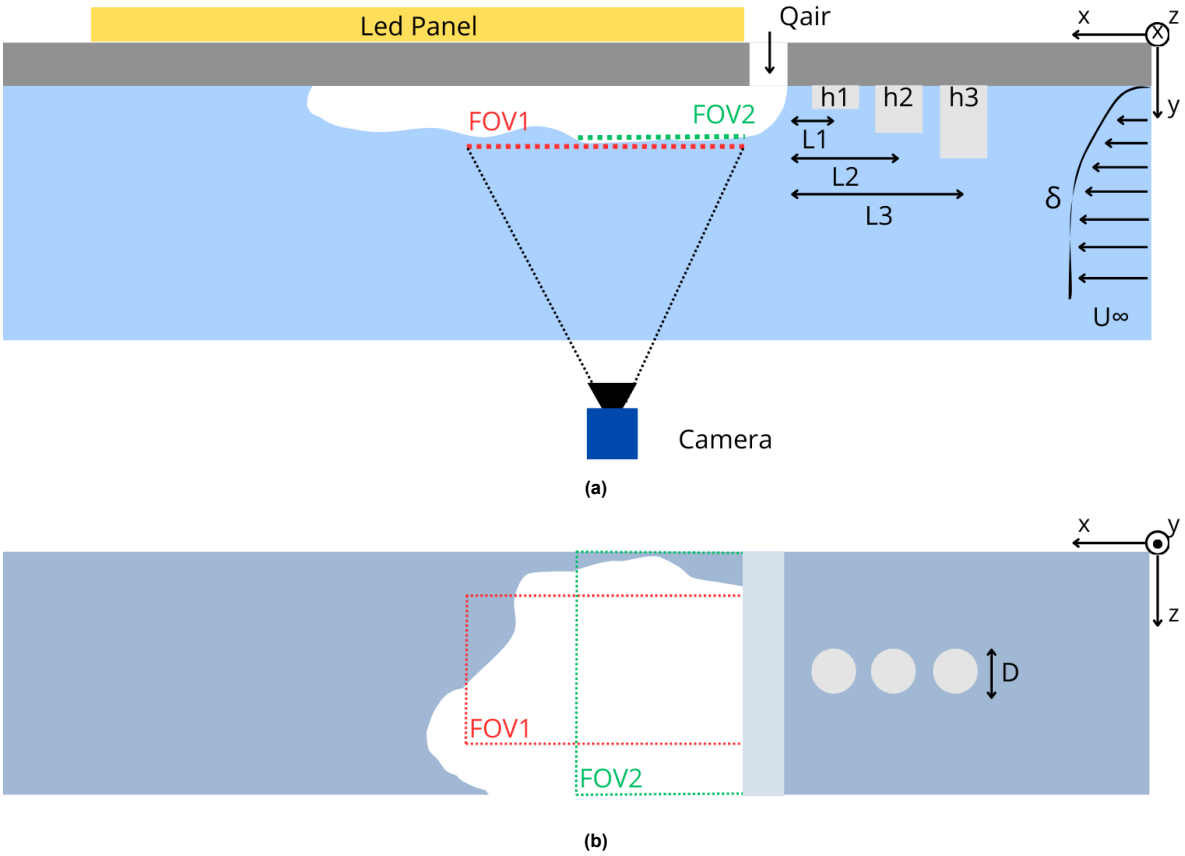

Figure 3.4: Schematic illustration of the experimental setup and the two different FOVs in the x-y plane **(a)** and x-z plane **(b)**.

3.3. Freestream velocity variation

With the obstacle configurations established, the experiments proceeded by varying the free-stream velocities to investigate the effect of the obstacles on the different regime formation. The selected velocities were 0.94 m/s, 0.68 m/s, and 0.49 m/s, covering a range of flow conditions relevant to the study. The properties of the TBL at each velocity were estimated using the Reynolds number (Re_x) and boundary layer thickness (δ) based on Equation (2.2), as shown in Table 3.4. The wall-normal units, y^+, were calculated using Equation (2.5), where $u_\tau = \sqrt{\tau_w/\rho}$. The values in the table represent the physical length corresponding to 1 y^+ unit in meters. The Reynolds number based on the momentum

thickness ($Re\tau = \frac{u_\tau \delta}{\nu}$) was also calculated for comparison with other studies.

U_∞ (m/s)	Re_x	Re_τ	δ (m)	y^+ (m)
0.94	3 $\cdot 10^6$	2176	0.060	2.75 $\cdot 10^{-5}$
0.68	2.2 $\cdot 10^6$	1707	0.063	4.95 $\cdot 10^{-5}$
0.49	1.6 $\cdot 10^6$	1374	0.068	3.69 $\cdot 10^{-5}$

Table 3.4: Estimated BL properties for different free-stream velocities, including Reynolds numbers and BL thickness.

The BL characteristics were calculated utilizing conventional empirical equations and corroborated by existing studies. It should be highlighted that these values are approximate and may differ in actual experiments. The TBL development at each velocity was found to be consistent with previous experimental setups, validating the chosen velocities for further investigation (Nikolaidou et al. 2024).

3.4. Regime variation

By varying the free-stream velocity (U_∞) and adjusting the air flow rate (Q_{air}), different air layer regimes could be achieved.. Three distinct regimes were identified: bubbly flow, transitional flow, and air layer flow, as detailed in Table 3.5 and Figure (3.5).

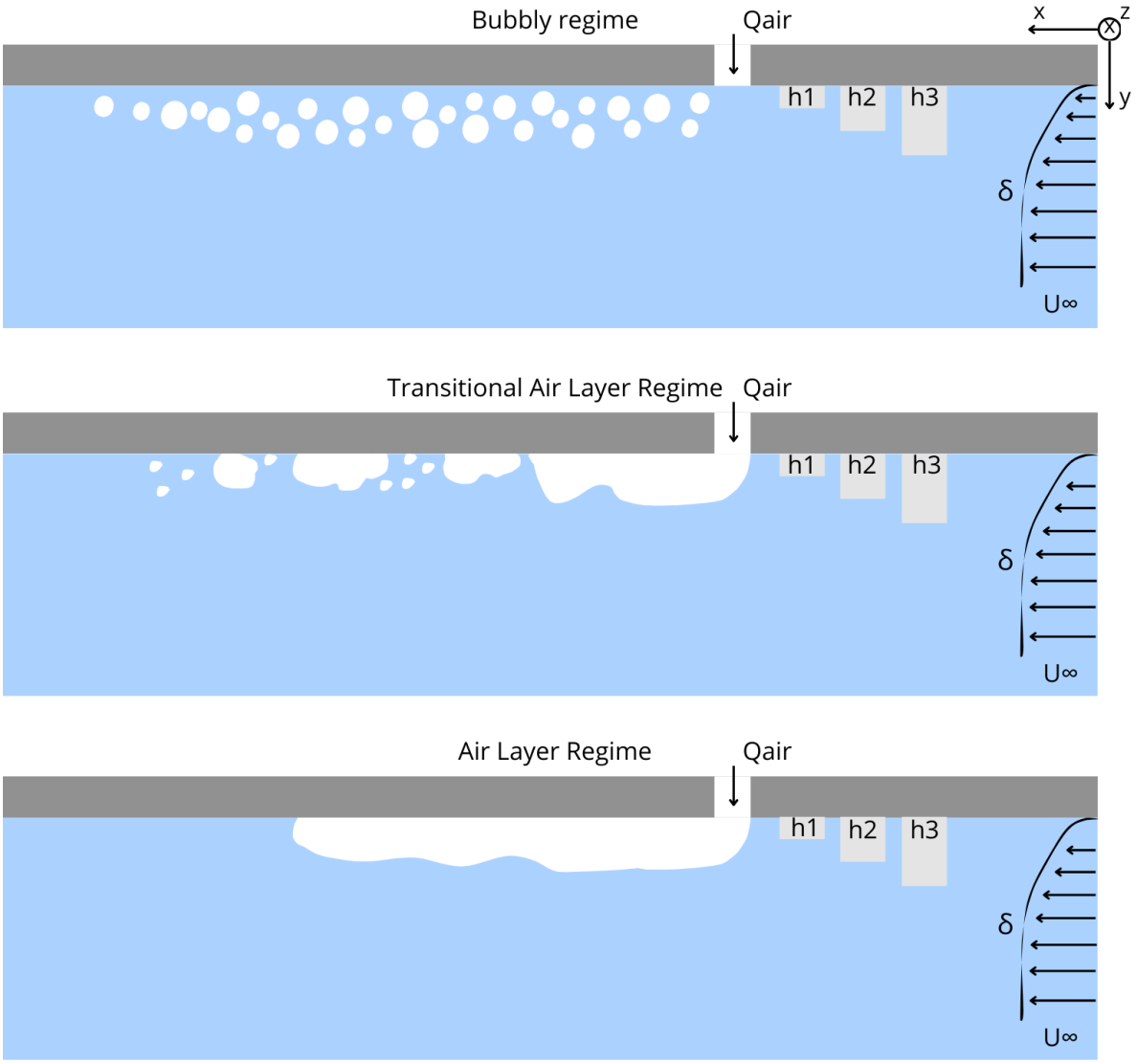

Figure 3.5: Schematic illustration of the experimental setup in the x-y plane, showing the different regimes and the obstacle positions and sizes.

U_∞ (m/s)	Q_{air} (l/min)	Air Regime	FOV	No Images	f (Hz)
0.94	1.5 l/min	Bubbly	FOV1	3029	500
0.68	6-96 l/min	Bubbly, Transitional, Air Layer	FOV1	1500	500
0.49	3-30 l/min	Air Layer	FOV2	3029	500

Table 3.5: Flow conditions and air regimes captured during the experiments.

By systematically varying the airflow rate and free-stream velocity, as shown in Table 3.5, the study aimed to document the transition between these regimes and assess the formation of the air layer under different conditions. The results from these experiments provided insights into the optimal conditions for achieving and maintaining an air layer in the presence of upstream obstacles.

3.4.1. Bubbly regime

For the bubbly regime, the behavior of air bubbles over a flat plate was investigated under the specific flow conditions listed in Table 3.5. The particular flow rate, Q_{air}, was chosen to create a very evenly

distributed pattern of air bubbles across the entire span of the flat plate.

The initial phase of the experiment involved taking measurements without any obstacles to establish a baseline for comparison. Following this, the cylindrical obstacles introduced in Section 3.2 were positioned at specific distances upstream of the air injector, as detailed in Table 3.3. These configurations were chosen to systematically investigate the impact of obstacle height and placement on bubble dynamics. It is important to note that FOV1 does not capture the entire span of the submerged plate, instead focusing on a specific region where bubble behavior is analyzed.

To capture the dynamics of the bubbles, a cyclic-based imaging approach was used. The images were taken at a frame rate of 500 Hz, with two images captured every one-second cycle, as illustrated in Figure (3.6). During the course of the experiment, 1514 independent image pairs were collected. By waiting one second between image pairs, it was ensured that all previously imaged bubbles within FOV1 were replaced by new bubbles, providing independent data for statistical convergence for each image pair. This methodology allows for a detailed examination of bubble properties and their interactions with obstacles, providing insights into the influence of different obstacle configurations on bubble distribution and dynamics.

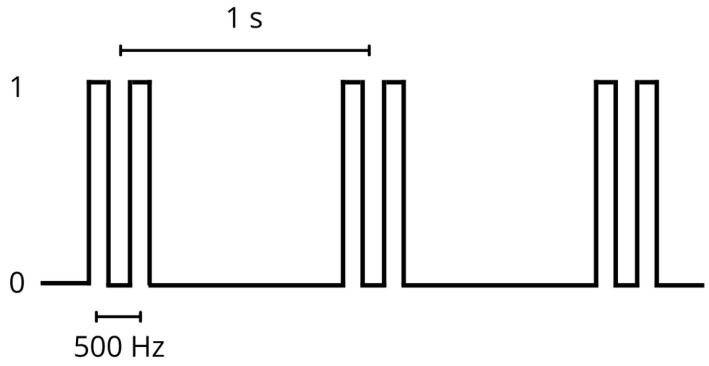

Figure 3.6: Illustration of the cyclic image approach used to capture independent data for statistical analysis.

3.4.2. Transitional regime

In the transitional regime, the same FOV1 was used, but the experimental approach involved systematically varying the air flow rate (Q_{air}) to capture the different gas phases. At a free-stream velocity of 0.68 m/s, as shown in Table 3.5, all three different gas phases (bubbly, transitional, and air layer) could be achieved by altering the air flow rate. The placement of obstacles remained identical to those used in the bubbly regime experiments. The air flow rate was varied in increments of 6.0 l/min to provide a detailed examination of the transitions between different gas phases and to study the effects of obstacles within these regimes.

This incremental variation in flow rate was chosen based on preliminary observations indicating that the first significant change in regime occurred at 18.0 l/min, which represents an increase of 12 l/min from the initial condition. The smaller increments allowed for a more detailed examination of the transitions between different gas phases.

To capture the time-dependent nature of the regimes, 1500 continuous images were taken at a frame rate of 500 Hz. This high-frequency imaging ensured that the dynamic behavior of the bubbles and their interactions with the obstacles were accurately recorded. However, because these images were taken at a continuous rate, the data set lacks statistical independence, which limits the robustness of the statistical analysis compared to the cyclic approach used in the bubbly regime.

3.4.3. Air layer regime

In the air layer regime, a free-stream velocity of 0.49 m/s was used to study the formation and behavior of a continuous air layer along the surface of a flat plate. For this regime, FOV2 was utilized, as detailed in Table 3.5, providing a broader spanwise view compared to FOV1. This broader view allowed for a

more detailed analysis of the air layer's behavior across the width of the plate. The LED panel was repositioned to ensure proper illumination of the entire span of FOV2.

As in the other regimes, the initial step was to establish a baseline by taking measurements without any obstacles to determine the conditions under which a stable air layer would form. It was determined that at an air flow rate of 3.0 l/min, a stable air layer developed along the surface, which served as the baseline for subsequent experiments involving obstacles.

In these experiments, the same cylindrical obstacles were used, and their impact on the air layer's stability and continuity was observed. The focus was on analyzing the air layer's length and morphology, as these are critical factors for drag reduction. The air flow rate was incrementally increased to assess whether the air layer properties observed in the baseline case could be maintained in the presence of obstacles.

As with the transitional regime, the lack of statistical independence in the continuous imaging approach is noted, which may affect the robustness of the statistical analysis. However, the systematic variation of air flow rate allowed for a thorough examination of the air layer's response to different flow conditions and obstacle configurations.

This chapter detailed the experimental setup and methodologies employed to study the effects of upstream obstacles on air layer formation and stability in a TBL. The experimental campaign was carefully designed to investigate how variations in freestream velocity, obstacle height, and obstacle distance from the air injector influence the behavior of different gas regimes. The next chapter will discuss the image processing techniques used to analyze the data collected during these experiments, ensuring accurate interpretation of the observed phenomena.

4

Image processing

In this section, the image processing techniques used to analyze the data collected during the experimental campaign are discussed. The images were captured using the Davis software, which facilitated background removal and image binarization at a specified bin level. After preprocessing with Davis, the images were converted from im7 format to a format readable by MATLAB. Subsequently, the main MATLAB code was executed to process the images and extract meaningful information.

The image processing was conducted in three distinct phases, each corresponding to a different gas phase regime: the bubbly regime, the transitional regime, and the air layer regime. Each regime required a tailored approach to ensure accurate analysis. An overview of the steps involved in the image processing pipeline is provided, along with an explanation of the MATLAB code used for each regime.

4.1. Overview of Image Processing Steps

The image processing workflow involved several key steps:

1. **Background removal and binarization**: Using the Davis software, the background of each image was removed, and the images were binarized at a specified bin level.
2. **File conversion**: The binarized images, initially saved as im7 files, were converted to a format readable by MATLAB.
3. **Image preprocessing**: MATLAB was used to preprocess the images, which included noise removal, closing operations, and filling holes.
4. **Data segmentation and analysis**: The processed images were segmented, and properties such as velocities, areas, and diameters were computed and analyzed.

4.2. Bubbly regime

The following steps outline the image processing procedure for the bubbly regime.

To start, each pair of images was preprocessed to eliminate noise and enhance details. The *preprocessImage* function handled noise reduction, morphological closing, and filling in holes. This preparation was crucial for accurate bubble tracking. Next, bubbles were identified and tracked across consecutive image pairs using the *connectBubbles* function. This function assigned labels to bubbles, computed their centroids, matched them between frames, and determined their velocities. Outliers were filtered out to ensure the validity of the velocity measurements. Following this, the *segmentImage* function segmented the images to calculate the areas and diameters of bubbles. This segmentation was done to assess the streamwise and spanwise variations, the images were divided into 25 evenly spaced segments along the z-axis, with each segment corresponding to 0.15δ. Additionally, the x-axis was divided into 3 evenly spaced segments, each corresponding to 2δ this is illustrated in Figure (4.2), details can be found in Table 4.1. This segmentation allowed for a detailed analysis of the variations in bubble

behavior across different regions of the flow field, as can be seen in Figure (4.2).A schematic of the image processing steps is presented in Figure (4.1).

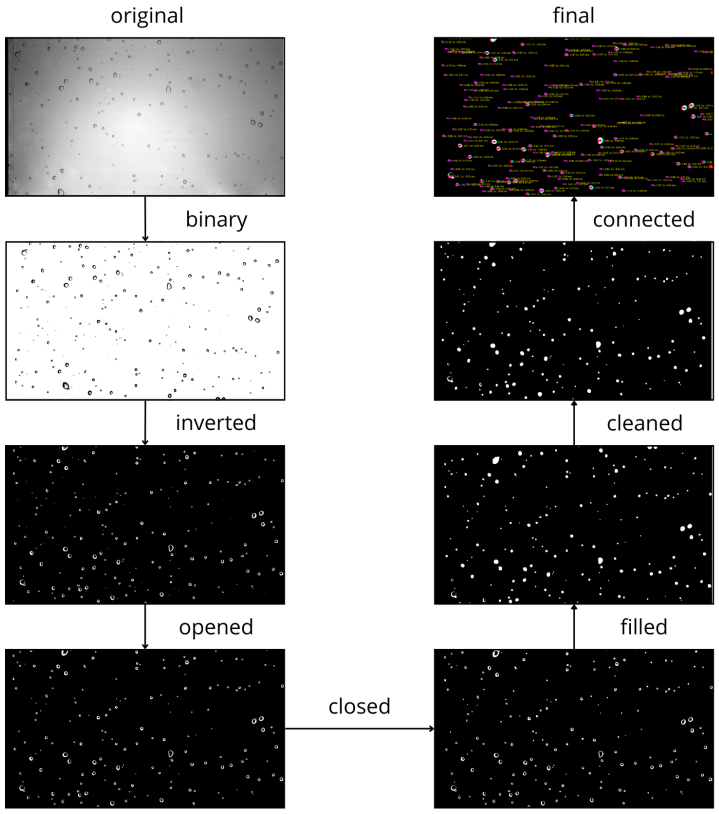

Figure 4.1: Image processing steps for the bubbly regime.

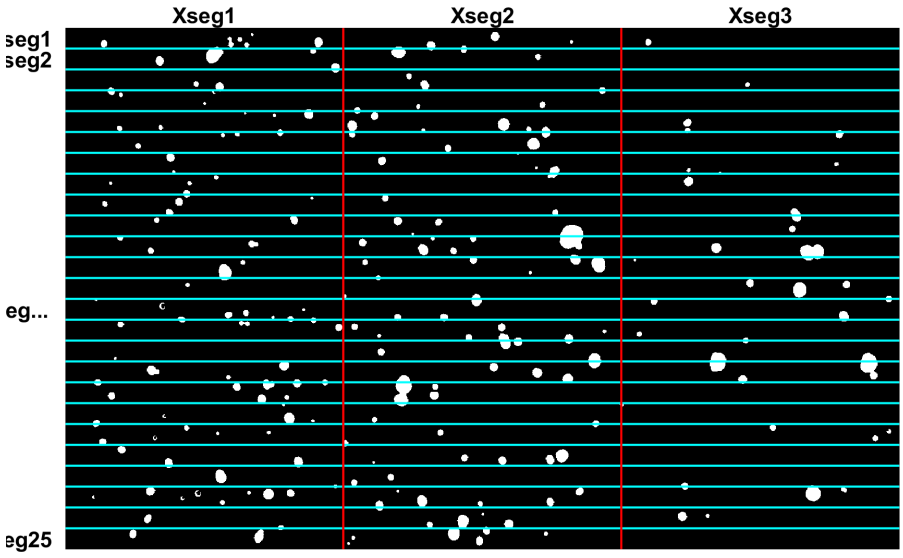

Figure 4.2: Illustration of the segmentation of FOV1. Flow goes from left to right

Ultimately, after processing all pairs of images, the combined results were saved into a single MAT-file for future analysis. This consolidation ensured that all processed data was readily available for

subsequent evaluation (the relevant code can be found in Appendix A.1).

	X_1	X_2	X_3	X_Avg
x/δ	$0-2$	$2-4$	$4-6$	$0-6$
x/D	$0-12$	$12-24$	$24-36$	$0-36$

Table 4.1: Details on the segmentation in the streamwise direction.

4.3. Transitional air layer regime

Within the transitional regime, images were captured at a free-stream velocity of 0.68 m/s. Unlike the bubbly regime, where image pairs were taken at one-second cyclic intervals, continuous image capture was employed for the transitional regime to better capture the dynamic changes in the air layer. The image processing procedure utilized in this regime is detailed as follows.

The preprocessing function, *processImage*, performs several key tasks, including selecting structuring elements based on the air flow rate, detecting edges, closing gaps, opening formations, and filling in holes when required. This preprocessing step is essential to prepare the images for subsequent analysis by enhancing the distinction between the air layer and the surrounding water.

Following preprocessing, the *processAndCombine* function merges the processed images. This function measures the non-wetted area of each processed image, compiles the data into a structured format, and creates a combined image by averaging the processed frames. This combined image represents the overall air layer formation across the captured frames.

One notable challenge in image processing is differentiating between the air layer and the surrounding water, as the air layer often lacks distinct features. However, in this study, the use of a submerged LED panel close to the plate proved advantageous. The presence of noise in the air layer images, introduced by the proximity of the LED, actually facilitated the differentiation between the air and water layers. This noise, contrary to being a hindrance, became a valuable feature, making it easier to identify the boundaries of the air layer, as illustrated in Figure (4.3).

Ultimately, the processed data and the combined images are stored in MAT-files for future analysis, ensuring all processed data is consolidated and easily accessible for subsequent assessments (the relevant code can be found in Appendix A.2).

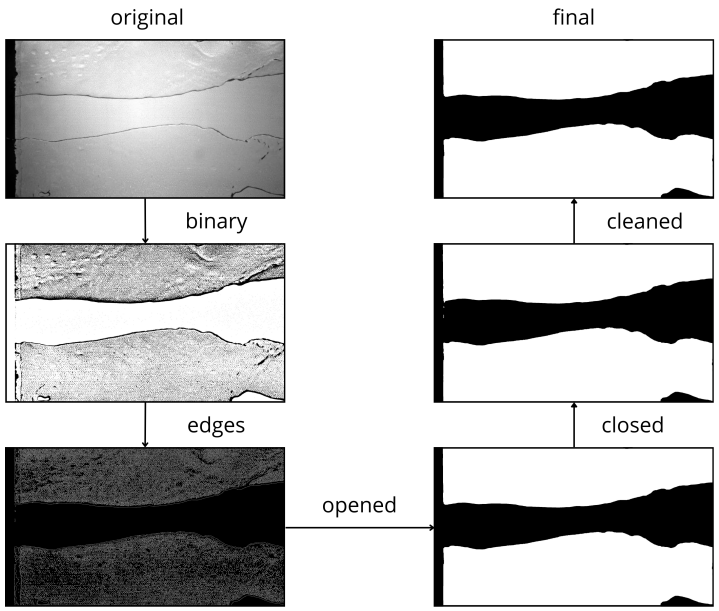

Figure 4.3: Image processing steps for the transitional regime.

4.4. Air layer regime

In the air layer regime, the focus shifted to capturing the continuous air layer formed along the surface of the flat plate. The image processing steps for this regime are described as follows.

After the initial background removal and binarization steps using Davis, the binarized images were further processed in MATLAB. The key task in this regime was to accurately detect the edges of the air layer, which is crucial for understanding its morphology and stability.

The images were binarized at a specific threshold level to distinguish the air layer from the surrounding fluid. Following binarization, the Canny edge detection algorithm was applied to detect the edges of the air layer. This method was chosen for its effectiveness in identifying edges in noisy images, ensuring accurate detection of the air layer boundaries.

After detecting the edges, the air layer's length and thickness were measured. The processed data was saved into MAT-files, similar to the previous regimes, for further analysis. This analysis focused on the stability and continuity of the air layer in the presence of upstream obstacles (the relevant code can be found in Appendix A.4).

A schematic of the image processing steps for the air layer regime is presented in Figure (4.4).

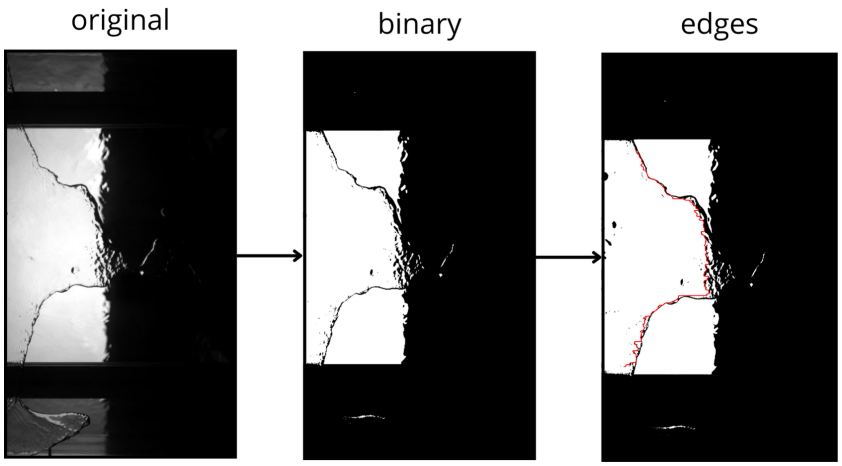

Figure 4.4: Image processing steps for the air layer regime.

The complete MATLAB code for this procedure can also be found in the appendix. By following these steps, the MATLAB code effectively processes the images to analyze the behavior of the air layer, providing valuable insights into its characteristics under varying conditions.

5

Results & Discussion

This chapter presents both the results and their discussion. The structure of the chapter mirrors that of the methodology section. The results are organized and analyzed in order of decreasing free stream velocity. First, the results for a free stream velocity of $U_\infty = 0.94$ m/s are given.

5.1. Bubbly regime

Using the images captured in FOV1 with the cycle-based approach, bubble outlines were identified according to the methodology described in Chapter 3. For each bubble, the area, equivalent diameter (d_B), and centroid coordinates (x_b, y_b) were determined at every time step. The streamwise (U_b) and spanwise (W_b) velocities of the bubbles were then computed by tracking the movement of their centroids between consecutive time steps.

Specifically, at each time step t, the centroid coordinates of the bubbles were recorded. At the subsequent time step $t+1$, the centroids were again determined. By comparing the positions of the centroids at t and $t+1$, the displacement of each bubble was calculated. The streamwise velocity U_b was computed based on the displacement in the x-coordinate, while the spanwise velocity W_b was derived from the displacement in the z-coordinate. This nearest-neighbour approach, used in the code detailed in Appendix A.1, allowed for an accurate estimation of bubble velocities by tracking their movement frame by frame.

During the experiments, some obstacle configurations had a clear effect on the bubble trajectories, which were contained within a spanwise zone of impact. To estimate its extent, the bubble diameters d_B, velocities U_b and W_b, and bubble counts N_b were averaged over the streamwise direction L_x $\left(\overline{U}_b(z) = \overline{U_b(x,z)}\right)$ for both the baseline and all obstacle cases, and were also compared with the corresponding global averages (Figure (5.5a) and Section 5.1.3).

5.1.1. Bubble diameter

The equivalent bubble diameter d_B was computed and analyzed across different obstacle configurations to assess the impact of obstacles on bubble size. In Figure (5.1a), the x-axis has been normalized by δ, and the y-axis by the diameter of the cylinder D. The global mean, depicted in Figure (5.1b), reveals that some obstacle configurations result in a mean bubble diameter $\overline{d}_B$ reduced by 2% to 15.5% compared to the no-obstacle case, except for the L1, h3 configuration. Details can be found in the tables in Appendix.This indicates that the presence of obstacles generally leads to the formation of smaller bubbles.

Furthermore, the data suggest that the positioning of the obstacle plays an important role: obstacles placed at greater distances from the injector appear to have a more pronounced effect on reducing d_B than those placed closer. This observation may point to the possibility that the obstacle disrupts the bubble formation process more effectively when it is positioned further away, potentially due to changes in the wake dynamics.

However, when examining the bubble diameter across different x-segments in Figure (5.2), no significant variation in bubble size is observed downstream. This lack of change suggests that the obstacle's influence is primarily concentrated at the point of bubble formation at the injector, rather than affecting the bubbles as they travel downstream. This could imply that the obstacles alter the initial conditions of bubble formation, but once the bubbles are formed, their size remains largely consistent as they move through the flow.

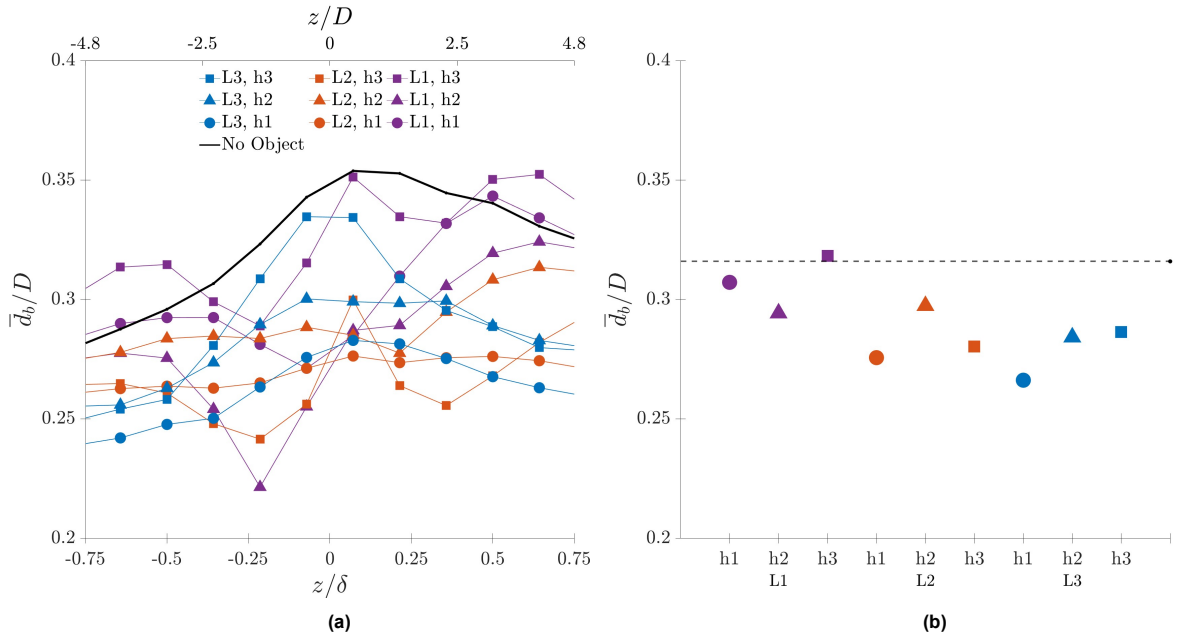

Figure 5.1: (a) Spanwise variation of the average bubble diameter $\overline{d}_B(z)$ and **(b)** global mean of bubble diameters, normalized with the obstacle diameter D, for all obstacle configurations.

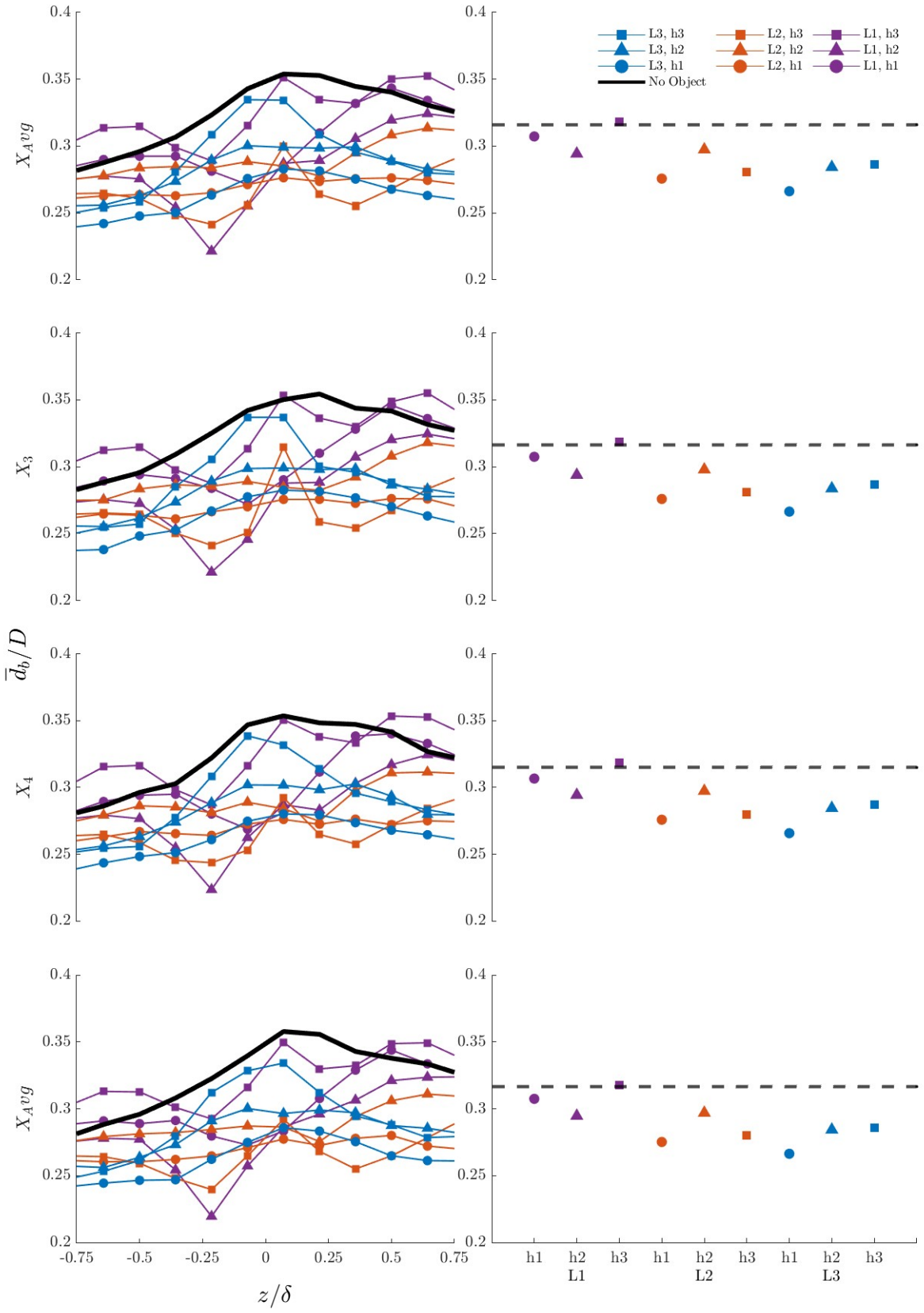

Figure 5.2: Streamwise and spanwise variation of bubble diameters for all configurations. On the left, the spanwise variation is shown where the three plots (X_1-X_3) represent the three X-segments detailed in Figure (4.2), and the bottom plot (X_{Avg}) illustrates the average of these segments. On the right, the plots present the global averages of these segments and the overall total average

5.1.2. Number of bubbles

The analysis of the bubble count N_b was conducted to evaluate the impact of obstacles on bubble distribution. The spanwise variation, shown in Figure (5.3a), indicates that specific obstacles, particularly the $L1, h2$ and $h3$, and $L2, h3$ configurations, significantly reduce N_b within the central region of the flow (-0.5δ to 0.5δ). In contrast, other configurations, such as $L3, h3$ and $L2, h2$, have a lesser effect, while the $h1$ cases appear to have minimal impact on bubble count. It can again be seen that obstacles at a further distance have the biggest effect on the whole span of FOV1.

Interestingly, the global average bubble count, presented in Figure (5.3b), shows a reduction in N_b across all configurations compared to the no-obstacle case. This reduction seems counterintuitive when considering the observed decrease in bubble diameter d_B (as shown in Figure (5.1b)), as one might expect that smaller bubbles would result in a higher overall bubble count due to the conservation of gas volume. However, this expected increase in N_b was not observed, either within or outside FOV1 during the experiments.

The consistent reduction in N_b across all obstacle configurations, coupled with the lack of significant streamwise variation observed in Figure (5.4), suggests that bubbles are likely being pushed laterally out of the wake region created by the obstacles. Examining Figure (5.8a), it is observed that the peak in spanwise velocity W_b aligns with this finding, indicating that bubbles remaining in this region experience a higher W_b, which likely causes them to be pushed laterally outwards.

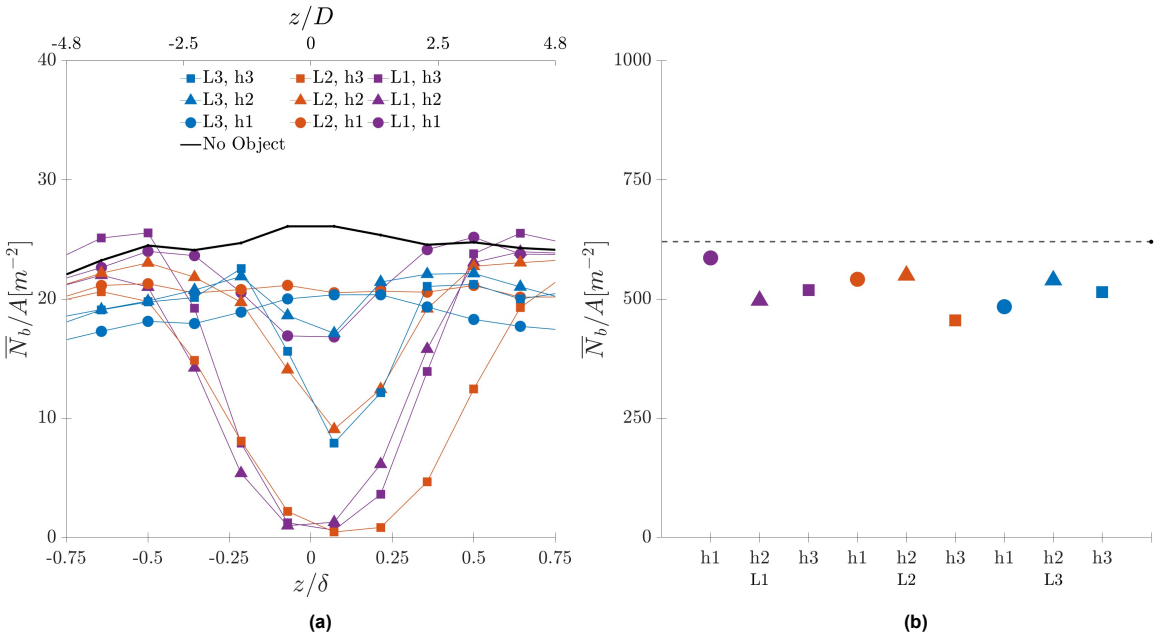

Figure 5.3: **(a)** Spanwise variation of the average bubble count $\overline{N}_b(z)$ and **(b)** global mean of bubble counts for all obstacle configurations.

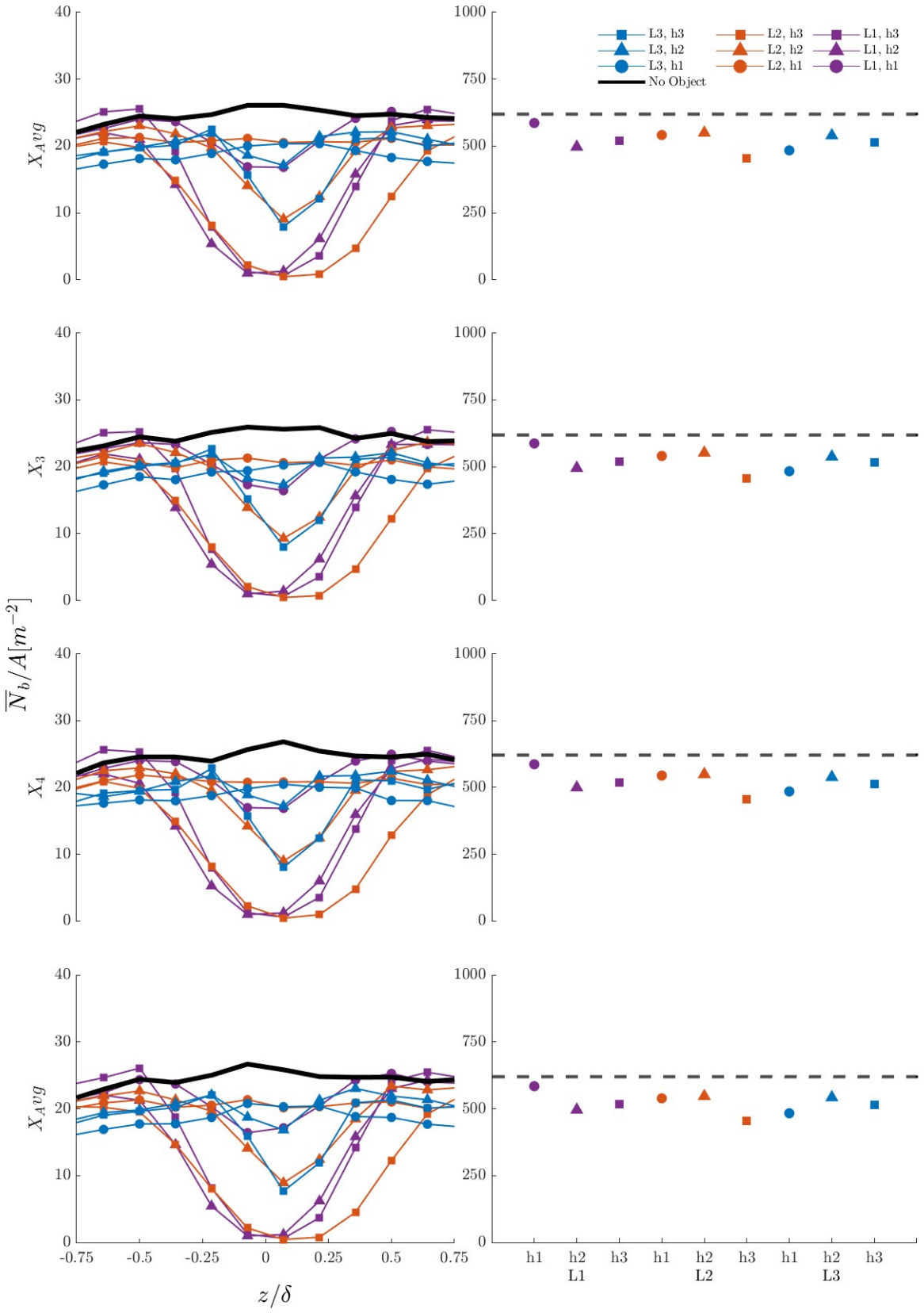

Figure 5.4: Streamwise and spanwise variation of bubble counts for all configurations. On the left, the spanwise variation is shown where the three plots (X_1-X_3) represent the three X-segments detailed in Figure (4.2), and the bottom plot (X_{Avg}) illustrates the average of these segments. On the right, the plots present the global averages of these segments and the overall total average

5.1.3. Bubble velocity

The streamwise velocity U_b and spanwise velocity W_b of the bubbles were determined and normalized by the free stream velocity U_∞.

Streamwise velocity

The global average of the streamwise bubble velocity U_b, shown in Section 5.1.3, indicates no significant variation across different obstacle configurations, although it reduces by up to 2.8% from the no-obstacle case. However, when examining the spanwise variation $U_b(z)$ in Figure (5.5a), a distinct pattern emerges for certain configurations ($L3, h3$; $L2, h3$; and $L1, h3$). In these cases, $U_b(z)$ decreases around (-0.5δ and 0.5δ), reaching a minimum at (-0.25δ and 0.25δ) with a decrease of up to 7% from its baseline value, before increasing to its maximum at approximately 0.05δ, where it rises up to 7.5% above the baseline. Details of this can be found in Appendix B. This behavior suggests that the height of the obstacles has a substantial impact on U_b, with taller obstacles and those placed further downstream from the injector having the most pronounced effect.

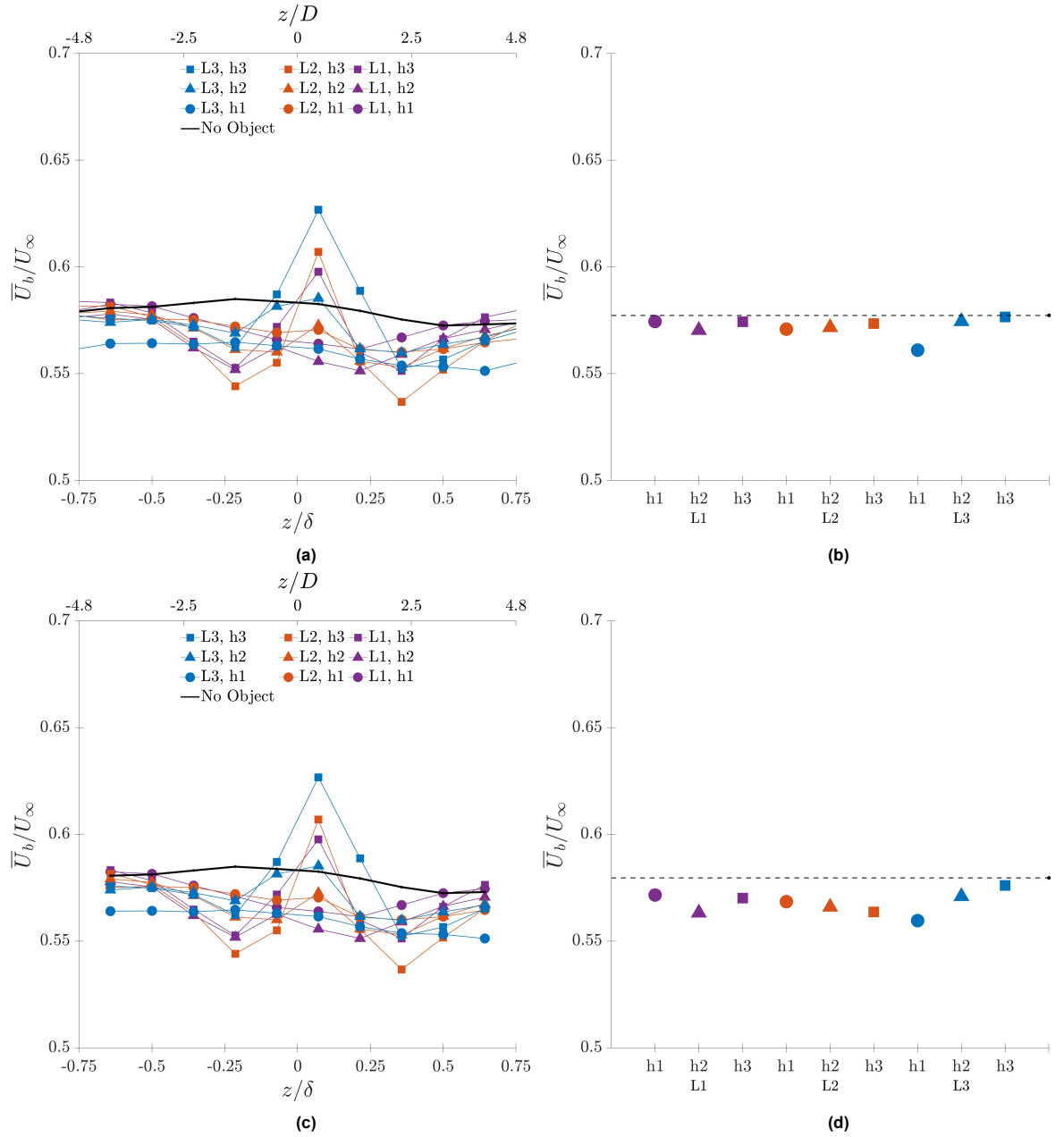

Figure 5.5: **(a)** Spanwise variation of the average bubble streamwise velocity $\overline{U}_b(z)$ and **(b)** global mean of bubble velocities, normalized with $U_\infty = 0.94\,\mathrm{ms}^{-1}$ for all obstacle configurations. **(c)** and **(d)** are zoomed in on the area with the most fluctuations.

To explore this phenomenon in more detail, zoomed-in plots were generated (Figure (5.5c) and Figure (5.5d)). These plots reveal that the observed velocity drop is not symmetrically centered around 0. It can be seen in Figure (5.7) that the peak is centered between $z/\delta = 0$ and $z/\delta = 0.25$ implying that the obstacle may not have been perfectly centered in the flow. Additionally, the region where this decrease and subsequent increase in velocity occurs coincides with areas where the bubble count $N_b(z)$ is low, making it challenging to perform accurate calculations. Despite this limitation, this velocity pattern was also observed in the video recordings of the experiments, suggesting a genuine physical phenomenon.

Interestingly, this behavior is somewhat unexpected, as one would typically anticipate a decrease in velocity within the wake region behind a cylinder. The absence of significant streamwise variation, as shown in Figure (5.6) and Figure (5.7), further supports the idea that the impact of the obstacles is highly localized, affecting the bubbles primarily within the spanwise plane. This suggests that the obstacles

create complex flow dynamics that influence the bubble velocity in a more nuanced way than initially expected.

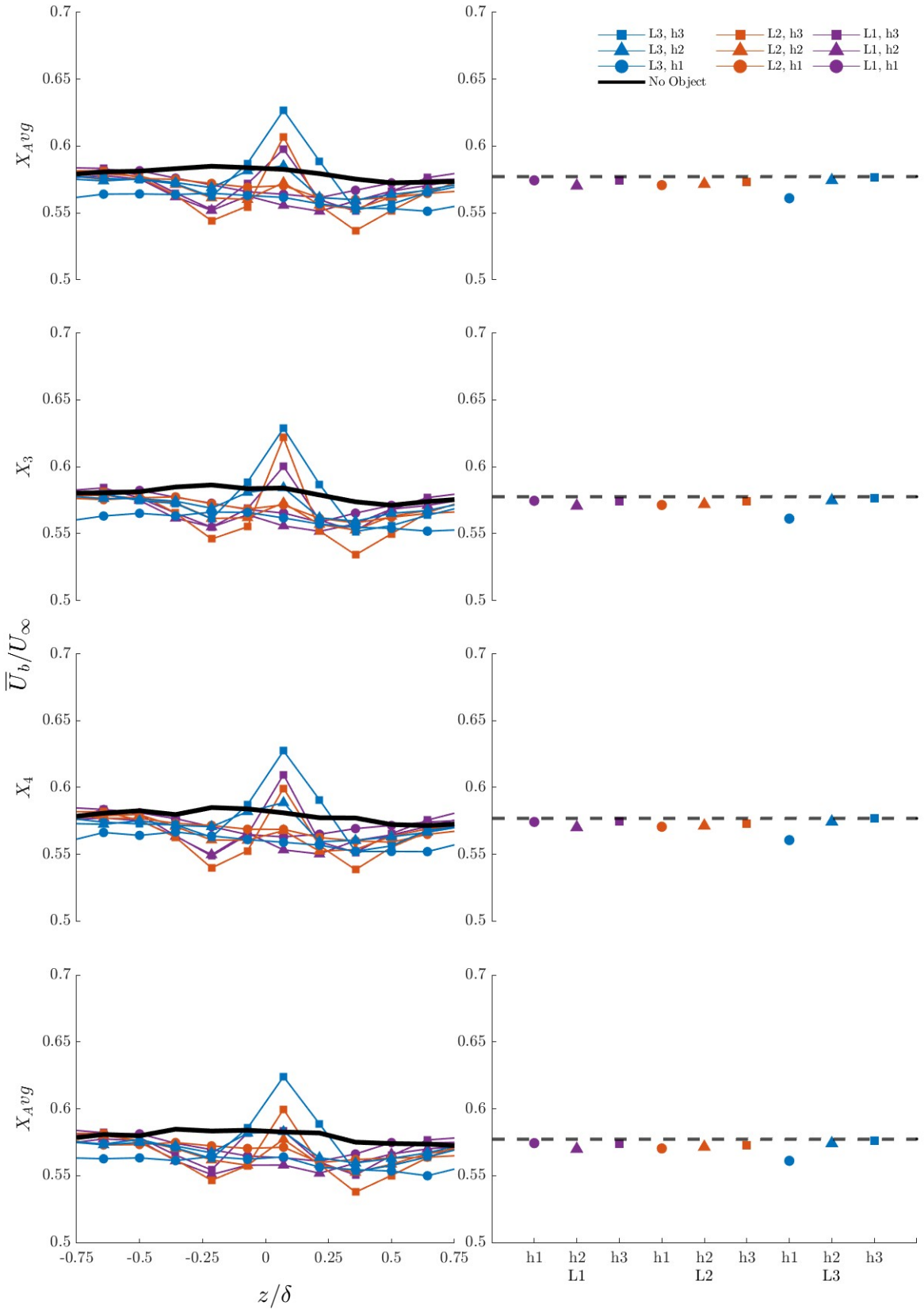

Figure 5.6: Streamwise and spanwise variation of bubble streamwise velocities for all configurations. On the left, the spanwise variation is shown where the three plots (X_1-X_3) represent the three X-segments detailed in Figure (4.2), and the bottom plot (X_{Avg}) illustrates the average of these segments. On the right, the plots present the global averages of these segments and the overall total average

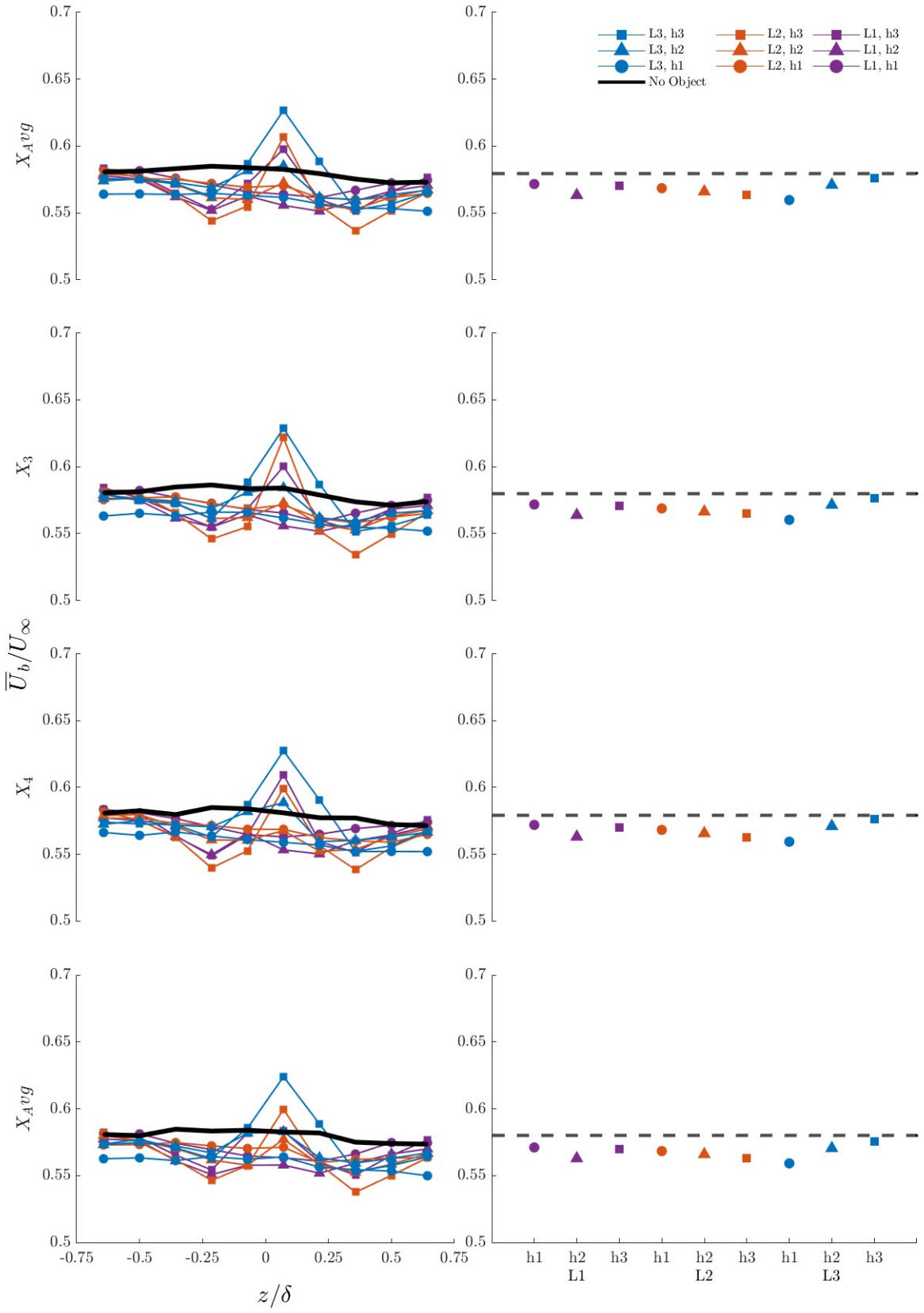

Figure 5.7: Zoomed-in streamwise and spanwise variation of bubble streamwise velocities for all configurations. On the left, the spanwise variation is shown where the three plots (X_1-X_3) represent the three X-segments detailed in Figure (4.2), and the bottom plot (X_{Avg}) illustrates the average of these segments. On the right, the plots present the global averages of these segments and the overall total average

Spanwise velocity

The spanwise velocity W_b was analyzed to understand how it is influenced by the presence of obstacles. As shown in Figure (5.8b), the global mean W_b is slightly negative, which could suggest a slight misalignment of the plate in the water tunnel.

The spanwise variation in $W_b(z)$, illustrated in Figure (5.8a), reveals that certain obstacle configurations ($L1, h3$; $L1, h2$; and $L2, h3$) have a noticeable impact on W_b, particularly around -0.5δ and 0.5δ. This pattern suggests that the bubbles are being pushed laterally out of the wake region created by the obstacles, which aligns with the trends observed in the bubble count N_b analysis.

However, it's important to note that in the regions where these changes in $W_b(z)$ are most pronounced, the bubble count $N_b(z)$ is relatively low, which limits the precision of the velocity calculations in these areas. Despite this limitation, the observed shifts in spanwise velocity were consistently captured in the video footage of the experiments. This increase in $W_b(z)$ likely contributes to the lateral displacement of bubbles, pushing them out of the wake region created by the obstacles. This displacement, in turn, reduces the local bubble count, $N_b(z)$, indicating a direct link between the spanwise velocity and the observed reduction in bubbles within these regions.

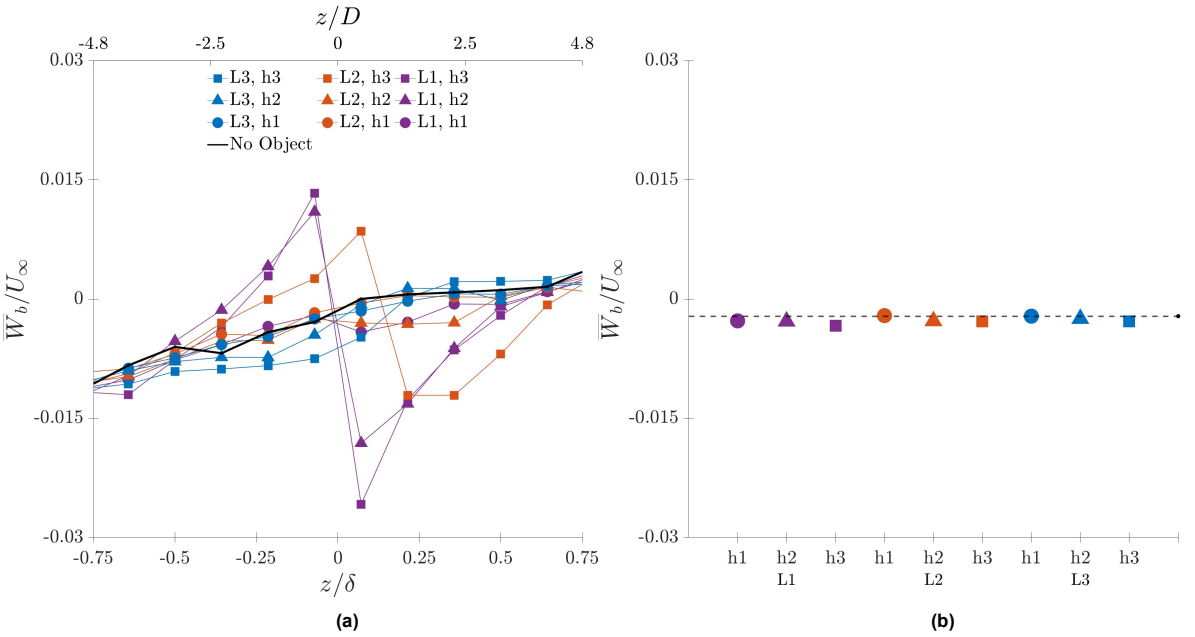

Figure 5.8: **(a)** Spanwise variation of the average bubble spanwise velocity $\overline{W}_b(z)$ and **(b)** global mean of bubble velocities, normalized with $U_\infty = 0.94\,\mathrm{ms}^{-1}$ for all obstacle configurations.

5.1.4. Discussion

The results from the bubbly regime experiments reveal complex interactions between the flow dynamics and obstacle configurations, which align with and extend the insights gained from the literature. The reduction in equivalent bubble diameter d_B observed across nearly all obstacle configurations suggests that the obstacles are disrupting the initial bubble formation process at the injector. This phenomenon is consistent with findings from previous studies, such as those by Serizawa and Kataoka (1990) and Xu, Maxey, and Karniadakis (2002), which highlight the sensitivity of bubble size to upstream flow conditions and disturbances. Smaller bubble sizes, as observed in most configurations, can be attributed to the enhanced mixing and shear induced by the obstacles, which fragment larger bubbles into smaller ones (Xu, Maxey, and Karniadakis 2002; Pang, Wei, and Yu 2013) .

Interestingly, the L1, h3 configuration, which results in a slightly larger d_B compared to other configurations, points to the nuanced role that obstacle height and positioning play. This suggests that specific configurations might stabilize certain flow structures, allowing larger bubbles to persist despite the general trend of bubble size reduction. This outcome reflects the complexity of flow-structure interactions highlighted in the literature, where the interplay between flow stability and turbulence intensity can lead

to varied outcomes depending on the exact experimental setup (Sumner, Heseltine, and Dansereau 2004; Zdravkovich 1997).

The analysis of bubble count N_b offers further insights into these interactions. The observed reduction in $N_b(z)$ across all obstacle configurations, particularly within the central region of the flow (-0.5δ to 0.5δ), suggests that obstacles not only reduce bubble size but also displace bubbles laterally. This displacement could be linked to the wake dynamics of the obstacles, which push bubbles out of the central flow region, as observed in the spanwise velocity $W_b(z)$ results. The literature supports this interpretation, with studies showing that wakes behind bluff bodies can significantly alter downstream flow structures and transport phenomena, including bubble trajectories (Sumner, Heseltine, and Dansereau 2004; Porteous, Moreau, and Doolan 2014) .

The recurring impact zone at -0.5δ and 0.5δ, evident in both the $U_b(z)$ and $W_b(z)$ results, points to a consistent region of influence where the obstacles most strongly affect bubble dynamics. The spanwise variation in $U_b(z)$ and $W_b(z)$, particularly the unexpected patterns observed in specific configurations (such as $L3, h3$; $L2, h3$; and $L1, h3$), underscores the importance of obstacle aspect ratio h/D, and positioning. The observed decrease in $U_b(z)$ followed by a localized increase suggests that these obstacles may be introducing secondary flow structures or altering the primary wake in a way that accelerates bubbles in specific regions.

The lack of significant streamwise variation in both $U_b(z)$ and $W_b(z)$ suggests that the effects of the obstacles are consistent along the streamwise direction but remain confined to specific spanwise zones. This implies that while the bubble motion is predominantly influenced laterally, the streamwise effects do not disappear; rather, they remain spatially constrained within these zones. The observed patterns across all streamwise locations indicate that bubbles do not revert to baseline behavior, supporting the persistence of the lateral flow structures generated by the obstacles. Despite some limitations in the low bubble count $N_b(z)$ in regions of significant velocity change, the consistent trends observed across different datasets confirm the robustness of these spanwise-dominated structures.

In summary, the interaction between obstacles and bubble dynamics in the bubbly regime is complex and multifaceted, with significant implications for drag reduction strategies using gas injection. The findings highlight the critical role of obstacle configuration in shaping flow dynamics and bubble behavior, with consistent patterns emerging in specific regions of the flow. These results extend the existing body of literature by providing detailed insights into how upstream modifications can influence downstream flow structures and bubble dynamics, offering new avenues for optimizing flow control techniques in turbulent boundary layers.

5.2. Transitional regime

In the transitional regime, images were captured continuously in FOV1, allowing for detailed observation of air distribution within the flow. The regions containing air were identified using the methodology described in Chapter 3. The mean non-wetted area, $\overline{A}_{nw}$, was determined for both the baseline and the various obstacle configurations.

Contours were generated to visualize the probability of air presence within the flow. Certain obstacle configurations were observed to have a noticeable impact within a specific zone, referred to as the zone of impact. This zone of impact was analyzed by measuring its extent and examining its variation along the streamwise direction.

5.2.1. Non-wetted area

The transitional regime was explored by analyzing how the non-wetted area ($\overline{A}_{\text{nw}}$) evolves with varying air flow rates (Q_{air}) across different obstacle configurations. In Figure (5.9), the behavior of $\overline{A}_{\text{nw}}$ reveals three distinct phases. Initially, for air flow rates between $Q = 6.0$ and 12 l/min, the system remains in the bubbly regime, characterized by smaller and more dispersed air pockets. As the air flow increases, a sharp rise in the non-wetted area occurs, signaling the onset of the transitional regime, which spans air flow rates from $Q = 18$ to 36 l/min.

During this transitional phase, it is interesting to note that the differences in $\overline{A}_{\text{nw}}$ between the ”No obstacle” and obstacle configurations are relatively minor. This suggests that the initial stages of air flow

increase lead to a more uniform distribution of air within the flow, regardless of the presence of obstacles. However, at $Q = 36$ l/min, a sudden rise in $\overline{A}_{\text{nw}}$ is observed for the obstacle configurations, followed by a plateau. This behavior indicates the onset of the air layer regime for these cases, suggesting that the obstacles cause the air layer to stabilize more quickly.

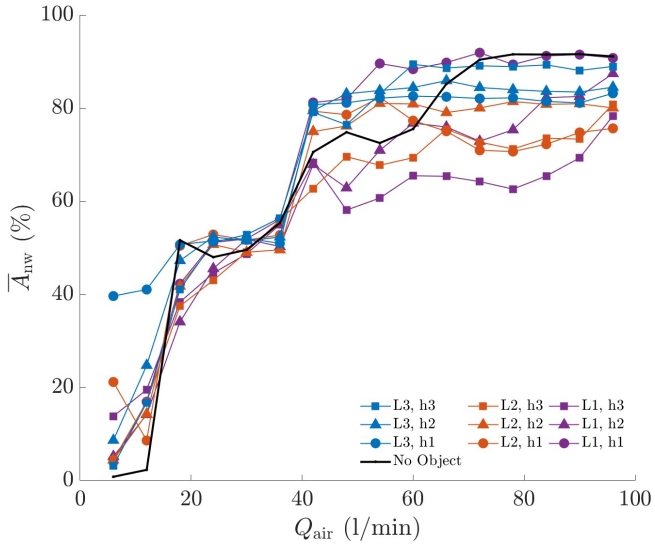

Figure 5.9: Mean non-wetted area ($\overline{A}_{\text{nw}}$) as a function of air flow rate (Q_{air}) for various obstacle configurations.

In contrast, the baseline scenario without any obstacles shows a different pattern. While $\overline{A}_{\text{nw}}$ continues to increase steadily beyond $Q = 36$ l/min, it does not plateau until reaching $Q = 72$ l/min. This suggests that for the no-obstacle case, the air layer regime begins later, requiring a higher air flow rate to fully establish. This plateau effect, which occurs earlier in the presence of obstacles, can be attributed to the way these obstacles influence the flow dynamics, potentially disrupting the uniform distribution of air and leading to a more rapid stabilization of the non-wetted area. It's important to clarify that when $\overline{A}_{\text{nw}}$ approaches 100%, this does not indicate complete coverage of the plate, but rather that the observed field of view (FOV) is fully covered by air pockets. This distinction is crucial for understanding the limitations of the measurement and the extent to which air coverage is achieved within the observed area.

Overall, the transition from the bubbly to the transitional regime highlights the complex interplay between air flow rate, obstacle configuration, and the resulting distribution of air within the flow. The sudden rise and subsequent plateau in $\overline{A}_{\text{nw}}$ at different air flow rates for the obstacle and no-obstacle cases provide key insights into the onset of the air layer regime, demonstrating how these factors combine to influence the efficiency and stability of air layer formation under varying conditions.

The contours in Figure (5.11) show that for certain configurations ($L1, h2$ and $h3$, and $L2, h3$), the obstacle has a major impact, resulting in an area where there is no air present. This is visible across all Q_{air} values, where blue indicates no air and yellow indicates a high probability of air presence. Other obstacle configurations seem to have less of an effect on the probability of air being present, which is more visible at higher air flow rates, especially in the $L2, h2$ case. The shape of the region where no air is visible is consistent across the obstacles ($L1, h3$ and $h2$, and $L2, h3$). This shape resembles a funnel, starting narrow and widening suddenly at a certain streamwise distance before stabilizing again.

This pattern suggests that the proximity of the obstacle to the injector, as well as the height of the obstacle, significantly influences the formation of the non-wetted area, which is critical for optimizing drag reduction. As discussed by Elbing et al. (2008), a more stable and uniform air layer is essential for minimizing skin friction drag, particularly in the transitional and air layer regimes. Obstacles that disrupt the uniformity of the air layer can lead to increased drag by creating areas where the air layer is incomplete or unstable, thus reducing the overall effectiveness of the drag reduction technique. For

instance, obstacles placed closer to the injector ($L1$) with greater heights ($h3$) appear to have the most pronounced effect, indicating that these factors may amplify the wake effects and alter the distribution of air more significantly than other configurations. Conversely, the smallest obstacle ($h1$) seems to have minimal impact on the non-wetted area, regardless of its position, except at the closest and farthest distances, where it still contributes to higher non-wetted areas at lower flow rates.

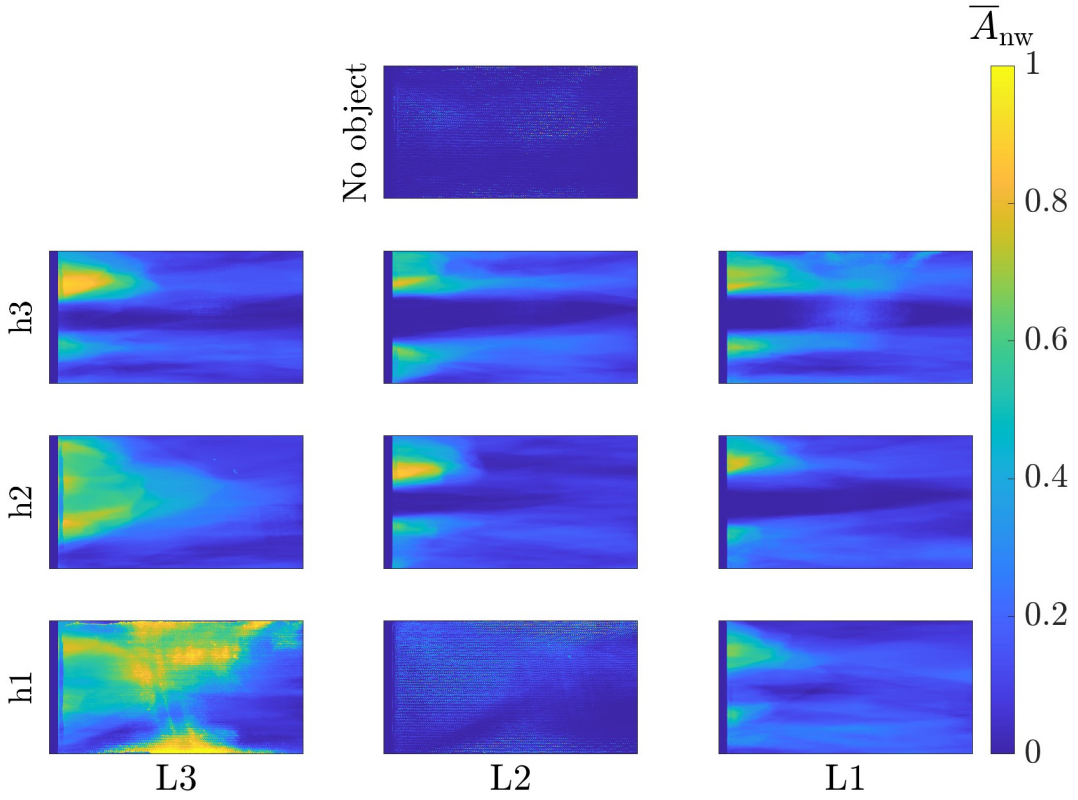

(a) $Q_{air} = 12.0$ l/min

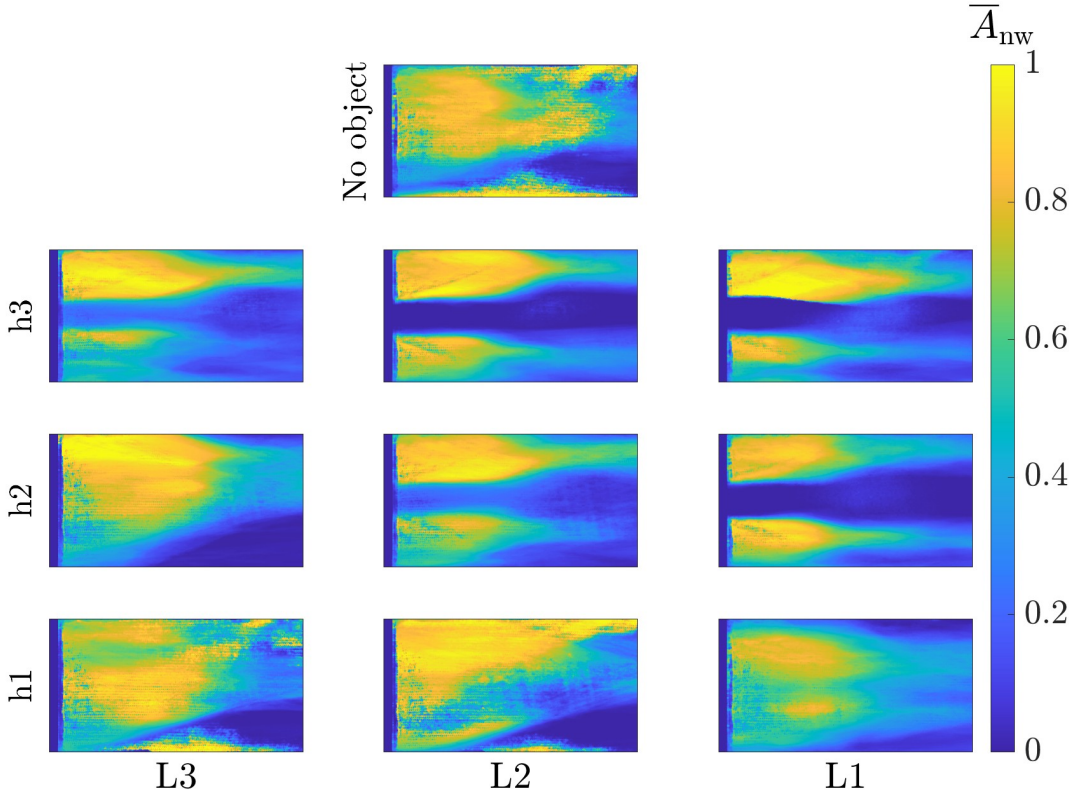

(b) $Q_{air} = 18.0$ l/min

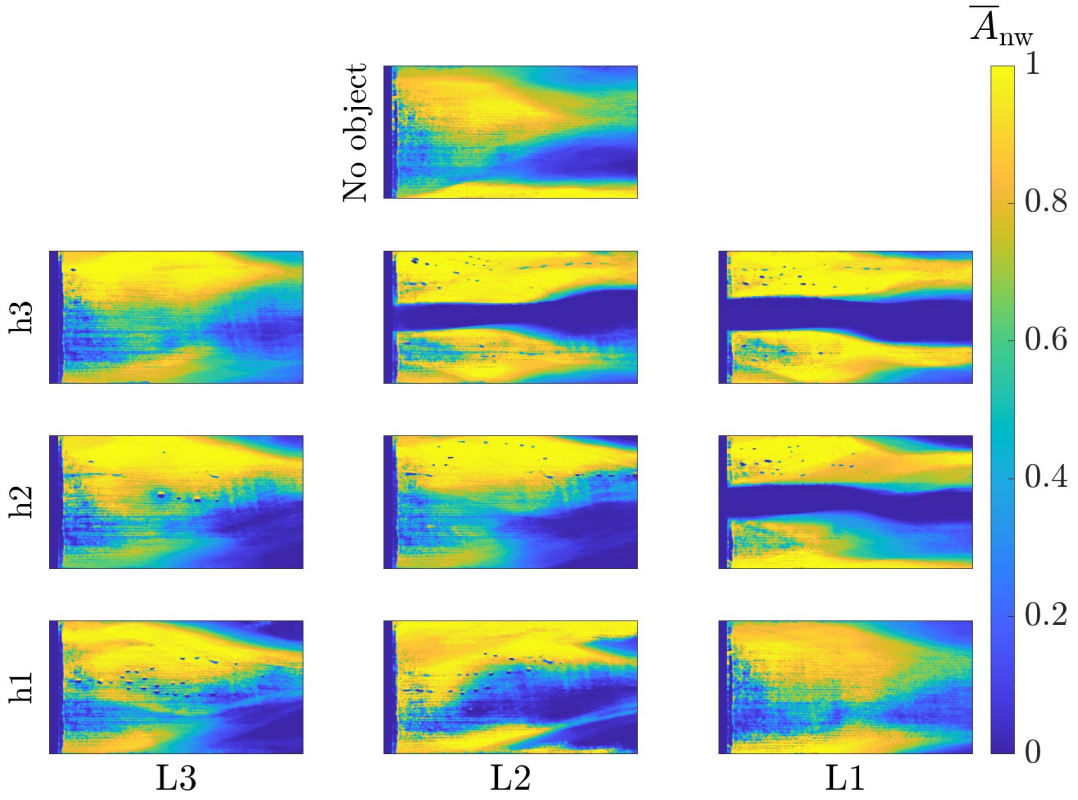

(c) $Q_{air} = 36.0$ l/min

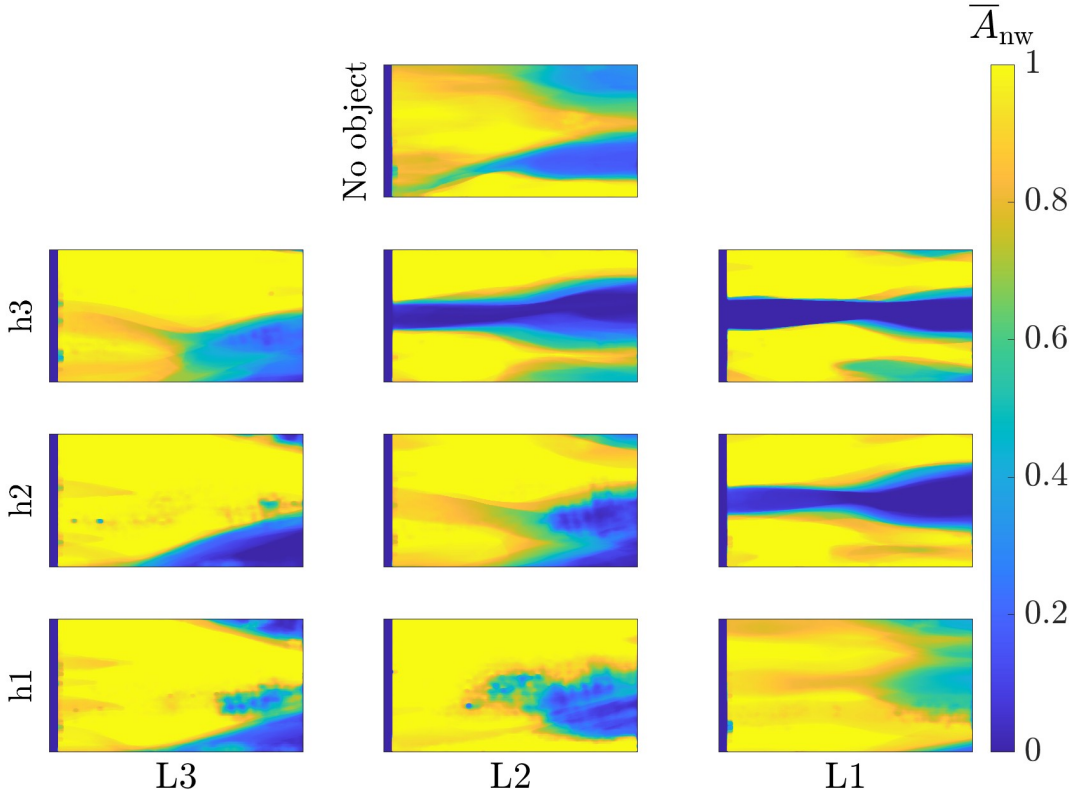

(d) $Q_{air} = 42.0$ l/min

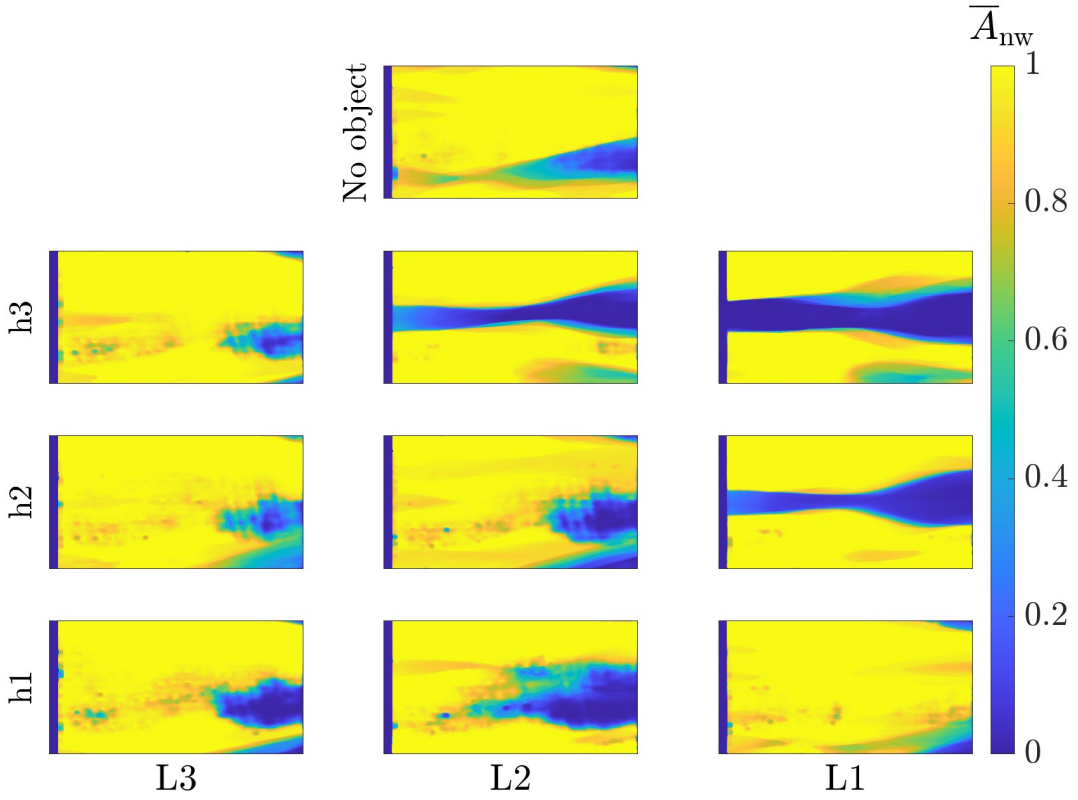

(e) $Q_{air} = 66.0$ l/min

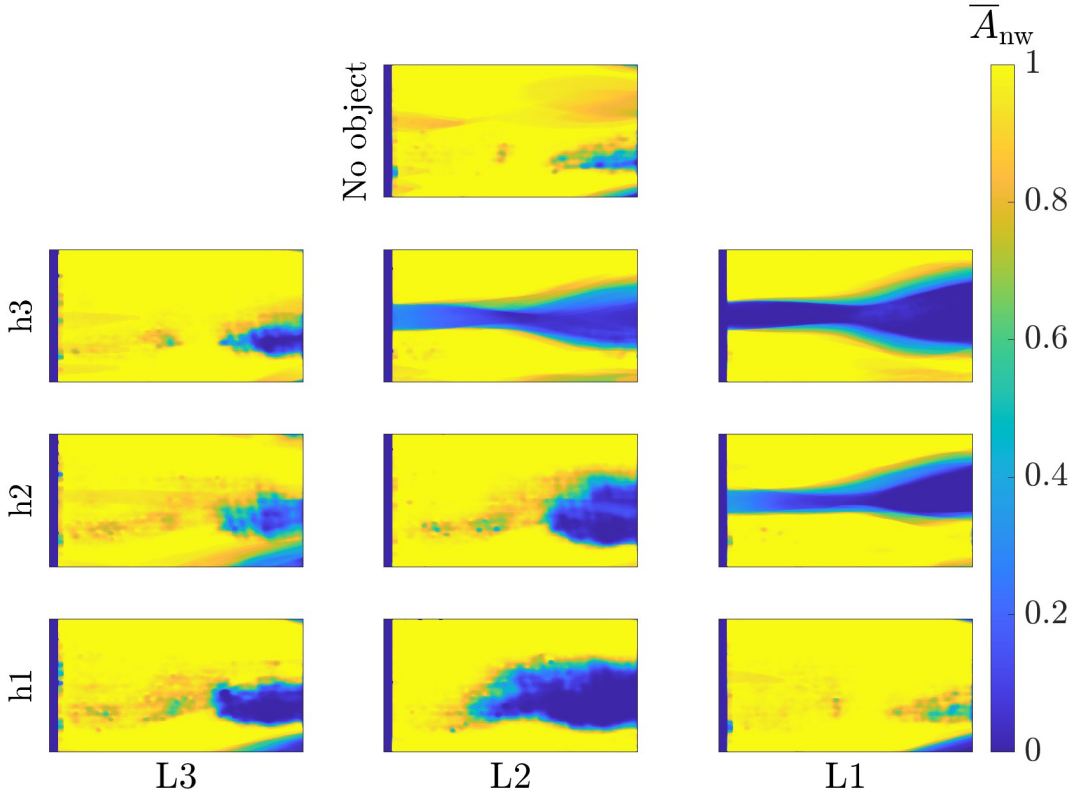

(f) $Q_{air} = 72.0$ l/min

Figure 5.10: Contours of the mean non-wetted area ($\overline{A}_{\text{nw}}$) for air flow rates $Q_{\text{air}} = 12.0$ l/min (a), $Q_{\text{air}} = 18.0$ l/min (b), $Q_{\text{air}} = 36.0$ l/min (c), $Q_{\text{air}} = 42.0$ l/min (d), $Q_{\text{air}} = 66.0$ l/min (e) and $Q_{\text{air}} = 72.0$ l/min (f) across different obstacle configurations. The color scale indicates the probability of air presence within the flow field.

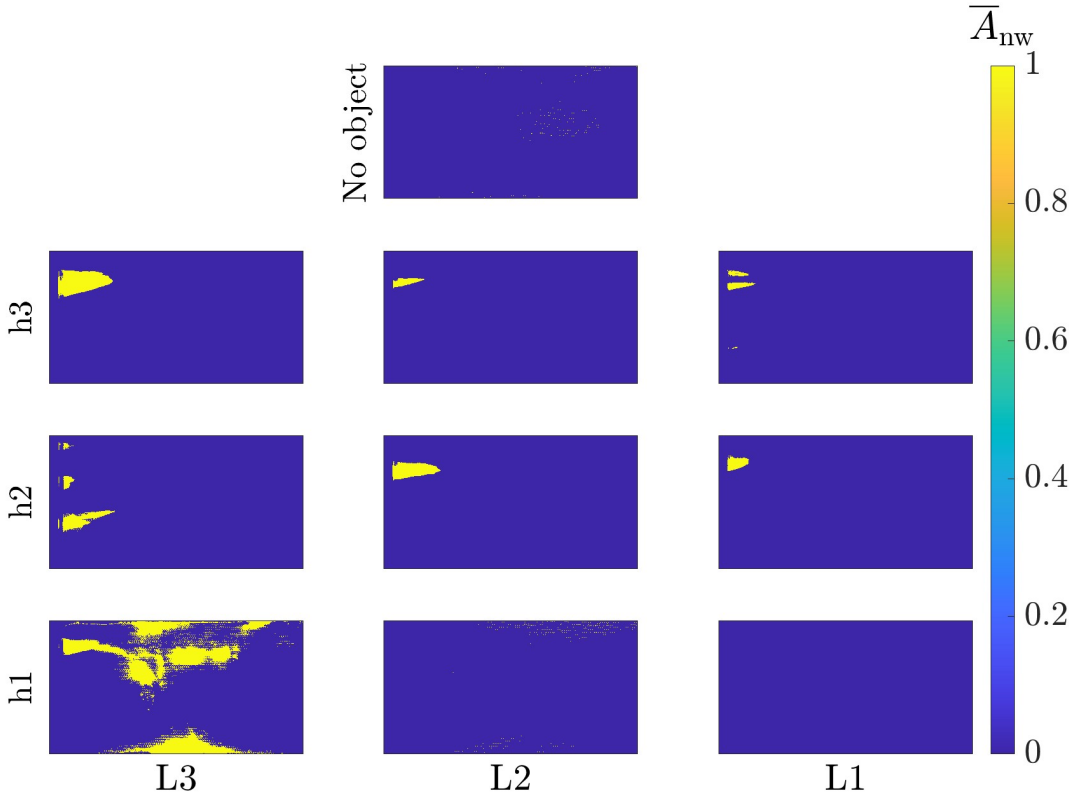

(a) $Q_{air} = 12.0$ l/min

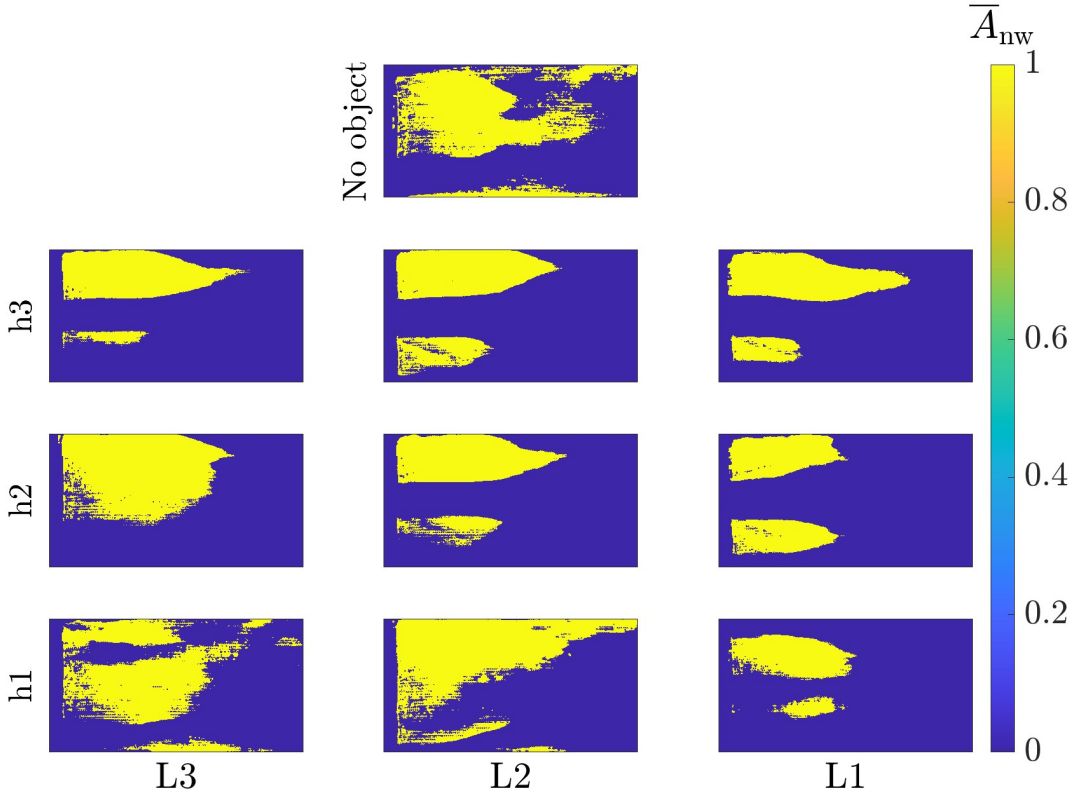

(b) $Q_{air} = 18.0$ l/min

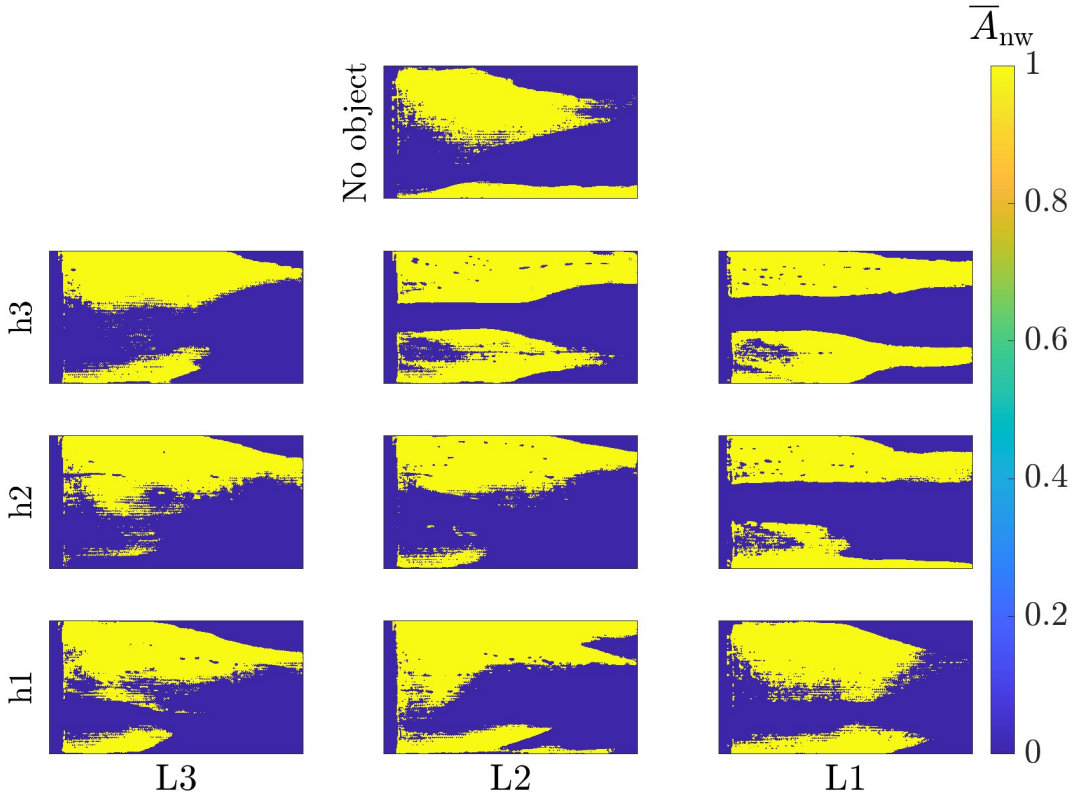

(c) $Q_{air} = 36.0$ l/min

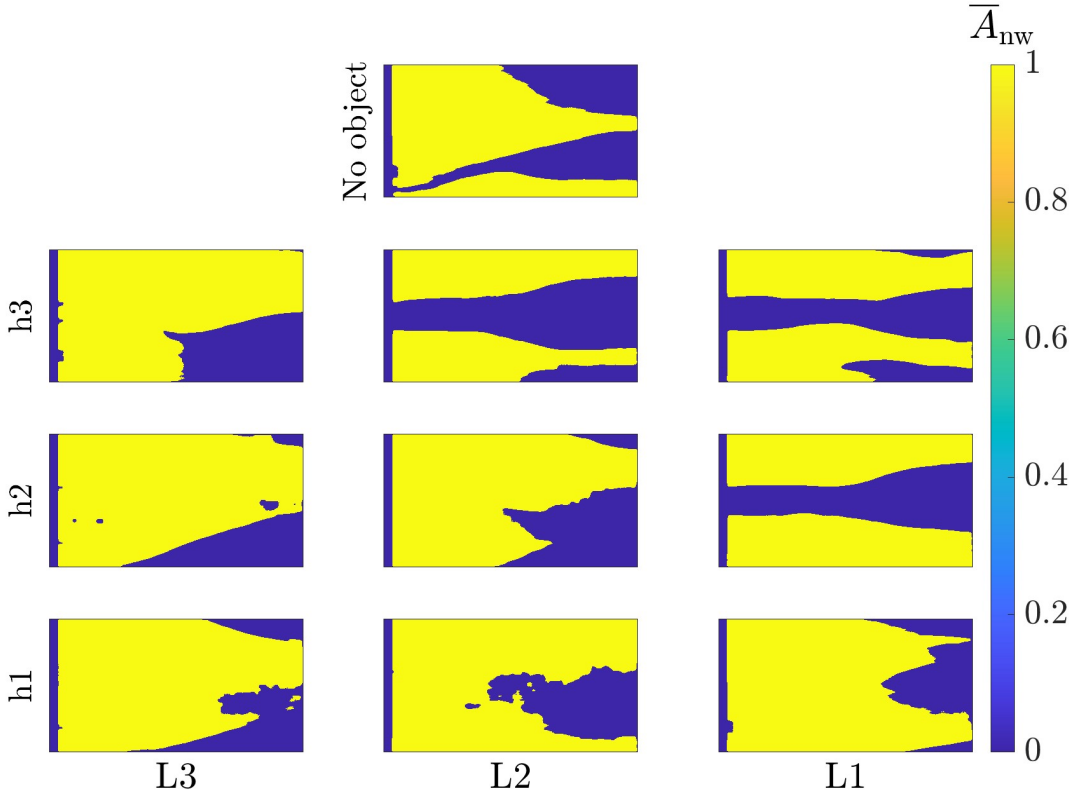

(d) $Q_{air} = 42.0$ l/min

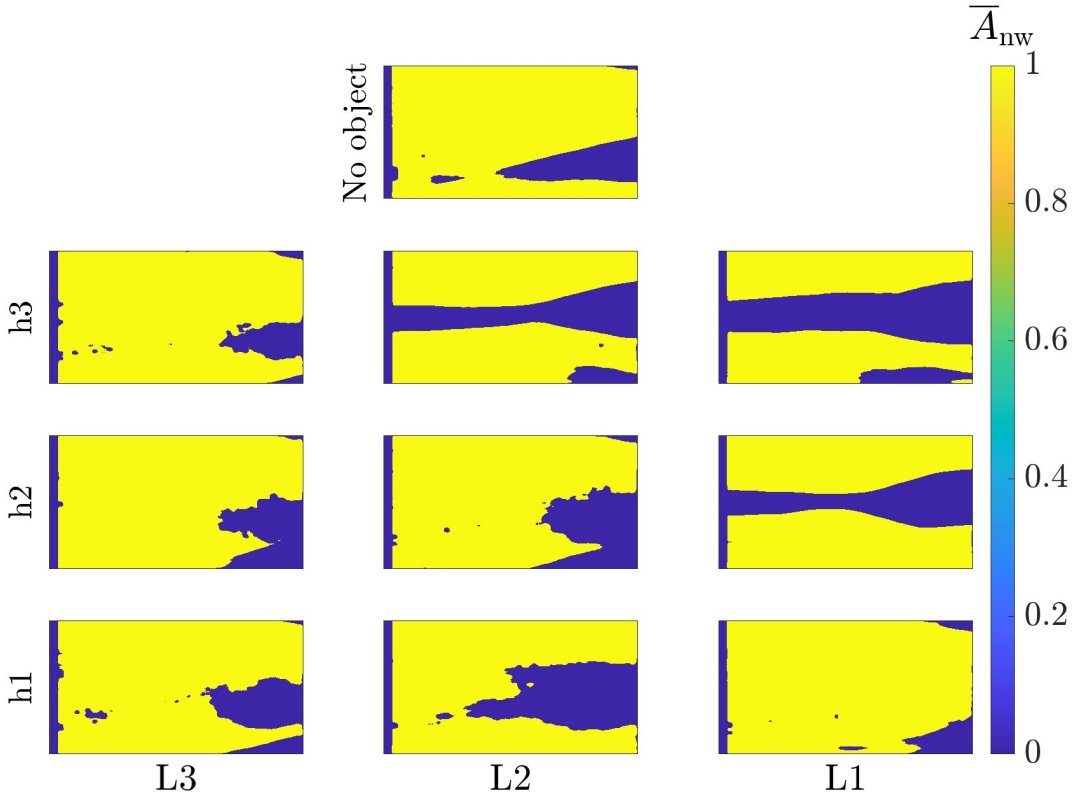

(e) $Q_{air} = 66.0$ l/min

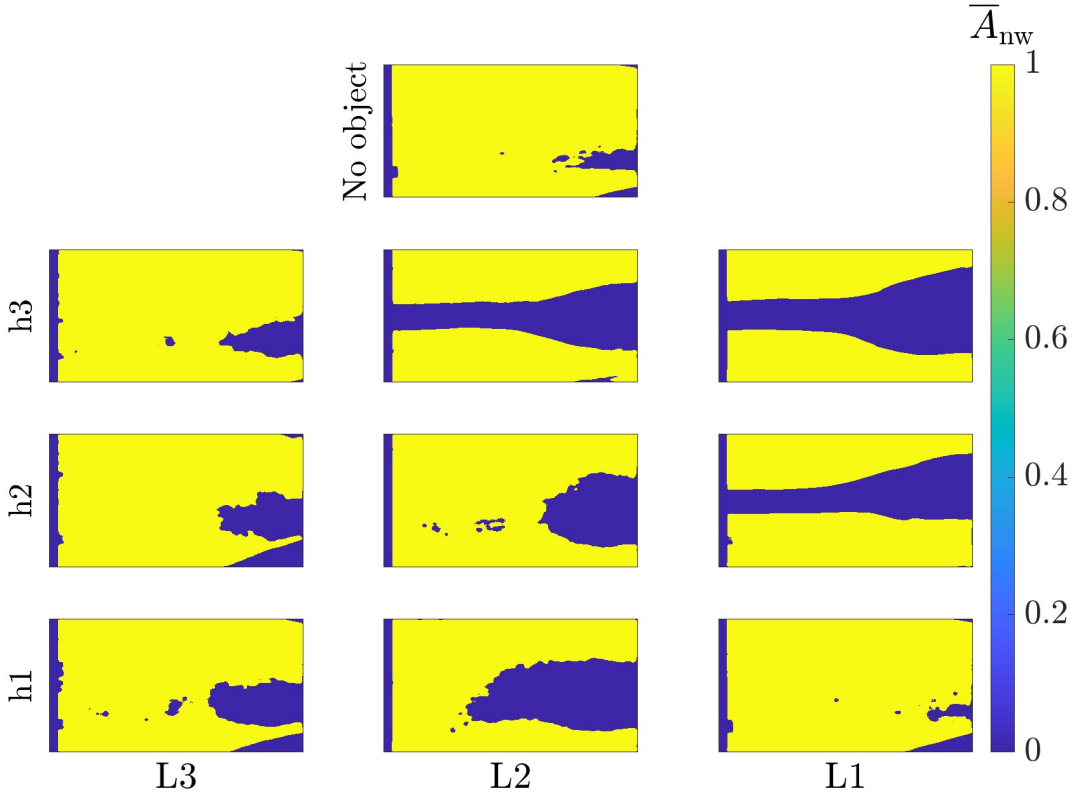

(f) $Q_{air} = 72.0$ l/min

Figure 5.11: Contours of the mean non-wetted area ($\overline{A}_{\mathrm{nw}}$) for air flow rates $Q_{\mathrm{air}} = 12.0$ l/min (a), $Q_{\mathrm{air}} = 18.0$ l/min (b), $Q_{\mathrm{air}} = 36.0$ l/min (c), $Q_{\mathrm{air}} = 42.0$ l/min (d), $Q_{\mathrm{air}} = 66.0$ l/min (e) and $Q_{\mathrm{air}} = 72.0$ l/min (f) across different obstacle configurations. The color scale indicates the probability of air presence within the flow field. Thresholded at $\overline{A}_{\mathrm{nw}} = 0.7$.

To further investigate the phenomenon of funnel formation in the non-wetted region, a methodical approach was employed. First, a threshold was applied to the contours to clearly define the edges of the no-air zone. A threshold value of 0.7 was selected, as it provided a consistent and accurate depiction of the region. Importantly, this threshold was chosen because no significant changes were observed when slightly increasing or decreasing it, indicating that the identification of the funnel edges was relatively stable across different threshold values.

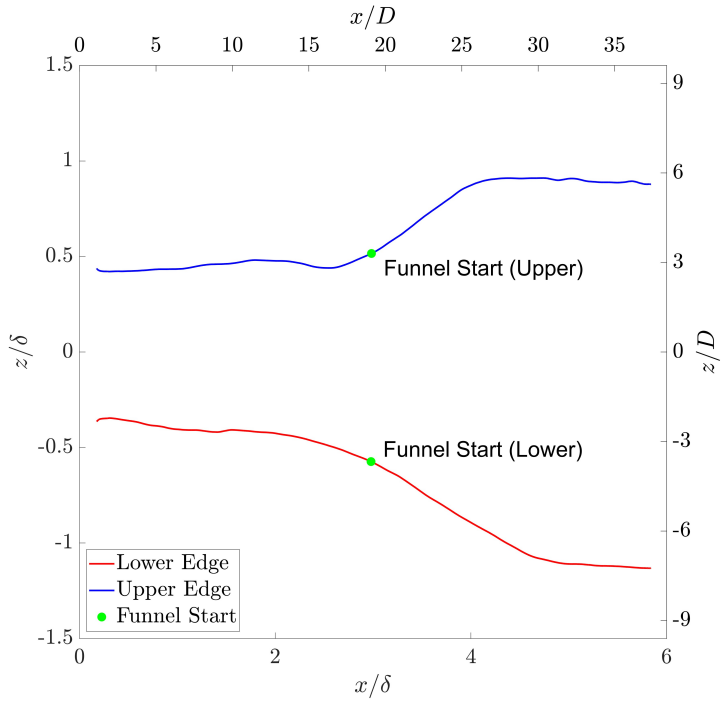

Figure 5.12: Detection of the ZOI edges and identification of the funnel start for configuration L2, h3 at $Q_{\text{air}} = 66.0\,\text{l/min}$.

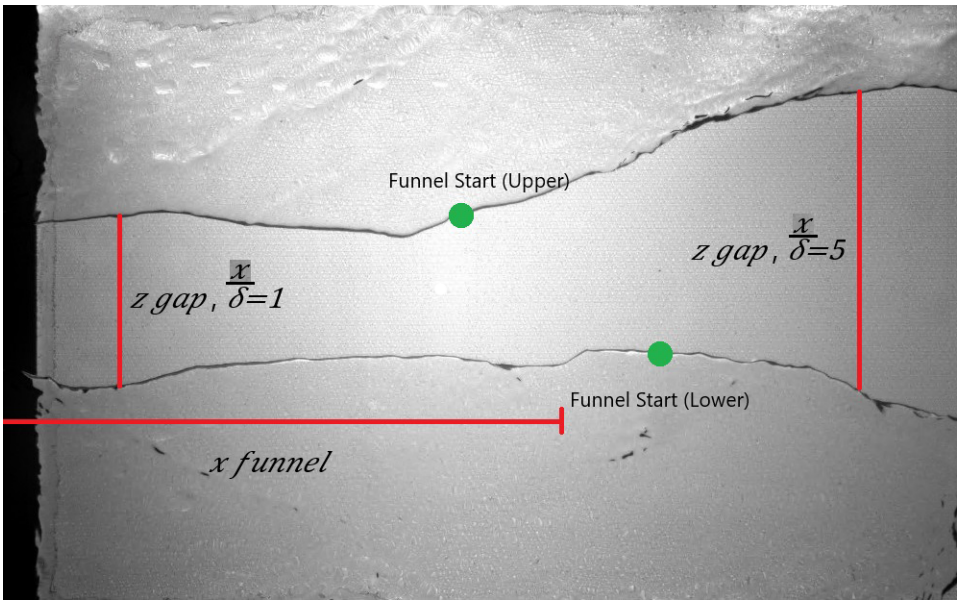

Figure 5.13: Raw image with depiction of Funnel Start, x_{funnel} (Figure (5.14a)) and z_{gap} (Figure (5.14b) Figure (5.14c)).

Following the thresholding, the edges of the non-wetted region were detected, focusing on the upper

edge $z_u(x)$ and the lower edge $z_l(x)$ of the air opening. These edges were smoothed using a moving average with a window size of 50 columns to minimize noise and enhance accuracy. The code implementation for this method is detailed in Appendix A.3.

The cumulative derivative method was then employed to pinpoint the exact location where the funnel begins to widen. This method involves calculating the cumulative trend $S(x)$ over a specified window of columns w:

$$S_u(x) = \sum_{i=x-w}^{x+w} (z_u(i) - z_u(i-1))$$

$$S_l(x) = \sum_{i=x-w}^{x+w} (z_l(i) - z_l(i-1))$$

A significant downward trend in $S_u(x)$ or an upward trend in $S_l(x)$ signals the onset of the funnel widening. The funnel start is marked when the cumulative deviation $S(x)$ exceeds a threshold of 2.4, indicating a notable shift in the edge positions.

With this stable threshold, the start of the funnel was consistently identified at approximately $x = 3\delta$, with only minor variations observed across different configurations and flow rates. Subsequently, the width of the no-air region was analyzed at specific streamwise positions, namely $x = \delta$ and $x = 5\delta$, to assess how the presence of obstacles influenced air distribution further downstream. At $x = \delta$, the width of the non-wetted area was observed to be fairly consistent, aligning with the impact zone identified in the bubbly regime, spanning from -0.5δ to 0.5δ, or approximately 1δ in width. As the air flow rate increased, a slight decrease in this width was noted. At $x = 5\delta$, the gap widened, centering between 1.5δ and 2δ. While the differences between obstacle configurations were minor, a subtle decrease in width was still discernible.

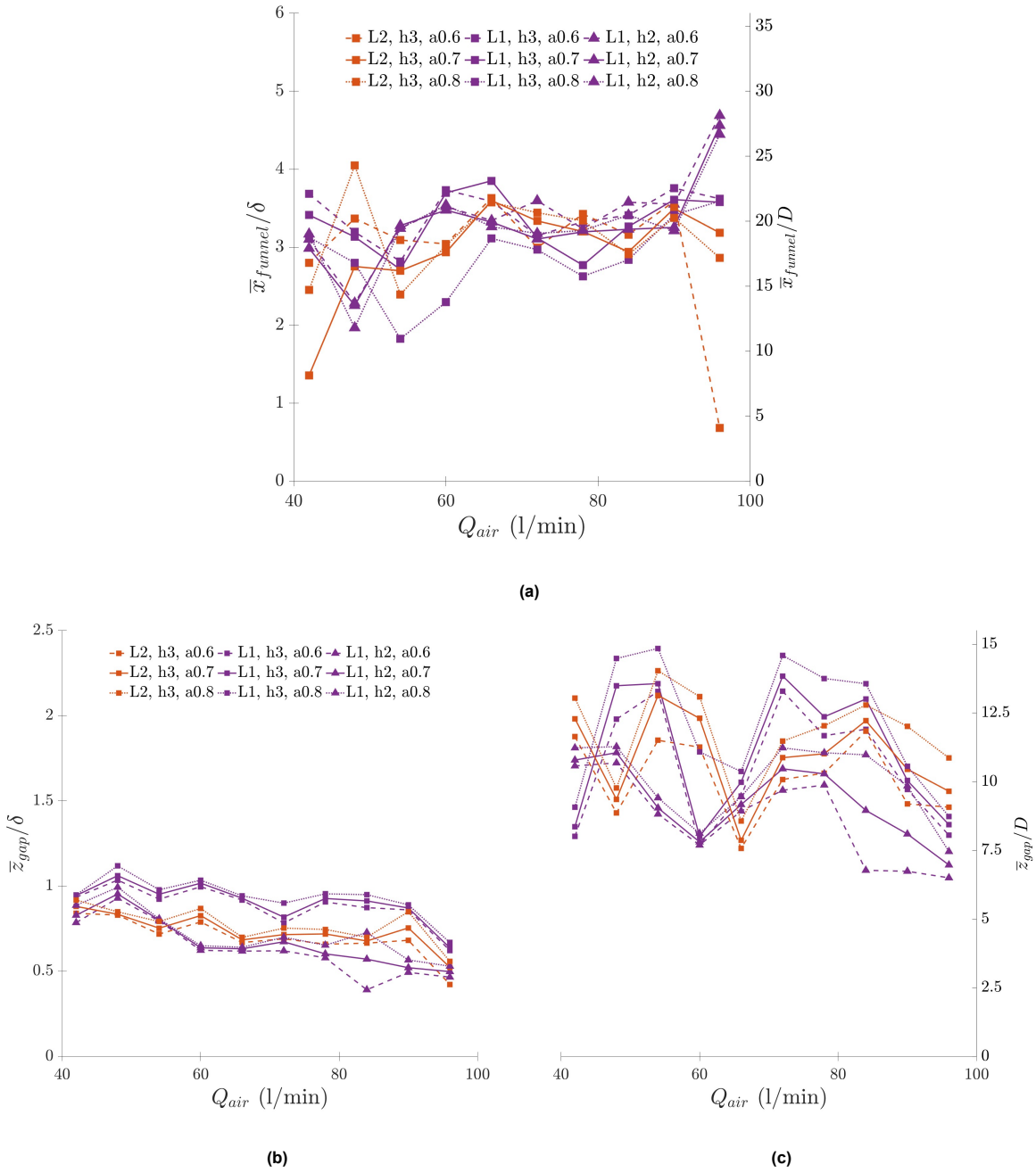

Figure 5.14: (a) Streamwise position of the funnel start x_{funnel}/δ as a function of air flow rate Q_{air} for configurations $L1, h2$; $L1, h3$; and $L2, h2$. Spanwise gap z_{gap}/δ between the upper and lower ZOI edges at $x/\delta = 1$ **(b)** and **(c)** $x/\delta = 5$ as a function of air flow rate Q_{air} for configurations $L1, h2$; $L1, h3$; and $L2, h2$.

The observations from the transitional regime suggest that the wake region of the cylinder likely has a significant impact on the behavior of the non-wetted area. However, quantifying this impact is challenging without access to velocity fields, which were not available in this study. It is hypothesized that the wake region has the most substantial effect on the flow dynamics and, consequently, on the air distribution. The analysis also reveals that the closer the obstacle is to the injector, the greater its impact on the non-wetted area. The obstacle height also plays a crucial role, with taller obstacles ($h3$ and $h2$) closer to the injector ($L1$) having the most pronounced effects. In contrast, the smallest obstacle ($h1$) shows minimal impact on the non-wetted area, except at the closest and farthest distances, where it contributes to higher non-wetted areas at lower flow rates.

The funnel-shaped region where no air is present appears across specific obstacle configurations, indicating that while the obstacles do influence the formation of this region, their impact is not consistently distinguishable across all cases. This suggests that the effect of obstacles on air layer stability and distribution is highly dependent on obstacle geometry, particularly height and proximity to the injector. The observed widening of the shedding region near taller obstacles indicates that these obstacles can disrupt the local flow dynamics, leading to instability in the air layer in certain areas. This instability could reduce the effectiveness of drag reduction, as the air layer becomes less uniform or fails to form completely.

While the results indicate that taller obstacles have a greater impact, they also suggest that there may be a critical obstacle height above which the air layer is significantly affected. Determining this critical height is essential for optimizing obstacle design to minimize disruption to the air layer and maintain efficient drag reduction. However, further research is needed to confirm the existence of such a critical height and to identify its precise value.

5.3. Air Layer Regime

In the air layer regime, images captured from FOV2 were utilized to assess the length of the air layer and observe a breakup close to the injector across various obstacle configurations. The analysis focused on quantifying the extent of the air layer in the presence of different obstacles and determining whether a Zone of Impact (ZOI), similar to that observed in the bubbly regime and transitional regime, was present. The methodology described in Chapter 3 was employed to accurately identify and measure the air layer. Additional analysis was conducted to explore any potential ZOI within this regime.

In Figure (5.15a), the detected edge of the air layer is shown. Due to uneven illumination across FOV2, a transition from white to black caused a data gap, as visible in Figure (5.16a). This gap results from the lighting conditions and is not indicative of any physical occurrence.

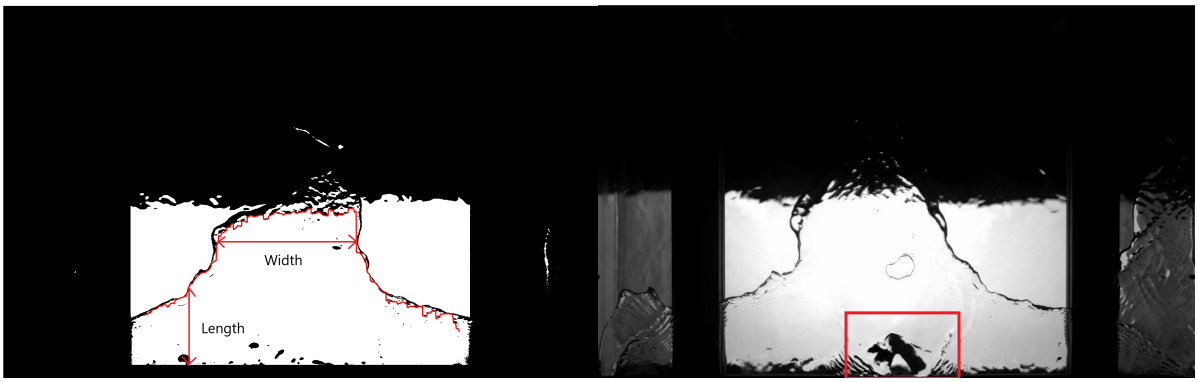

Figure 5.15: (a) Detected edge of the air layer. The sudden change from white to black is due to uneven illumination, resulting in unusable data in the affected region. Width and length have been illustrated from Figure (5.16a).**(b)** Visualisation of a breakup close to the injector.

Upon closer inspection, the detected edges do not show significant variation in length, except on the right side, where a discrepancy may be attributed to the quality of the images. The primary focus, however, is on the width of the shedding region, which is defined as the distance between the gap. To quantify the extent of the gap caused by uneven illumination, a bar plot was generated to display the distance between the detected edges, as shown in Figure (5.16b). This plot highlights the width of the gap and demonstrates how this distance varies across different experimental conditions. Although some variation is observed, there is no consistent trend linking the obstacle height and distance to the gap width.

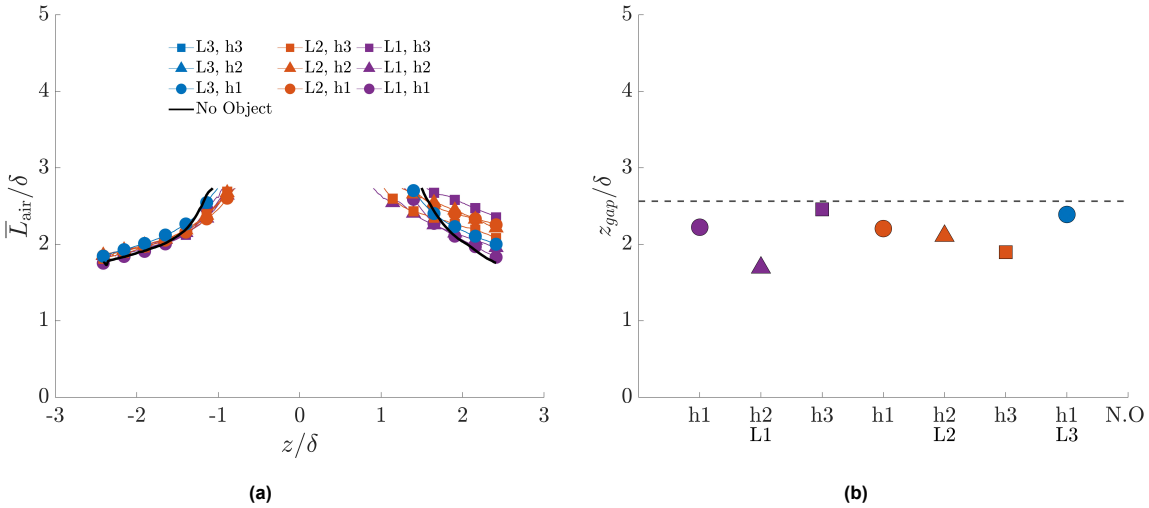

Figure 5.16: **(a)** Overlay of the detected edges. The gap visible in the overlay corresponds to the region where data was removed due to the illumination issue. and **(b)** distance of the gap between the detected edges for different obstacles.

The comparison of the measured air layer length with theoretical and experimental results from the literature is shown in Figure (5.17). The data is compared to the dispersion relation for deep water using the half-gravity wavelength from Butuzov (1966). Additionally, the experimental findings from Nikolaidou et al. (2024), Qin et al. (2019), and Zverkhovskyi (2014) are included. The plot shows how the measured air layer lengths align with these well-established models and experimental data, providing further validation for the observed phenomena.

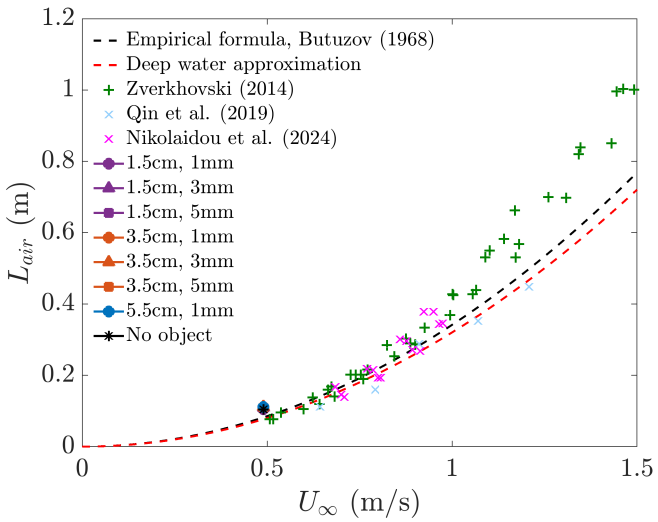

Figure 5.17: Comparison of the measured air layer length with the deep water dispersion relation (Butuzov 1966) and experimental data from Nikolaidou et al. (2024), Qin et al. (2019), and Zverkhovskyi (2014).

The consistency of the air layer formation and its susceptibility to breakups close to the injector was further investigated across different configurations, as shown in Table 5.1. The occurrence of breakups close to the injector in the air layer at various injector distances and heights under different air inlet flow rates (Q_{air}) was recorded, with red cells indicating a breakup close to the injector and green cells indicating stable air layers.

The results from the air layer regime indicate that while the presence of obstacles introduces localized instability, particularly in a small region near the injector, it does not significantly impact the overall length of the air layer. Across different configurations, the air layer remains consistent in length, even

Distance from injector	Height	Air inlet flow rate, Q_{air} (l/min)			
		3.0	20.0	25.0	30.0
No obstacle	No obstacle				
L1	h1				
	h2	6	5		
	h3	5	3	2	
L2	h1				
	h2		5		
	h3	3	3	/	
L3	h1				
	h2	/	/		
	h3	/	/		

No Breakup
Breakup

Table 5.1: breakup close to the injector occurrence of the air layer at various injector distances and heights under different air inlet flow rates (Q_{air}). Red indicates breakup, green indicates no breakup, and dashes ('/') represent cases where the breakups close to the injector were observed visually.

in the presence of obstacles.

However, the obstacles do have a notable impact on the width of the shedding region within the air layer, as illustrated by the bar plot in Figure (5.16b). This widening of the shedding region, suggests that while the overall length of the air layer is maintained, the stability of the air layer in specific regions is affected by the presence of these obstacles. The breakups close to the injector observed in these areas are likely due to the influence of the obstacles on the local flow dynamics.

The comparison of the measured air layer length with theoretical models and previous experimental data from Qin et al. (2019) and Zverkhovskyi (2014) further supports the finding that the air layer length aligns well with the deep water dispersion relation, as proposed by Butuzov (1966). This consistency indicates that, despite the localized instabilities caused by the obstacles, the overall formation and length of the air layer are in agreement with established theoretical and experimental frameworks.

5.4. Discussion

The experimental results across the bubbly, transitional, and air layer regimes provide a comprehensive view of how different upstream obstacle configurations and flow conditions impact the formation and stability of the air layer in a turbulent boundary layer (TBL). This study systematically explores the influence of obstacle height and distance from the injector, which significantly affects flow behavior, particularly in the bubbly and transitional regimes. Such systematic investigation is unique, as no other studies have explored these variables in this level of detail, particularly in the context of air lubrication and drag reduction.

In the bubbly regime, an unexpected local peak in the streamwise velocity was observed at the center of the field of view (FOV). This peak, which was anticipated to decrease due to the expected wake effects of the cylinder, instead remained prominent. The zone of influence (ZOI) for this peak spanned approximately from -0.5δ to 0.5δ, or $-3D$ to $3D$, indicating a complex interaction between the obstacle wake and the bubbly flow. This localized increase in velocity, particularly for configurations where obstacles were placed at $L1$ and $L2$ with heights $h2$ and $h3$, suggests that the obstacle wake may be enhancing local flow dynamics in a way that could influence drag reduction strategies. The findings highlight that, in certain configurations, the bubbly flow can lead to unexpected increases in velocity.

To better understand these observations, it is helpful to compare them with established knowledge of wake behavior behind cylindrical bodies within a turbulent boundary layer (TBL). Cylindrical obstacles typically generate wakes characterized by flow separation and vortex shedding, which lead to

unsteady flow conditions downstream. These wakes create localized regions of high turbulence and flow instabilities, disrupting the formation of a stable air layer. Given the challenge of finding directly comparable data for such large downstream distances, the study by Tan and Longmire (2017) offers valuable insights. They examined the recovery of vortex packet organization in turbulent boundary layers perturbed by cylindrical arrays with a height of $H = 0.2\delta$, under Reynolds number conditions of $Re_D = 3225$ and $Re_\tau = 2500$, which are closely aligned with those in this study.

As shown in Figure (5.18), the velocity field varies significantly at different wall-normal positions ($z^+ = 125$, $z^+ = 300$, and $z^+ = 500$). For this study, the camera focused on bubbles approximately 0.5–1 cm thick, corresponding to the range $180h^+ - 360h^+$. The figure highlights a region behind the cylinder where a higher-velocity zone is observed, potentially explaining the peak in streamwise velocity. This peak is surrounded by a velocity deficit, accounting for the observed minima in velocity. This higher-velocity zone occurred when the obstacle height was $H = 0.2$. However, on the right side of the figure, where $H = 1$, there is a noticeable velocity decrease behind the cylinder. Tan and Longmire (2017) attribute these high-velocity zones to tip structures, which draw faster-moving fluid downward toward the wall. Confirming this effect with particle image velocimetry (PIV) measurements would be essential to fully comprehend the implications for air lubrication and hull smoothness.

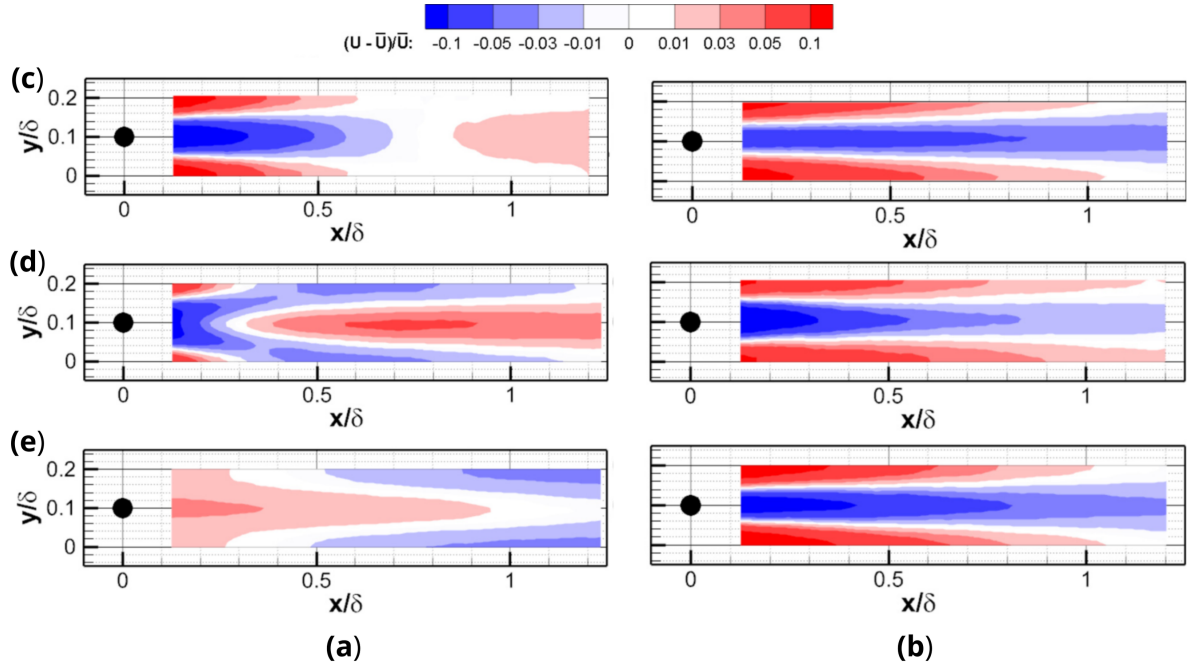

Figure 5.18: Mean streamwise velocity downstream of flow perturbed by $H = 0.2$ **(a)** and **(b)** array at **(c)** $z^+ = 125$, **(d)** $z^+ = 300$, and **(f)** $z^+ = 500$.

During the experiments, an obstacle with a height of 8 mm at a distance of 1D was also tested. It was observed that the morphology of the bubbles changed significantly. Instead of being evenly distributed, the bubbles coalesced into a large bubble that attached itself to the obstacle upstream of the injector Figure (5.19). This behavior could be attributed to the lower velocity behind the obstacle, as illustrated in Figure (5.18). Further research is necessary to investigate this phenomenon and confirm the underlying mechanisms.

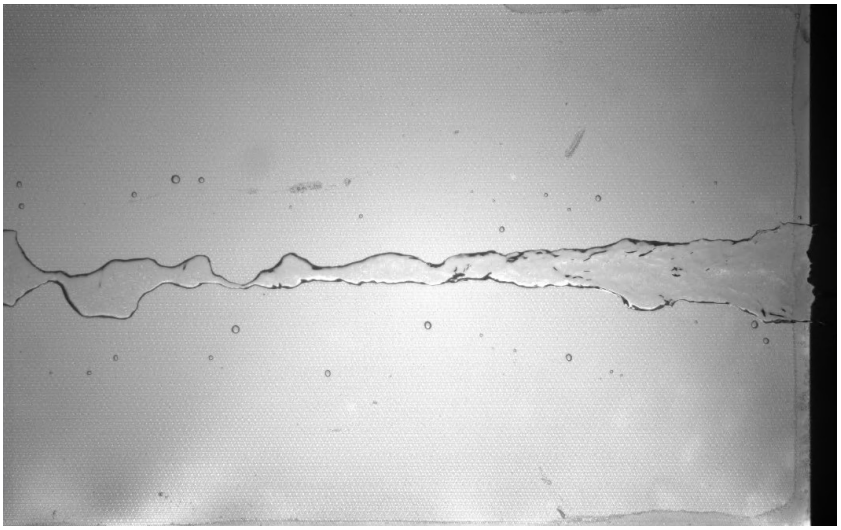

Figure 5.19: RAW image of coalesced bubble attached to upstream obstacle of 8 mm at -1D from the injector.

In the transitional regime, the most significant observation was the formation of a funnel-shaped region for specific obstacle configurations, namely $L1\ h3$ and $h2$, and $L2\ h3$. This region, where no air was present, extended from approximately -0.5δ to 0.5δ in the spanwise direction, mirroring the ZOI observed in the bubbly regime. The presence of these funnel-shaped regions across different obstacle configurations indicates a highly sensitive interaction between the wake generated by the obstacle and the air layer, which may have implications for the uniformity of air lubrication and, consequently, drag reduction. The ability to predict and control these interactions could be crucial for optimizing air lubrication systems.

For the funnel shape, vorticity fields provide additional insights. Although flow fields at this distance were not available, examining vorticity at around 25D downstream shows that the dipoles reach a width of approximately 7.5D, as shown in Figure (5.20). Given the instantaneous nature of this image, predicting the mean behavior is challenging, but the observed funnel width of around 7.5D at similar distances suggests a correlation.

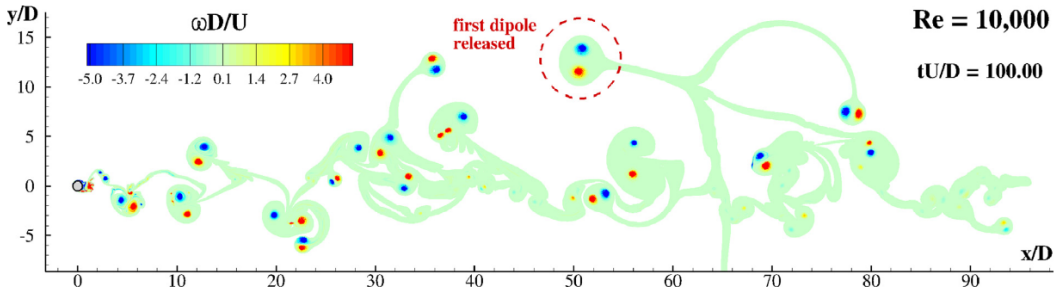

Figure 5.20: Vorticity distribution in the wake of a cylinder at $Re_D = 10000$ (Rossi, Colagrossi, and Le Touzé 2017).

The air layer regime presents a more challenging scenario for analysis due to imperfections in the data. However, it is clear that obstacles did not significantly alter the length of the air layer, though some instability was noted in specific regions. The interaction between the wake and the air layer appears to be less pronounced than in the bubbly and transitional regimes, possibly due to the more continuous nature of the air layer itself. The findings align with previous studies that indicated a strong correlation with the deep water dispersion relation for the half-gravity wavelength. Further investigation is needed to fully understand these dynamics, especially considering the potential influence of the wake on the air layer's stability and its implications for drag reduction.

In conclusion, this experimental study has provided valuable insights into the influence of upstream obstacles on air layer formation across different regimes in a TBL. The results highlight the complex interactions between the wake generated by obstacles and the air layer, particularly in the bubbly and transitional regimes. While some of these interactions are well-understood, such as the velocity peak in the bubbly regime and the funnel shape in the transitional regime, others require further exploration, especially in the context of the air layer regime. Notably, this study is one of the first to systematically investigate these factors, emphasizing the need for future research that integrates velocity measurements and explores different obstacle geometries. Such work will be crucial for refining the application of gas injection drag reduction techniques in real-world marine environments, ultimately more efficient drag reduction strategies.

6

Conclusion & Recommendations

6.1. Conclusion

This study explored the effects of upstream finite wall-mounted cylinders (FWMCs) on the formation and stability of different gas phases—bubbly, transitional, and air layer—within a turbulent boundary layer (TBL). The research aimed to better understand how the placement and dimensions of these obstacles influence the effectiveness of gas injection drag reduction techniques, which are critical for reducing hydrodynamic drag in marine applications. Through a series of controlled experiments, the study varied obstacle heights, distances from the air injector, and free-stream velocities to investigate their impact on gas phase formation and stability.

The primary research question guiding this investigation was: ***How does the placement and the dimensions of upstream circular cylindrical obstacles affect the formation and characteristics of different gas phases (bubbly, transitional, air layer) in a turbulent boundary layer?*** This question was addressed through a series of experiments that varied the height of the obstacles, their distance from the air injector, and the free-stream velocity. The findings have led to several key conclusions:

First, in the bubbly regime, it was observed that the presence of obstacles had a significant impact on the flow dynamics, particularly in the formation of local velocity peaks within the flow field. These peaks, observed in certain configurations, are hypothesized to result from the complex interactions between the obstacle-induced wake and the surrounding bubble-laden flow. The zone of influence (ZOI) for these velocity peaks was found to span approximately from -0.5δ to 0.5δ, indicating that the obstacles not only affect the local flow but also influence the overall distribution of bubbles within this region. This finding partially addresses the first subquestion, suggesting that obstacle height plays a crucial role in altering the bubbly flow characteristics.

In the transitional regime, the formation of funnel-shaped regions where air was absent provided further insights into the influence of upstream obstacles. These regions were observed to span similar ZOI ranges as in the bubbly regime, with specific obstacle configurations leading to the most pronounced funnel formations. The analysis of these regions highlighted the sensitivity of the transitional flow to obstacle placement, with the funnel's formation being directly linked to the interaction between the obstacle wake and the developing air layer. This finding supports the idea that both the height and distance of the obstacles from the injector are critical in determining the stability and extent of the air layer during the transition from a bubbly to an air layer regime.

For the air layer regime, the results were less definitive due to data imperfections. However, it was clear that while obstacles did not significantly alter the length of the air layer, they did influence its stability, particularly in regions close to the obstacles. The stability issues observed suggest that while a continuous air layer can be maintained, its integrity is susceptible to disruptions caused by upstream wakes, especially in the case of taller obstacles. This observation further answers the first and second subquestions, indicating that obstacle height and placement can affect the formation and maintenance of a stable air layer, though the effects are more subtle compared to the other regimes.

The comparative analysis with the wake of a cylindrical obstacle in a TBL revealed that the behaviors observed in the bubbly and transitional regimes align with known wake dynamics. Specifically, the ZOI and the funnel width correlated with the expected wake effects at similar Re_D, indicating that the obstacle wakes are likely driving the observed flow disruptions. This analysis highlights the importance of considering wake-induced instabilities when designing gas injection systems for drag reduction.

6.2. Recommendations for future research

Velocity measurements

Future research should integrate velocity measurements, such as Particle Image Velocimetry (PIV), to provide a more detailed understanding of the flow dynamics around obstacles. These measurements would help in quantifying the wake effects and their impact on the air layer, particularly in the transitional and air layer regimes. It is also essential to ensure accurate free-stream velocity measurements in future experiments to eliminate potential discrepancies.

Wider field of view

The current experimental setup was limited by the field of view, which did not capture the entire span of the plate. Future studies should consider widening the FOV to include the entire span, which would require a new experimental setup. This setup should include a custom-made, water-resistant LED panel designed to illuminate the entire plate uniformly. The development of such an LED panel is crucial, as the standard LED used in this study, despite being modified for water resistance, occasionally experienced leaks. A carefully designed and built LED panel would significantly enhance the accuracy and reliability of the experimental data.

More obstacles

Exploring the effects of larger obstacles on the air layer formation and stability is another avenue for future research. During the current study, preliminary tests with obstacles of 8 mm height in a bubbly regime with a free-stream velocity of 0.94 m/s showed significant changes in bubble morphology, including the formation of a large bubble attached to the obstacle, which grew with increased air flow. Investigating such phenomena further could provide valuable insights into the scaling effects and the limits of gas injection drag reduction techniques.

However, it is equally important to explore the effects of smaller obstacles to determine if there is a critical height where the effects become noticeable. Additionally, testing obstacles with different aspect ratios could reveal how the ratio between height and diameter influences the stability and effectiveness of the air layer regimes. Understanding these factors could help identify the optimal obstacle dimensions for maximizing the benefits of gas injection drag reduction across a range of flow conditions.

Improved experimental setup

The experimental setup could be further optimized to ensure accurate free-stream velocity measurements and to minimize the influence of support structures on the flow. The beams of the current support structure, located in the middle of the setup, affected the field of view and introduced unwanted flow disturbances. A redesign of the experimental setup, with a focus on minimizing such disturbances, would enhance the validity of the results..

Overall, this study has contributed to a deeper understanding of the interactions between upstream obstacles and gas injection drag reduction techniques in a turbulent boundary layer. The findings highlight the complexity of these interactions and provide a foundation for future research aimed at optimizing drag reduction strategies for marine vessels and other engineering applications.

References

Adrian, Ronald J. 2007. “Hairpin vortex organization in wall turbulence.” *Physics of Fluids.*

Ahmadzadehtalatapeh, M., and M. Mousavi. 2015. “A Review on the Drag reduction Methods of the Ship Hulls for Improving the Hydrodynamic Performance.” *International Journal of Maritime Technology.*

Allen, J. R. L. 1985. *Principles of Physical Sedimentology.* Springer.

Anand, Abirath. 2021. “A free-slip ”speed-modulator.”

ANSYS. n.d. “Turbulence modelling training manual.” Accessed May 30, 2024. https://www.ansys.com/training-center/course-catalog/fluids/ansys-cfd-fluent-and-cfx-turbulence-modeling.

Blevins, R.D. 1990. *Flow-induced vibration.* 2nd. Van Nostrand Reinhold.

Boris Jacob, Angelo Olivieri, Massimo Miozzi, Emilio F. Campana, and Renzo Piva. 2010. “Drag reduction by microbubbles in a turbulent boundary layer.” *Physics of Fluids.*

Braslow, Albert L., and Eugene C. Knox. 1957. *Simplified method for determination of critical height of distributed roughness particles for boundary-layer transition at Mach numbers from 0 to 5.* Technical Note 4363. National Advisory Committee for Aeronautics.

Butuzov, A. A. 1966. “Limiting parameters of an artificial cavity formed on the lower surface of a horizontal wall.” *Fluid Dynamics.*

Ceccio, S.L., M. Perlin, and B. Elbing. 2012. “Air lubrication drag reduction on great lake ships.” *Great Lakes Maritime Research Institute.*

Corporation, SMC. n.d. “Digital Flow Switch.”

Domel, August G., Mehdi Saadat, James C. Weaver, Hossein Haj-Hariri, Katia Bertoldi, and George V. Lauder. 2018. “Shark skin-inspired designs that improve aerodynamic performance.” *The Royal Society Publishing.*

Elbing, Brian R., Simo A. Mäkiharju, Andrew Wiggins, Steven L. Ceccio, David D. Dowling, and Marc Perlin. 2013. “On the scaling of air layer drag reduction.” *Journal of Fluid Mechanics.*

Elbing, Brian R., Eric S. Winkel, Keary A. Lay, Steven L. Ceccio, David D. Dowling, and Marc Perlin. 2008. “Bubble-induced skin-friction drag reduction and the abrupt transition to air-layer drag reduction.” *Journal of Fluid Mechanics.*

Essel, Ebenezer E., Mark F. Tachie, and Ram Balachandar. 2021. “Time-resolved wake dynamics of finite wall-mounted circular cylinders submerged in a turbulent boundary layer.” *J. Fluid Mech.*

Ferrante, A., and S. Elghobashi. 2004. “On the physical mechanism of drag reduction in a spatially developing turbulent boundary layer laden with microbubbles.” *Journal of Fluid engineering.*

Ganapathisubramani, B., E.K Longmire, and I. Marusic. 2003. “Characteristics of vortex packets in turbulent boundary layers.” *Journal of Fluid Mechanics.*

Guin, M.M., H. Kato, H. Yamamoto, M. Maeda, and M. Miyanaga. 1996. “Reduction of skin friction by microbubbles and its relation with near wall bubble concentration in a channel.” *J Mar Sci Technol.*

Harleman, M.J.W., R. Delfos, T.J.C. van Terwisga, and J. Westerweel. 2011. “Dispersion of bubbles in fully developed channel flow.” *Journal of Physics: Conference, vol. 318, p.052007.*

Hutchins, N., and Ivan Marusic. 2006a. “Evidence of very long meandering features in the logarithmic region of turbulent boundary layers.” *Journal of Fluid Mechanics.*

Hutchins, N., and Ivan Marusic. 2006b. “Experimental study of wall turbulence: Implications for control.” *Transition and Turbulence Control.*

J.C. Del Álamo and J. Jiménez. 2003. “Spectra of the very large anisotropic scales in turbulent channels.” *Phys. Fluids.*

Jinghzen, Ren, and Liang Hanwei. 2017. “Measuring the sustainability of marine fuels: A fuzzy group multi-criteria decision making approach.” *Transp Res D.*

Kim, D., and P. Moin. 2010. “Direct numerical study of air layer drag reduction phenomenon over a backward-facing step.” *Center for Turbulence Research Annual Research Briefs.*

Kim, John. 2003. “Control of turbulent boundary layers.” *Physics of Fluids.*

Kim, Young-Roung, and Sverre Steen. 2023. “Potential energy savings of air lubrication technology on merchant ships.” *International Journal of Naval Architecture and Ocean Engineering.*

Kitagawa, A., K. Hishida, and Y Kodama. 2005. “Flow structure of microbubble-laden turbulent channel flow measured by PIV combined with the shadow image technique.” *Exp Fluids.*

Kline, S. J., W.C. Reynolds, F. A. Schraub, and P. W. Runstadler. 1967. “The structure of turbulent boundary layers.” *Journal of Fluid Mechanics.*

Larsson, Lars, Hoyte C. Raven, and J. Randolph Paulling. 2010. *Ship Resistance and Flow.* Society of Naval Architects / Marine Engineers.

Legner, H. H. 1984. “Simple model for gas bubble drag reduction.” *Phys Fluids.*

Lu, J., A. Fernandez, and G. Tryggvason. 2005. “The effect of bubbles on the wall drag in a turbulent channel flow.” *Phys Fluids.*

Madavan, N. K., S. Deutsch, and C. L. Merkle. 1984. “Reduction of the turbulent skin friction by microbubbles.” *Physics of Fluids.*

———. 1985. “Measurements of local skin friction in microbubble-modified turbulent boundary layer.” *Journal of Fluid Mechanics.*

Mäkiharju, Simo A., Marc Perlin, and Steven L. Ceccio. 2012. “On the Energy Economics of Air Layer Lubrication Drag Reduction.” *International Journal of Naval Architecture and Ocean Engineering.*

Marie, J.L. 1987. “A simple analytical formulation for microbubble drag reduction.” *J PhysicoChem Hydrodyn.*

McCormick, Micheal E., and Rameswar Battacharyya. 1973. “Potential energy savings of air lubrication technology on merchant ships.” *Naval Engineers Journal.*

Merkle, C. L., and S. Deutsch. 1990. “Drag reduction in liquid boundary layers by gas injection.” *Prog Astronaut Aeronaut.*

———. 1992. “Microbubble drag reduction in liquid turbulent boundary layers.” *ASME Appl Mech Rev.*

Murai, Yuichi. 2014. “Frictional drag reduction by bubble injection.” *Experiments in Fluids.*

Murai, Yuichi, H. Fujii, Y. Tasaka, and Y. Takeda. 2006. “Turbulent bubbly channel flow investigated by ultrasound velocity profiler.” *J Fluid Sci Technology.*

Murai, Yuichi, Y. Oishi, Y. Takeda, and F. Yamamoto. 2006. “Turbulent shear stress profiles in a bubbly channel flow assessed by particle tracking velocimetry.” *Exp Fluids.*

Nieuwstadt, Frans T.M., Bendiks J. Boersma, and Jerry Westerweel. 2016. *Turbulence: Introduction to Theory and Applications of Turbulent Flows.* Springer.

Nikolaidou, L., A. Laskari, C. Poelma, and T. van Terwisga. 2024. “Effect of incoming flow conditions on air lubrication regimes.” *International Journal of Multiphase Flow.*

rs-online. 2024. “Festo G 1/4 Pneumatic Regulator - 0.1MPa to 1MPa, 1/4 in, 10bar max. input, 8099359.” Accessed May 25, 2024. https://benl.rs-online.com/web/p/pneumatic-regulators/2539227?gb=s.

Pang, M. J., J. J. Wei, and B. Yu. 2013. “Numerical study on modulation of microbubbles on turbulence frictional drag in horizontal channel.” *Ocean Engineering.*

Phillips, W.R.C. 2003. *Wind over Waves II: Forecasting and Fundamentals.* Horwood.

Porteous, Ric, Danielle J. Moreau, and Con J. Doolan. 2014. “A review of flow-induced noise from finite wall-mounted cylinders.” *Journal of Fluids and Structures* 51:240–254. ISSN: 0889-9746. https://doi.org/https://doi.org/10.1016/j.jfluidstructs.2014.08.012. https://www.sciencedirect.com/science/article/pii/S0889974614001959.

Preston, J. H. 1957. “The minimum Reynolds number for a turbulent boundary layer and the selection of a transition device.” *Department of Fluid Mechanics, University of Liverpool.*

Psaraftis, Harilaos N., and Christos A. Kontovas. 2020. “Decarbonization of Maritime Transport: Is There Light at the End of the Tunnel?” *Sustainability* 13.

Qin, Shijie, Yue Wu, Dazhuan Wu, and Jiarong Hong. 2019. “Experimental investigation of ventilated partial cavitation.” *International Journal of Multiphase Flow* 113:153–164.

Rossi, Emanuele, Andrea Colagrossi, and David Le Touzé. 2017. “he DVH model: Simulating 2D viscous flows around five different bodies at Re = 10,000.” *VII International Conference on Computational Methods in Marine Engineering (MARINE 2017).*

Sanders, Wendy C., Eric S. Winkel, Steven L. Ceccio, David D. Dowling, and Marc Perlin. 2006. “Bubble friction drag reduction in a high-Reynolds-number flat-plate turbulent boundary layer.” *Journal of Fluid Mechanics.*

Schoppa, W., and F. Hussain. 2002. “Coherent structure generation in near-wall turbulence.” *Journal of Fluid Mechanics.*

Serizawa, A., and I. Kataoka. 1990. “Turbulence suppression in bubbly two-phase flow.” *Nuclear Engineering Design.*

Stenzel, Volkmar, Yvonne Wilke, and Wolfram Hage. 2010. “Drag-reducing paints for the reduction of fuel consumption in aviation and shipping.” *Elsevier.*

Sumner, D., J. L. Heseltine, and O. J. P. Dansereau. 2004. “Wake structure of a finite circular cylinder of small aspect ratio.” *Experiments in Fluids* 37 (5): 720–730. https://doi.org/10.1007/s00348-004-0862-7.

Tan, Yan Ming, and Ellen K. Longmire. 2017. “Recovery of vortex packet organization in perturbed turbulent boundary layers.” *Physical review Fluids.*

Theodorsen, T. 1952. “Mechanism of Turbulence.” *Proceedings of the 2nd Midwestern Conference on Fluid Mechanics.*

tudelft.nl. 2004. “Water tunnel for Optical Diagnostics Applications (WODA).” Accessed May 25, 2024. https://www.tudelft.nl/me/over/afdelingen/process-energy/about-pe/facilities/water-tunnel-for-optical-diagnostics-applications-woda.

White, Frank M. 2011. *Fluid Mechanics.* McGraw-Hill.

Xu, J., M.L. Maxey, and G.E. Karniadakis. 2002. “Numerical simulation of turbulent drag reduction using micro-bubbles.” *Ocean Engineering.*

Yifeng, F., C. Yuan, and X. Q. Bai. 2017. “Marine Drag Reduction of Shark Skin Inspired Riblet Surfaces.”

Zdravkovich, M.M. 1997. “Flow around Circular Cylinders; Volume 1. Fundamentals.” *Journal of Fluid Mechanics* 350.

Zhao, L.H., H.I. Andersson, and J.J.J Gillissen. 2010. “Turbulence modulation and drag reduction by spherical particles.” *Phys Fluids.*

Zhao, L.H., H.I. Andersson, and C. Marchioli. 2012. “Stokes number effects on particle slip velocity in wall-bounded turbulence and implications for dispersion models.” *Phys Fluids.*

Zverkhovskyi, Oleksandr. 2014. “Ship drag reduction by air cavities.”

A

Code

A.1. Bubbly regime

Listing A.1: MATLAB code for processing the bubbly regime.

```
%% Clear workspace, command window, and close all figures
clc;
clear;
close all;

%% Define directories
baseDirs = {
    'C:\Users\thiba\Documents\Thesis\Data\54Hz\no_object',
    'C:\Users\thiba\Documents\Thesis\Data\54Hz\1.5cm\1mm',
    'C:\Users\thiba\Documents\Thesis\Data\54Hz\1.5cm\3mm',
    'C:\Users\thiba\Documents\Thesis\Data\54Hz\1.5cm\5mm',
    'C:\Users\thiba\Documents\Thesis\Data\54Hz\3.5cm\1mm',
    'C:\Users\thiba\Documents\Thesis\Data\54Hz\3.5cm\3mm',
    'C:\Users\thiba\Documents\Thesis\Data\54Hz\3.5cm\5mm',
    'C:\Users\thiba\Documents\Thesis\Data\54Hz\5.5cm\1mm',
    'C:\Users\thiba\Documents\Thesis\Data\54Hz\5.5cm\3mm',
    'C:\Users\thiba\Documents\Thesis\Data\54Hz\5.5cm\5mm'
};

fileNames = {
    'LED_all_no_object.mat',
    'LED_all_1.5cm_1mm.mat',
    'LED_all_1.5cm_3mm.mat',
    'LED_all_1.5cm_5mm.mat',
    'LED_all_3.5cm_1mm.mat',
    'LED_all_3.5cm_3mm.mat',
    'LED_all_3.5cm_5mm.mat',
    'LED_all_5.5cm_1mm.mat',
    'LED_all_5.5cm_3mm.mat',
    'LED_all_5.5cm_5mm.mat'
};

%% Define parameters
minDotSize1 = 40;
minDotSize2 = 150;
seClosing = strel('disk', 3);
borderWidth = 10;
frameRate = 500;
pixelToM = 0.14286 * 10^-3;
flowVelocity = 0.94;
folder = 'Data_segmented';

%% Process each directory and file name pair
for k = 1:length(baseDirs)
    baseDir = baseDirs{k};
    fileName = fileNames{k};
```

```
    fullPath = fullfile(baseDir, fileName);

    %% Add directory to MATLAB path
    addpath(baseDir);

    %% Load the MAT file containing the binary images
    if exist(fullPath, 'file')
        data = load(fullPath);
        dataFields = fieldnames(data);
        LED_all = data.(dataFields{1});  % dynamically load the first variable
        disp(['File loaded successfully: ', fullPath]);
    else
        disp(['File does not exist: ', fullPath]);
        continue;  % Skip this iteration if the file does not exist
    end

    numImages = numel(LED_all);

    %% Setup directories for saving results
    folderName = fullfile(baseDir, folder);
    if ~exist(folderName, 'dir')
        mkdir(folderName);
    end

    figuresFolder = fullfile(folderName, 'folder_figures');
    if ~exist(figuresFolder, 'dir')
        mkdir(figuresFolder);
    end

    %% Process each image pair
    for i = 1:2:numImages-1
        firstImage = preprocessImage(LED_all(i).I, minDotSize1, minDotSize2, seClosing,
            borderWidth);
        secondImage = preprocessImage(LED_all(i+1).I, minDotSize1, minDotSize2, seClosing,
            borderWidth);
        [connectedImage, numNotConnected, velocities, statsCurr] = connectBubbles(secondImage
            , firstImage, pixelToM, frameRate, i, figuresFolder);
        velocities(abs(velocities(:,1)) > flowVelocity | abs(velocities(:,2)) > flowVelocity,
             :) = NaN;
        [bubbleAreas, bubbleDiameters] = calculateBubbleAreas(connectedImage);

        % Call to segment the image data (pass both height and width)
        segmentData = segmentImage(connectedImage, velocities, bubbleAreas, bubbleDiameters,
            statsCurr, size(secondImage, 1), size(secondImage, 2));

        % Store the data for each pair
        savePath = fullfile(folderName, sprintf('connected_image_pair_%05d_%05d.mat', i, i+1)
            );
        connectedImageStruct = struct('SegmentData', segmentData);
        save(savePath, 'connectedImageStruct');
    end

    %% Combine all individual MAT-files into a single MAT-file
    outputFileSuffix = regexprep(fileName, '^LED_all', '');
    combineMATfiles(folderName, fullfile(folderName, ['combined_results_x_z' outputFileSuffix
        ]));

    %% After processing, clear large variables
    clear data LED_all;  % Free up memory by removing large variables
end

disp('All datasets processed.');

%% Helper functions
function cleanedImage = preprocessImage(imageData, minDotSize1, minDotSize2, seClosing,
    borderWidth)
    invertedImage = ~imbinarize(imageData);
    openedImage = bwareaopen(invertedImage, minDotSize1);
    closedImage = imclose(openedImage, seClosing);
    filledImage = imfill(closedImage, 'holes');
    [cleanedImage, numRemovedBubbles] = removeBorderBubbles(filledImage, borderWidth);
```

```
end

function [filledImage, numRemovedBubbles] = removeBorderBubbles(filledImage, borderWidth)
    borderTouched = padarray(true(size(filledImage) - 2 * borderWidth), [borderWidth
        borderWidth], false, 'both');
    components = bwlabel(filledImage);
    borderComponents = unique(components(~borderTouched));
    filledImage(ismember(components, borderComponents)) = 0;
    numRemovedBubbles = numel(borderComponents);
end

function [connectedImage, numNotConnected, velocities, statsCurr] = connectBubbles(currFrame,
     prevFrame, pixelToM, frameRate, pairIndex, figuresFolder)
    [prevLabeled, numLabelsPrev] = bwlabel(prevFrame);
    [currLabeled, numLabelsCurr] = bwlabel(currFrame);
    connectedImage = zeros(size(currFrame));
    numNotConnected = 0;
    velocities = zeros(numLabelsCurr, 2);

    statsPrev = regionprops(prevLabeled, 'Centroid');
    statsCurr = regionprops(currLabeled, 'Centroid');

    for i = 1:numLabelsCurr
        minDistance = inf;
        bestMatchIdx = -1;
        for j = 1:numLabelsPrev
            distance = norm(statsCurr(i).Centroid - statsPrev(j).Centroid);
            if distance < minDistance
                minDistance = distance;
                bestMatchIdx = j;
            end
        end
        if bestMatchIdx ~= -1
            connectedImage(currLabeled == i) = 1;
            deltaX = (statsCurr(i).Centroid(1) - statsPrev(bestMatchIdx).Centroid(1)) *
                pixelToM * frameRate;
            deltaZ = (statsCurr(i).Centroid(2) - statsPrev(bestMatchIdx).Centroid(2)) *
                pixelToM * frameRate;
            velocities(i, :) = [deltaX, deltaZ];
        else
            numNotConnected = numNotConnected + 1;
            velocities(i, :) = [NaN, NaN];  % Assign NaN to non-matched bubbles
        end
    end
end

function [bubbleAreas, bubbleDiameters] = calculateBubbleAreas(connectedImage)
    [labeledImage, numLabels] = bwlabel(connectedImage);
    bubbleAreas = zeros(numLabels, 1);
    bubbleDiameters = zeros(numLabels, 1);  % Store diameters here

    for label = 1:numLabels
        areaInPixels = sum(labeledImage(:) == label);
        bubbleAreas(label) = areaInPixels;
        bubbleDiameters(label) = sqrt(4 * areaInPixels / pi);  % Calculate equivalent
            diameter in pixels
    end
end

function segmentData = segmentImage(connectedImage, velocities, bubbleAreas, bubbleDiameters,
     statsCurr, imageHeight, imageWidth)
    numZSegments = 25;
    numXSegments = 3;

    segmentHeight = imageHeight / numZSegments;
    segmentWidth = imageWidth / numXSegments;
    segmentData = cell(numZSegments, numXSegments);  % Create a cell array to store data for
        each 2D segment

    % Initialize accumulators for cumulative data
    cumulativeVelocities = [];
```

```
    cumulativeAreas = [];
    cumulativeDiameters = [];

    for zSeg = 1:numZSegments
        for xSeg = 1:numXSegments
            % Define the segment ranges in both directions
            zRange = round((zSeg-1) * segmentHeight + 1) : round(zSeg * segmentHeight);
            xRange = round((xSeg-1) * segmentWidth + 1) : round(xSeg * segmentWidth);

            % Find the bubbles that fall within this segment
            inSegment = arrayfun(@(x) ...
                x.Centroid(2) >= zRange(1) && x.Centroid(2) <= zRange(end) && ...
                x.Centroid(1) >= xRange(1) && x.Centroid(1) <= xRange(end), statsCurr);

            % Store data for this segment
            segmentVelocities = velocities(inSegment, :);
            segmentAreas = bubbleAreas(inSegment);
            segmentDiameters = bubbleDiameters(inSegment);

            segmentData{zSeg, xSeg}.Velocities = segmentVelocities;
            segmentData{zSeg, xSeg}.BubbleAreas = segmentAreas;
            segmentData{zSeg, xSeg}.BubbleDiameters = segmentDiameters;
            segmentData{zSeg, xSeg}.ZSegmentStart = zRange(1);
            segmentData{zSeg, xSeg}.ZSegmentEnd = zRange(end);
            segmentData{zSeg, xSeg}.XSegmentStart = xRange(1);
            segmentData{zSeg, xSeg}.XSegmentEnd = xRange(end);

            % Accumulate data for summary
            cumulativeVelocities = [cumulativeVelocities; segmentVelocities];
            cumulativeAreas = [cumulativeAreas; segmentAreas];
            cumulativeDiameters = [cumulativeDiameters; segmentDiameters];
        end
    end

    % Append cumulative data as the last entry
    segmentData{numZSegments+1, numXSegments+1}.Velocities = cumulativeVelocities;
    segmentData{numZSegments+1, numXSegments+1}.BubbleAreas = cumulativeAreas;
    segmentData{numZSegments+1, numXSegments+1}.BubbleDiameters = cumulativeDiameters;
    segmentData{numZSegments+1, numXSegments+1}.Description = 'Cumulative Data for All
        Segments';
end

function combineMATfiles(folder, outputFileName)
    matFiles = dir(fullfile(folder, '*.mat'));
    combinedData = [];  % Initialize as empty array to store structured data

    % Iterate through each file in the directory
    for i = 1:length(matFiles)
        filePath = fullfile(folder, matFiles(i).name);
        if contains(filePath, 'connected_image_pair')
            loadedData = load(filePath, 'connectedImageStruct');  % Load the specific
                structure
            if isempty(combinedData)
                combinedData = loadedData.connectedImageStruct;  % Initialize if empty
            else
                combinedData = [combinedData, loadedData.connectedImageStruct];  %
                    Concatenate structures
            end
        end
    end

    % Save the combined data to a new .mat file
    if ~isempty(combinedData)
        save(outputFileName, 'combinedData', '-v7.3');
    end
end
```

A.2. Transitional regime

Listing A.2: MATLAB code for processing the transitional regime.

```

% Clear the environment
clc;
clear;
close all;

%% Parameters
base_path = 'C:\Users\thiba\Documents\Thesis\Data\40Hz';
depths = {'no_object'};
thicknesses = {''};
Q_values = 6:6:12;


% Process each directory
for i = 1:length(depths)
    for j = 1:length(thicknesses)
        if strcmp(depths{i}, 'no_object') && ~isempty(thicknesses{j})
            continue;  % Skip invalid combinations
        end
        for q = Q_values
            directory = generatePath(base_path, depths{i}, thicknesses{j}, q);
            [processedStruct, combinedImage] = processAndCombine(directory, q);
            saveProcessedData(directory, depths{i}, thicknesses{j}, q, processedStruct,
                combinedImage);
        end
    end
end

disp('All directories have been processed.');

function directory = generatePath(base_path, depth, thickness, q)
    if strcmp(depth, 'no_object')
        directory = fullfile(base_path, depth, sprintf('%.1fQ', q));
    else
        directory = fullfile(base_path, depth, thickness, sprintf('%.1fQ', q));
    end
end

function [processedStruct, combinedImage] = processAndCombine(directory, q)
    file_pattern = fullfile(directory, 'LED_all*.mat');
    files = dir(file_pattern);
    numFiles = length(files);

    if numFiles == 0
        fprintf('No matching .mat files found in %s\n', directory);
        processedStruct = struct();
        combinedImage = [];
        return;
    end

    imageCount = 0;
    processedStruct = repmat(struct('FileName', '', 'ProcessedImage', [], 'Area', 0),
        numFiles * 1000, 1); % Initial allocation
    combinedSum = 0;

    for fileIdx = 1:numFiles
        file = files(fileIdx);
        filePath = fullfile(directory, file.name);
        fprintf('Processing file %d of %d: %s\n', fileIdx, numFiles, filePath);
        data = load(filePath);
        if isfield(data, 'LED_all')
            LED_images = data.LED_all;
            for imgIdx = 1:numel(LED_images)
                binaryImage = LED_images(imgIdx).I;
                processedImage = processImage(binaryImage, q);
                area = sum(processedImage(:));

                % Update processedStruct
                structIdx = imageCount + 1;
                processedStruct(structIdx).FileName = sprintf('image_%05d', structIdx);
                processedStruct(structIdx).ProcessedImage = processedImage;
```

```
                processedStruct(structIdx).Area = area;

                % Accumulate for combined image
                if imageCount == 0
                    combinedSum = double(processedImage);
                else
                    combinedSum = combinedSum + double(processedImage);
                end
                imageCount = imageCount + 1;
            end
        else
            fprintf('Expected field not found in %s\n', filePath);
        end
    end

    % Trim processedStruct to the actual number of images
    processedStruct = processedStruct(1:imageCount);

    % Create combined image
    combinedImage = combinedSum / imageCount;
end

function saveProcessedData(directory, depth, thickness, q, processedStruct, combinedImage)
    % Save processedStruct
    structFileName = sprintf('processed_data_%s_%s_%.1fQ.mat', depth, thickness, q);
    structFilePath = fullfile(directory, structFileName);
    save(structFilePath, 'processedStruct', '-v7.3');
    fprintf('Processed structure saved to: %s\n', structFilePath);

    % Save combined image
    if isempty(thickness)
        combinedFileName = sprintf('combined_image_%s_%.1fQ.mat', depth, q);
    else
        combinedFileName = sprintf('combined_image_%s_%s_%.1fQ.mat', depth, thickness, q);
    end
    combinedFilePath = fullfile(directory, combinedFileName);
    save(combinedFilePath, 'combinedImage', '-v7.3');
    fprintf('Combined image saved to: %s\n', combinedFilePath);
end

function processedImage = processImage(binaryImage, q)
    seClose = selectStructuringElements(q);
    seOpen = seClose;  % Assuming same values for simplicity
    edgeImage = edge(~binaryImage, 'Canny');
    closedImage = imclose(edgeImage, strel('disk', seClose));
    openedImage = imopen(closedImage, strel('disk', seOpen));
    filledImage = openedImage; % Start with the opened image

    if q >= 6 && q <= 12
        filledImage = imfill(filledImage, 'holes');
    end

    % Do not invert the image to keep it non-binary for averaging
    processedImage = filledImage;
end

function se = selectStructuringElements(q)
    if q <= 12
        se = 1;
    elseif q <= 36
        se = 8;
    else
        se = 23;
    end
end
```

Listing A.3: MATLAB code for detection of the ZOI edges and identification of the funnel start.

```
    % Load the .mat file containing the cell array
matFilePath = 'C:\Users\thiba\Documents\Thesis\Data\40Hz\0.7\threshold_0.7.mat'; % Adjust
    this path
```

```
loadedData = load(matFilePath);

% Assuming the cell array is named 'thresholdedImagesCell'
cellArray = loadedData.thresholdedImagesCell;

% Define the indices corresponding to the cases of interest
indicesOfInterest = [39:48, 55:64, 103:112];

% Define the naming conventions for each case by index
nameMapping = containers.Map(...
    [39, 40, 41, 42, 43, 44, 45, 46, 47, 48, ...
     55, 56, 57, 58, 59, 60, 61, 62, 63, 64, ...
     103, 104, 105, 106, 107, 108, 109, 110, 111, 112], ...
    {'-1.5D, h2_Q48.0', '-1.5D, h2_Q54.0', '-1.5D, h2_Q60.0', '-1.5D, h2_Q66.0', ...
     '-1.5D, h2_Q72.0', '-1.5D, h2_Q78.0', '-1.5D, h2_Q84.0', '-1.5D, h2_Q90.0', ...
     '-1.5D, h2_Q96.0', '-1.5D, h2_Q102.0', '-1.5D, h3_Q48.0', '-1.5D, h3_Q54.0', ...
     '-1.5D, h3_Q60.0', '-1.5D, h3_Q66.0', '-1.5D, h3_Q72.0', '-1.5D, h3_Q78.0', ...
     '-1.5D, h3_Q84.0', '-1.5D, h3_Q90.0', '-1.5D, h3_Q96.0', '-1.5D, h3_Q102.0', ...
     '-3.5D, h3_Q48.0', '-3.5D, h3_Q54.0', '-3.5D, h3_Q60.0', '-3.5D, h3_Q66.0', ...
     '-3.5D, h3_Q72.0', '-3.5D, h3_Q78.0', '-3.5D, h3_Q84.0', '-3.5D, h3_Q90.0', ...
     '-3.5D, h3_Q96.0', '-3.5D, h3_Q102.0'}); % Correct mapping

% Initialize a structure to store the edges
edgeStruct = struct('Name', {}, 'EdgeData', {});

% Process each relevant image based on index
for i = 1:length(indicesOfInterest)
    index = indicesOfInterest(i);
    name = cellArray{index, 1};  % Metadata (name, Q value, etc.)
    binaryImage = cellArray{index, 2};  % Binary image

    % Process the image to find edges
    [upperEdges, lowerEdges] = detectEdges(binaryImage);

    % Apply smoothing to the edges
    upperEdgesSmoothed = smoothdata(upperEdges, 'movmean', 50);  % Adjust the window size as
        needed
    lowerEdgesSmoothed = smoothdata(lowerEdges, 'movmean', 50);  % Adjust the window size as
        needed

    % Store the smoothed edge data in the structure
    edgeName = nameMapping(index);
    edgeData = [upperEdgesSmoothed; lowerEdgesSmoothed]; % Store both smoothed upper and
        lower edges

    edgeStruct(end+1) = struct('Name', edgeName, 'EdgeData', edgeData);
    fprintf('Processed and added edges for %s\n', edgeName);
end

% Save the edge data to a new .mat file
savePath = 'C:\Users\thiba\Documents\Thesis\Data\40Hz\Edges\edge_data.mat'; % Adjust the path
     as needed
save(savePath, 'edgeStruct', '-v7.3');
fprintf('Edge data saved to: %s\n', savePath);

% Plotting a Random Case from the Saved Edge Data with Funnel Detection

if ~isempty(edgeStruct)
    % Select a random case to plot
    randomIndex = randi(length(edgeStruct));
    randomCase = edgeStruct(randomIndex);

    % Extract the data for plotting
    edgeName = randomCase.Name;
    edgeData = randomCase.EdgeData;  % Correct field name
    upperEdges = edgeData(1, :);
    lowerEdges = edgeData(2, :);
    cols = length(upperEdges);

    % Convert columns (x-axis) from pixels to meters and normalize
    pixelToMeter = 1 / 7000; % Conversion factor
```

```
    xMeters = (1:cols) * pixelToMeter / 0.062; % Normal x-axis conversion

    % Convert row indices (y-axis) from pixels to meters, with 0 at 800 pixels
    yPixelsOffset = 800;
    upperEdgesMeters = (upperEdges - yPixelsOffset) * pixelToMeter / 0.062;
    lowerEdgesMeters = (lowerEdges - yPixelsOffset) * pixelToMeter / 0.062;

    % Detect the funnel start
    [funnelStartUpper, funnelStartLower] = detectFunnelStartDirectional(upperEdges,
        lowerEdges);

    % Create figure with specified paper size and position
paperPosition = [0 0 30 30]; % Same as in your other code
paperSize = [30 30];
figureHandle = figure('PaperUnits', 'centimeters', 'PaperPosition', paperPosition, 'PaperSize
    ', paperSize);

% Main plot with normalized axes
hold on;
plot(xMeters, upperEdgesMeters, 'r-', 'LineWidth', 2); % Plot upper edge in red
plot(xMeters, lowerEdgesMeters, 'b-', 'LineWidth', 2); % Plot lower edge in blue

% Mark the detected funnel start points
if ~isempty(funnelStartUpper)
    plot(xMeters(funnelStartUpper), upperEdgesMeters(funnelStartUpper), 'go', 'MarkerSize',
        10, 'MarkerFaceColor', 'g'); % Green circle
    text(xMeters(funnelStartUpper), upperEdgesMeters(funnelStartUpper), '␣␣Funnel␣Start␣(
        Lower)', 'VerticalAlignment', 'bottom', 'FontSize', 26);
else
    fprintf('No␣significant␣funnel␣start␣detected␣for␣the␣upper␣edge.\n');
end
if ~isempty(funnelStartLower)
    plot(xMeters(funnelStartLower), lowerEdgesMeters(funnelStartLower), 'go', 'MarkerSize',
        10, 'MarkerFaceColor', 'g'); % Green circle
    text(xMeters(funnelStartLower), lowerEdgesMeters(funnelStartLower), '␣␣Funnel␣Start␣(
        Upper)', 'VerticalAlignment', 'top', 'FontSize', 26);
end

% Main axes labels
xlabel('$x/␣\delta$', 'Interpreter', 'latex', 'FontSize', 35);
xlim([0 6]);
xticks(0:2:6);
ylabel('$z/␣\delta$', 'Interpreter', 'latex', 'FontSize', 35);
ylim([-1.5 1.5]);
yticks(-1.5:0.5:1.5);

% Set LaTeX interpreter for ticks and font size
set(gca, 'TickLabelInterpreter', 'latex', 'FontSize', 26);

% Adjust the axes to fill more of the figure area
ax1 = gca;
ax1.Position = [0.1, 0.10, 0.82, 0.8]; % Left, Bottom, Width, Height

% Create secondary axes with pixel-based scaling
ax2 = axes('Position', ax1.Position, 'XAxisLocation', 'top', 'YAxisLocation', 'right', ...
           'Color', 'none', 'XColor', 'k', 'YColor', 'k');

% Define the limits and ticks for the pixel-based axes
xlim(ax2, [0 38.4]);
ylim(ax2, [-9.6 9.6]);
xticks(ax2, 0:5:35);
yticks(ax2, -9:3:9);

% Labels for the pixel-based axes
xlabel(ax2, '$x/␣D$', 'Interpreter', 'latex', 'FontSize', 35);
ylabel(ax2, '$z/␣D$', 'Interpreter', 'latex', 'FontSize', 35);

% Set LaTeX interpreter for ticks and font size on the secondary axes
set(ax2, 'TickLabelInterpreter', 'latex', 'FontSize', 26);

% Legend (added to the main axes)
```

```
legend(ax1, {'Lower Edge', 'Upper Edge', 'Funnel Start'}, 'Interpreter', 'latex', 'FontSize', 26, 'Location','southwest');
hold off;

    fprintf('Plot created for random case: %s\n', edgeName);

    % Save the figure as both .fig and high-resolution .jpg
    savePath = 'C:\Users\thiba\Documents\Thesis\Data\40Hz\Edges\final'; % Adjust this path as needed
    if ~exist(savePath, 'dir')
        mkdir(savePath);
    end

    figFileName = fullfile(savePath, 'edge_plot.fig');
    jpgFileName = fullfile(savePath, 'edge_plot.jpg');

    savefig(figureHandle, figFileName);
    print(figureHandle, jpgFileName, '-djpeg', '-r300'); % Save as high-resolution JPEG

    fprintf('Figure saved as .fig and high-resolution .jpg in %s\n', savePath);

else
    fprintf('No edge data available for plotting.\n');
end

%% Functions

function [upperEdges, lowerEdges] = detectEdges(binaryImage)
    % Detect the upper and lower edges in the binary image
    [rows, cols] = size(binaryImage);
    middleRow = round(rows / 2);

    % Initialize arrays to store the edges
    upperEdges = nan(1, cols);
    lowerEdges = nan(1, cols);

    % Define the start and end columns
    startCol = 100;
    endCol = cols - 50;

    % Process each column from startCol to endCol
    for col = startCol:endCol
        % Upper edge (moving upwards from the middle row)
        for row = middleRow:-1:1
            if binaryImage(row, col) == 1 % Detecting the yellow region (binary value 1)
                upperEdges(col) = row;
                break;
            end
        end

        % Lower edge (moving downwards from the middle row)
        for row = middleRow:rows
            if binaryImage(row, col) == 1 % Detecting the yellow region (binary value 1)
                lowerEdges(col) = row;
                break;
            end
        end
    end
end

function [funnelStartUpper, funnelStartLower] = detectFunnelStartDirectional(upperEdges, lowerEdges)
    % Detect the funnel start points based on directional trends
    windowSize = 10; % Number of columns to consider for trend
    threshold = 2.4; % Minimum cumulative deviation to be considered as funnel start

    % Detect downward trend for the upper edge
    funnelStartUpper = [];
    for i = windowSize:length(upperEdges)-windowSize
        trend = mean(upperEdges(i-windowSize+1:i)) - mean(upperEdges(i+1:i+windowSize));
        if trend > threshold
```

```
            funnelStartUpper = i;
            break;
        end
    end

    % Detect upward trend for the lower edge
    funnelStartLower = [];
    for i = windowSize:length(lowerEdges)-windowSize
        trend = mean(lowerEdges(i+1:i+windowSize)) - mean(lowerEdges(i-windowSize+1:i));
        if trend > threshold
            funnelStartLower = i;
            break;
        end
    end

    % Print out debugging information
    if ~isempty(funnelStartUpper)
        fprintf('Funnel start detected at column %d for the upper edge.\n', funnelStartUpper)
            ;
    end
    if ~isempty(funnelStartLower)
        fprintf('Funnel start detected at column %d for the lower edge.\n', funnelStartLower)
            ;
    end
end
```

A.3. Air layer regime

Listing A.4: MATLAB code for processing the air layer regime.

```
    % Clear the environment
clc;
clear;
close all;

% PARAMETERS
base_path = 'D:\MSc_Thibaut\30Hz';
depths = {'no_object', '1.5cm', '3.5cm', '5.5cm'};
thicknesses = {'', '1mm', '3mm', '5mm'};
Q_values = [3.0, 6.0, 20.0, 25.0, 30.0];
D = 0.01;  % Object diameter in meters
X_scale = 0.2127659574468; % X_scale = pix/mm (7 pix = 1 mm)

% Define the range of x positions to consider
x_start = 600;
x_end = 1960;
cols_range = x_start:x_end;

% Convert pixel distances to meters and normalize by D
cols_range_m = (cols_range - mean([x_start, x_end])) * X_scale / 1000 / D;

% Define markers and colors
markerMap = containers.Map({'1mm', '3mm', '5mm', 'no_object'}, {'o', '^', 's', 'none'});
colorMap = containers.Map({'1.5cm', '3.5cm', '5.5cm', 'no_object'}, {
    [0.4940, 0.1840, 0.5560],  % Purple for 1.5cm
    [0.8500, 0.3250, 0.0980],  % Orange for 3.5cm
    [0, 0.4470, 0.7410],       % Blue for 5.5cm
    [0, 0, 0]                  % Black for no object
});

% Add 5 cm (0.05 meters) to each average distance and normalize by D
additional_distance = 0.05 / D;

% Initialize a structure to store average distances for each Q value
avgDistances = containers.Map;

% Processing loop for each Q value
for q = Q_values
    figure;
    hold on;
```

```
    legendLabels = {};
    legendHandles = [];

    for i = 1:length(depths)
        for j = 1:length(thicknesses)
            if strcmp(depths{i}, 'no_object') && ~isempty(thicknesses{j})
                continue;  % Skip invalid combinations
            end

            % Generate the file paths
            if strcmp(depths{i}, 'no_object')
                Directory = fullfile(base_path, depths{i}, sprintf('%.1fQ', q), 'Bin_Level
                    =1900');
            else
                Directory = fullfile(base_path, depths{i}, thicknesses{j}, sprintf('%.1fQ', q
                    ), 'Bin_Level=1900');
            end

            % Print the current directory being processed
            fprintf('Processing␣directory:␣%s\n', Directory);

            % Ensure the directory exists
            if ~exist(Directory, 'dir')
                fprintf('Directory␣does␣not␣exist:␣%s\n', Directory);
                continue;
            end

            % Define output folder
            outputFolder = fullfile(Directory, 'ProcessedData');

            % Load the gap_distances_x_time.mat file
            gapDistancesFilePath = fullfile(outputFolder, 'gap_distances_x_time.mat');
            if ~exist(gapDistancesFilePath, 'file')
                fprintf('gap_distances_x_time.mat␣does␣not␣exist␣in␣%s\n', Directory);
                continue;
            end

            % Load the average distances
            data = load(gapDistancesFilePath);
            average_distances = data.gap_distances_x_time.average_distances;

            % Convert y distances from pixels to meters and normalize by D
            average_distances_m = (average_distances * X_scale / 1000) / D;

            % Add the additional distance
            average_distances_m = average_distances_m + additional_distance;

            % Determine the marker and color for the current combination
            objectHeight = thicknesses{j};
            if isempty(objectHeight)
                objectHeight = 'no_object';
            end
            distanceFromInjector = depths{i};
            if isKey(markerMap, objectHeight) && isKey(colorMap, distanceFromInjector)
                marker = markerMap(objectHeight);
                color = colorMap(distanceFromInjector);

                % Set line width and style based on the case
                if strcmp(objectHeight, 'no_object')
                    lineWidth = 1.0;
                    lineStyle = '-';  % Solid line for no object case
                    legendLabel = 'no␣object'; % Special label for no object case
                else
                    lineWidth = 0.5;
                    lineStyle = '--';  % Dashed line for other cases
                    legendLabel = sprintf('L␣=␣%s,␣h␣=␣%s', distanceFromInjector,
                        objectHeight);
                end

                % Plot the data
                plotHandle = plot(cols_range_m, average_distances_m, 'Color', color, '
```

```
                    LineWidth', lineWidth, 'LineStyle', lineStyle);

                % Add markers at every 100 pixels
                markerIndices = x_start:100:x_end;
                markerIndices_m = (markerIndices - mean([x_start, x_end])) * X_scale / 1000 / D;
                markerHandle = plot(markerIndices_m, average_distances_m(markerIndices - x_start + 1), 'LineStyle', 'none', 'Marker', marker, 'Color', color, 'MarkerSize', 6);

                % Store handles and labels
                legendHandles = [legendHandles, plotHandle, markerHandle];
                legendLabels{end + 1} = legendLabel;
            end
        end
    end

    % Customize the legend to show both lines and markers
    legendEntries = arrayfun(@(h, l) plot(NaN, NaN, 'Color', get(h, 'Color'), 'Marker', get(l, 'Marker'), 'LineStyle', get(h, 'LineStyle')), legendHandles(1:2:end), legendHandles(2:2:end), 'UniformOutput', false);
    lgd = legend([legendEntries{:}], legendLabels, 'Location', 'southoutside', 'Orientation', 'horizontal', 'Interpreter', 'latex', 'FontSize', 13);
    lgd.NumColumns = 3;  % Set the number of columns to 3

    xlabel('X/D', 'Interpreter', 'latex', 'FontSize', 20);
    ylabel('$\overline{L}_{\mathrm{air}}/D$', 'Interpreter', 'latex', 'FontSize', 20);
    title(sprintf('Q = %.1f (l/min)', q), 'Interpreter', 'latex', 'FontSize', 20);

    % Set x and y axis limits and ticks
    xlim([-20 20]);
    ylim([5 25]);
    set(gca, 'XTick', -20:5:20);
    set(gca, 'YTick', 5:5:25);
    set(gca, 'TickDir', 'both');
    set(gca, 'FontSize', 13);

    hold off;

    % Save the plot as a .fig file
    savefig(fullfile(base_path, sprintf('Average_Distance_Q_%.1f.fig', q)));

    % Print completion message
    fprintf('Completed processing for Q = %.1f\n', q);
end

disp('All Q values have been processed.');
```

B

Tables

Configuration	Z1	Z2	Z3	Z4	Z5	Z6	Z7	Z8	Z9	Z10	Z11	Z12	Z13	Z14	Z15	Z16	Z17	Z18	Z19	Z20	Z21	Z22	Z23	Z24	Z25
-1.5D, h1, x1	1.69	2.17	1.71	7.39	0.58	1.57	3.29	0.93	-2.36	-5.45	-13.31	-19.65	-20.80	-13.49	-4.06	1.79	0.01	0.41	1.44	-0.61	-2.17	-1.17	-3.31	-1.13	-0.25
-1.5D, h2, x1	-2.42	-1.50	-1.53	3.35	-0.42	-1.33	-1.35	-3.59	-6.32	-17.47	-31.95	-24.26	-19.97	-16.77	-10.63	-4.96	-2.99	-0.38	1.72	-0.76	-3.42	-2.55	-4.70	-5.14	-6.44
-1.5D, h3, x1	1.79	4.15	3.27	9.25	6.01	6.55	8.29	8.58	5.65	-2.29	-9.33	-6.91	-2.26	-7.28	-3.10	3.23	4.73	3.61	3.34	-0.09	-2.26	-2.88	-5.52	-5.32	-4.16
-3.5D, h1, x1	-3.47	-3.34	-5.35	-0.65	-6.15	-7.00	-6.28	-9.67	-11.98	-14.90	-17.93	-20.22	-22.49	-23.37	-18.95	-17.10	-18.43	-17.06	-14.44	-13.60	-16.93	-11.13	-13.27	-13.64	-11.57
-3.5D, h2, x1	0.85	-0.60	0.48	7.81	1.15	-0.47	-1.35	-3.14	-4.95	-8.38	-11.80	-15.47	-19.97	-22.54	-14.20	-9.42	-6.77	-4.93	-1.95	-4.18	-6.62	-4.98	-4.68	-5.73	-4.20
-3.5D, h3, x1	-3.04	-2.24	-4.07	0.84	-4.07	-4.54	-5.08	-8.35	-12.38	-19.49	-25.72	-22.04	-18.36	-24.60	-25.63	-21.61	-16.55	-10.13	-6.29	-7.63	-7.12	-6.98	-7.60	-9.12	-9.01
-5.5D, h1, x1	-7.30	-7.44	-9.16	-5.74	-9.91	-11.88	-13.37	-15.21	-16.69	-19.84	-18.71	-19.07	-20.11	-20.35	-19.68	-21.61	-21.68	-19.76	-17.35	-19.72	-18.04	-16.66	-15.59	-15.12	-11.98
-5.5D, h2, x1	-3.14	-4.62	-5.08	-1.40	-4.48	-8.62	-7.78	-11.16	-10.87	-11.33	-9.80	-11.61	-17.15	-15.92	-13.37	-14.91	-14.43	-13.50	-11.78	-12.00	-11.30	-9.28	-9.70	-10.06	-7.19
-5.5D, h3, x1	-6.06	-4.18	-5.42	-2.66	-6.38	-8.78	-11.29	-12.14	-11.67	-9.28	-3.22	-3.30	-6.60	-12.24	-14.07	-14.76	-16.52	-14.07	-13.12	-11.31	-11.87	-9.38	-11.19	-12.16	-8.97
-1.5D, h1, x2	3.01	3.01	3.98	6.18	3.51	2.86	0.40	1.21	-0.71	-2.58	-13.02	-22.48	-20.50	-10.55	-2.50	-0.41	1.85	0.23	2.01	-1.19	-2.21	-0.60	-0.94	-2.81	-4.79
-1.5D, h2, x2	-1.93	0.48	-1.10	3.11	-0.12	1.93	-1.06	-2.38	-6.63	-15.83	-30.58	-24.34	-18.80	-18.72	-12.70	-7.18	-0.75	-0.61	1.95	-2.24	-1.57	-1.90	-2.05	-5.18	-5.98
-1.5D, h3, x2	4.12	3.92	6.00	8.68	6.45	8.82	7.77	10.25	6.81	-1.44	-10.90	-8.85	-0.82	-2.99	-3.96	3.50	7.86	5.99	4.42	0.10	-0.54	-2.50	-4.62	-5.31	-7.08
-3.5D, h1, x2	-2.11	-3.04	-4.12	-0.17	-4.72	-2.93	-7.17	-8.07	-9.89	-12.32	-17.99	-21.40	-21.92	-21.77	-20.42	-20.29	-15.85	-14.52	-11.47	-14.72	-13.81	-12.76	-11.31	-13.75	-13.59
-3.5D, h2, x2	2.69	1.94	1.58	4.45	2.23	3.58	-2.01	-2.37	-3.40	-5.75	-12.72	-16.69	-19.66	-21.13	-14.24	-8.97	-4.70	-3.26	-1.83	-4.83	-4.74	-3.62	-4.54	-4.15	-7.27
-3.5D, h3, x2	-1.98	-2.95	-1.67	1.40	-4.61	-1.70	-5.56	-7.42	-12.68	-18.91	-24.33	-27.04	-17.32	-23.98	-25.76	-20.34	-13.05	-8.67	-3.89	-5.40	-7.72	-6.92	-7.14	-8.14	-11.19
-5.5D, h1, x2	-6.90	-6.71	-8.36	-5.95	-10.67	-9.99	-14.92	-14.85	-16.18	-17.00	-18.97	-20.77	-20.74	-19.77	-21.18	-21.51	-19.04	-18.82	-16.17	-18.99	-18.24	-16.24	-15.31	-14.14	-13.16
-5.5D, h2, x2	-2.88	-2.59	-3.60	-0.36	-4.74	-5.53	-9.56	-10.42	-11.16	-9.50	-10.42	-12.96	-14.66	-14.36	-12.83	-14.05	-14.40	-12.91	-9.86	-11.86	-12.35	-9.06	-8.02	-9.53	-9.06
-5.5D, h3, x2	-2.23	-2.97	-4.01	-3.67	-6.66	-6.87	-10.15	-11.06	-13.64	-8.28	-4.26	-2.36	-6.15	-9.94	-14.82	-15.29	-13.32	-13.11	-10.08	-12.39	-11.16	-8.12	-9.47	-10.46	-10.96
-1.5D, h1, x3	1.17	1.49	1.06	7.01	1.15	0.87	0.74	0.30	-0.49	-5.85	-12.70	-20.56	-17.12	-12.51	-4.57	1.27	1.32	0.25	-0.41	0.13	-1.87	0.27	0.65	-1.45	-4.01
-1.5D, h2, x3	-2.10	-2.96	-1.27	4.81	-1.30	-0.18	-2.80	-4.51	-7.79	-18.12	-31.98	-28.20	-17.85	-18.66	-10.67	-6.29	-2.18	-1.77	-1.92	-2.24	-1.22	-2.47	-1.40	-3.29	-3.96
-1.5D, h3, x3	3.20	2.97	2.89	10.45	5.52	7.01	7.43	8.25	6.54	-3.73	-11.56	-8.35	0.91	-5.09	-3.95	2.04	7.10	4.05	2.71	1.23	-1.53	-1.78	-3.51	-4.82	-5.67
-3.5D, h1, x3	-2.94	-2.90	-6.28	0.19	-4.35	-4.93	-7.00	-8.24	-10.79	-15.60	-18.08	-21.07	-21.32	-22.25	-20.70	-19.16	-16.81	-17.36	-13.86	-15.44	-13.33	-11.11	-11.18	-12.98	-13.58
-3.5D, h2, x3	1.07	0.40	-1.18	6.26	1.28	0.83	-2.18	-4.64	-4.10	-7.34	-12.21	-15.49	-18.72	-20.33	-14.99	-9.87	-4.13	-3.31	-3.94	-4.63	-4.24	-5.30	-3.36	-2.13	-5.32
-3.5D, h3, x3	-0.62	-3.07	-3.43	2.20	-3.92	-2.54	-5.91	-8.01	-10.51	-19.01	-25.82	-26.77	-10.09	-26.99	-26.14	-21.82	-14.57	-9.59	-6.84	-6.78	-6.86	-6.50	-6.07	-8.47	-9.73
-5.5D, h1, x3	-7.39	-7.94	-9.13	-4.37	-11.45	-13.49	-15.59	-17.48	-16.03	-18.34	-17.91	-18.88	-19.34	-20.59	-19.50	-20.93	-20.64	-21.06	-19.18	-18.89	-18.48	-15.66	-13.12	-13.63	-11.72
-5.5D, h2, x3	-4.68	-4.17	-5.04	0.89	-6.39	-7.37	-8.95	-11.52	-11.47	-11.52	-11.06	-12.70	-14.61	-15.94	-13.17	-16.22	-14.57	-14.29	-12.28	-11.57	-11.11	-9.00	-7.68	-8.53	-10.56
-5.5D, h3, x3	-2.42	-4.86	-8.04	-1.71	-7.20	-9.23	-11.38	-11.74	-13.00	-7.79	-6.03	-1.50	-3.80	-15.29	-13.94	-15.57	-16.25	-14.77	-11.91	-12.26	-11.02	-8.97	-7.33	-8.62	-10.81
No Object, x1	0.00	0.00	0.00	0.00	0.00	0.00	0.00	0.00	0.00	0.00	0.00	0.00	0.00	0.00	0.00	0.00	0.00	0.00	0.00	0.00	0.00	0.00	0.00	0.00	0.00
No Object, x2	0.00	0.00	0.00	0.00	0.00	0.00	0.00	0.00	0.00	0.00	0.00	0.00	0.00	0.00	0.00	0.00	0.00	0.00	0.00	0.00	0.00	0.00	0.00	0.00	0.00
No Object, x3	0.00	0.00	0.00	0.00	0.00	0.00	0.00	0.00	0.00	0.00	0.00	0.00	0.00	0.00	0.00	0.00	0.00	0.00	0.00	0.00	0.00	0.00	0.00	0.00	0.00
-1.5D, h1, X_tot	1.96	2.22	2.25	6.86	1.75	1.77	1.47	0.81	-1.19	-4.63	-13.01	-20.90	-19.47	-12.18	-3.71	0.88	1.06	0.30	1.01	-0.56	-2.08	-0.50	-1.20	-1.80	-3.02
-1.5D, h2, X_tot	-2.15	-1.33	-1.30	3.76	-0.61	0.14	-1.73	-3.49	-6.91	-17.14	-31.50	-25.60	-18.87	-18.05	-11.33	-6.14	-1.97	-0.92	0.59	-1.75	-2.07	-2.31	-2.72	-4.54	-5.46
-1.5D, h3, X_tot	3.03	3.68	4.05	9.46	5.99	7.46	7.83	9.03	6.34	-2.49	-10.60	-8.03	-0.72	-5.12	-3.67	2.92	6.56	4.55	3.49	0.41	-1.44	-2.39	-4.55	-5.15	-5.64
-3.5D, h1, X_tot	-2.84	-3.09	-5.25	-0.21	-5.07	-4.95	-6.82	-8.66	-10.89	-14.27	-18.00	-20.89	-21.91	-22.46	-20.02	-18.85	-17.03	-16.31	-13.26	-14.59	-14.69	-11.67	-11.92	-13.46	-12.91
-3.5D, h2, X_tot	1.54	0.58	0.29	6.17	1.55	1.31	-1.85	-3.38	-4.15	-7.16	-12.24	-15.88	-19.45	-21.33	-14.48	-9.42	-5.20	-3.83	-2.57	-4.54	-5.20	-4.63	-4.19	-4.00	-5.60
-3.5D, h3, X_tot	-1.88	-2.75	-3.06	1.48	-4.20	-2.93	-5.52	-7.93	-11.86	-19.14	-25.29	-25.28	-15.26	-25.19	-25.84	-21.26	-14.73	-9.46	-5.67	-6.60	-7.23	-6.80	-6.94	-8.58	-9.98
-5.5D, h1, X_tot	-7.20	-7.36	-8.88	-5.35	-10.68	-11.79	-14.62	-15.85	-16.30	-18.40	-18.53	-19.57	-20.06	-20.24	-20.12	-21.35	-20.45	-19.88	-17.56	-19.20	-18.25	-16.19	-14.67	-14.30	-12.29
-5.5D, h2, X_tot	-3.57	-3.79	-4.57	-0.29	-5.20	-7.17	-8.77	-11.03	-11.17	-10.79	-10.42	-12.42	-15.47	-15.41	-13.12	-15.06	-14.47	-13.57	-11.31	-11.81	-11.58	-9.12	-8.47	-9.38	-8.94
-5.5D, h3, X_tot	-3.57	-4.00	-5.82	-2.68	-6.75	-8.29	-10.94	-11.64	-12.77	-8.45	-4.50	-2.38	-5.52	-12.49	-14.28	-15.21	-15.36	-13.98	-11.70	-11.99	-11.35	-8.82	-9.33	-10.41	-10.25
No Object, X_tot	0.00	0.00	0.00	0.00	0.00	0.00	0.00	0.00	0.00	0.00	0.00	0.00	0.00	0.00	0.00	0.00	0.00	0.00	0.00	0.00	0.00	0.00	0.00	0.00	0.00

Table B.1: Summary of values for the number of bubbles for different configurations.

Configuration	Z1	Z2	Z3	Z4	Z5	Z6	Z7	Z8	Z9	Z10	Z11	Z12	Z13	Z14	Z15	Z16	Z17	Z18	Z19	Z20	Z21	Z22	Z23	Z24	Z25
-1.5D, h1, x1	-2.98	-1.60	-0.02	-0.52	-1.25	-1.05	0.99	-2.37	-0.24	-0.93	-18.89	-38.46	-33.61	-17.71	-1.63	2.27	-0.29	-2.72	-1.85	-2.54	1.63	-6.71	-5.43	0.99	-1.87
-1.5D, h2, x1	-1.13	-5.42	-2.56	-1.38	-3.45	-3.92	-1.60	-3.90	-12.89	-38.88	-78.19	-96.28	-95.39	-74.95	-35.98	-6.87	0.80	0.14	-5.49	-2.52	-4.04	-5.74	-4.90	-0.42	-2.26
-1.5D, h3, x1	-3.26	-0.33	-0.46	4.18	0.10	0.18	10.67	7.51	6.84	-21.80	-67.45	-95.38	-97.58	-85.05	-42.72	-2.38	5.70	0.62	4.54	-1.80	-3.64	-4.31	-5.75	-2.46	-0.95
-3.5D, h1, x1	0.40	-4.58	-0.43	0.07	-10.13	-10.42	-6.02	-8.97	-12.66	-15.38	-17.93	-19.94	-22.02	-18.08	-15.56	-15.02	-16.73	-16.34	-16.96	-17.88	-20.18	-19.47	-12.73	-13.69	-9.63
-3.5D, h2, x1	-1.43	-1.08	2.02	0.10	0.15	-3.29	-1.65	-4.36	-7.13	-10.86	-21.48	-47.13	-65.44	-49.96	-25.20	-5.41	-5.24	-4.99	-4.97	-5.07	-7.39	-5.00	-5.55	-2.48	-3.95
-3.5D, h3, x1	3.62	-3.03	-1.37	1.40	-10.63	-10.21	-4.26	-11.77	-20.00	-38.59	-67.64	-91.83	-98.24	-96.80	-81.73	-50.44	-20.17	-9.51	-6.58	-7.03	-8.07	-9.10	-4.53	-5.97	-3.42
-5.5D, h1, x1	-2.74	-7.94	-5.77	-10.57	-22.35	-26.43	-25.08	-26.24	-27.37	-25.80	-25.26	-22.04	-21.41	-17.75	-23.74	-24.37	-26.53	-29.41	-26.80	-32.99	-34.59	-28.05	-25.01	-17.68	-12.78
-5.5D, h2, x1	-2.04	-3.75	-1.30	-2.00	-12.18	-15.20	-14.60	-15.28	-18.76	-13.30	-11.81	-29.79	-34.83	-14.17	-6.76	-11.45	-11.32	-17.70	-14.45	-15.13	-14.62	-11.02	-7.89	-6.51	-5.17
-5.5D, h3, x1	-0.06	-3.32	-3.43	-4.73	-12.60	-16.31	-17.27	-16.94	-19.59	-15.65	-11.60	-40.32	-70.25	-51.87	-15.41	-13.88	-16.54	-16.82	-14.59	-13.44	-13.92	-12.78	-9.28	-7.24	-2.70
-1.5D, h1, x2	-0.47	-1.09	-3.05	-2.65	2.18	-2.91	-1.73	-3.48	-2.24	-2.83	-12.30	-33.88	-37.13	-18.27	-3.05	1.71	-4.07	-2.01	-0.70	1.35	-2.09	-3.08	-3.04	-3.89	3.36
-1.5D, h2, x2	4.10	-4.79	-1.52	-2.25	-0.83	-3.79	0.16	-6.99	-16.12	-42.21	-77.98	-96.20	-95.41	-76.45	-35.49	-7.07	-2.90	-0.56	-1.06	2.65	-1.71	-2.85	-5.95	-5.99	2.06
-1.5D, h3, x2	0.13	-3.34	0.34	-1.58	5.54	1.97	6.95	8.27	2.93	-21.77	-66.67	-95.13	-97.80	-86.03	-44.45	-2.12	2.32	1.81	4.53	-0.52	-3.13	-4.01	-6.53	-6.60	3.09
-3.5D, h1, x2	4.32	-1.90	-1.83	-1.35	-4.84	-8.13	-8.95	-11.31	-11.03	-12.87	-12.79	-19.06	-22.41	-18.04	-16.51	-12.97	-18.14	-14.34	-11.92	-17.72	-19.02	-16.43	-17.33	-17.75	-11.96
-3.5D, h2, x2	4.10	-1.29	-3.14	2.00	4.35	-5.64	-3.76	-4.96	-6.71	-10.28	-18.36	-44.63	-66.49	-51.17	-20.84	-8.78	-9.34	-2.52	-0.31	-2.89	-9.61	-4.24	-6.27	-8.34	-2.42
-3.5D, h3, x2	3.35	-1.64	-1.81	-4.18	-3.86	-11.38	-10.16	-11.70	-19.14	-39.11	-65.65	-91.10	-98.34	-96.21	-80.65	-47.70	-24.36	-7.88	-2.00	-5.51	-9.39	-7.86	-8.69	-9.47	0.21
-5.5D, h1, x2	-1.38	-6.70	-10.91	-14.48	-18.57	-26.19	-20.71	-25.48	-26.23	-26.72	-21.56	-22.77	-23.69	-21.28	-19.40	-26.52	-27.78	-29.47	-26.88	-30.20	-33.32	-28.68	-25.21	-20.97	-10.51
-5.5D, h2, x2	0.81	-3.68	-5.08	-6.90	-11.63	-19.80	-10.95	-21.35	-20.90	-15.01	-9.20	-26.46	-35.87	-14.73	-11.85	-8.64	-15.59	-16.91	-14.35	-13.22	-14.89	-12.21	-7.54	-11.11	-5.33
-5.5D, h3, x2	4.94	-4.15	-5.18	-7.58	-8.37	-18.00	-18.95	-19.08	-20.52	-19.80	-4.54	-38.80	-69.99	-51.06	-14.50	-14.52	-21.09	-12.41	-13.66	-18.14	-15.63	-12.04	-12.00	-10.38	-2.45
-1.5D, h1, x3	-3.06	3.47	-0.70	1.02	1.59	-0.93	-2.03	-1.87	-3.51	-2.01	-19.13	-33.21	-35.90	-18.28	-0.31	1.17	-1.84	0.34	-1.39	0.96	0.38	-2.61	-0.04	-2.68	-3.58
-1.5D, h2, x3	0.49	-0.31	3.09	-2.19	0.31	-3.49	-8.70	-5.13	-13.68	-41.81	-78.50	-96.26	-94.62	-76.05	-35.48	-6.60	-1.75	-2.69	-3.92	0.63	-5.40	-4.83	-3.07	-4.56	-5.44
-1.5D, h3, x3	-1.90	-0.63	5.50	3.67	3.82	5.59	4.30	8.42	3.22	-17.27	-69.81	-95.49	-97.65	-86.26	-42.76	-7.02	7.35	4.86	1.30	1.74	-0.67	-4.58	-2.72	-5.34	-0.89
-3.5D, h1, x3	1.71	1.47	2.43	0.52	-7.52	-7.19	-9.04	-6.83	-15.59	-16.56	-16.59	-17.89	-19.59	-19.64	-16.56	-15.84	-16.00	-17.99	-16.39	-16.10	-21.90	-17.65	-13.47	-17.42	-12.50
-3.5D, h2, x3	2.02	3.69	4.69	0.69	2.99	0.35	-4.64	-4.52	-4.01	-7.14	-20.45	-46.42	-63.78	-51.82	-19.47	-10.15	-0.39	-2.22	-5.50	-3.74	-6.80	-7.99	-2.80	-7.04	-6.55
-3.5D, h3, x3	-2.54	1.37	-0.31	-0.62	-3.49	-6.79	-11.97	-10.36	-18.36	-37.32	-68.44	-92.05	-98.27	-97.20	-80.57	-50.92	-17.04	-7.36	-4.36	-7.17	-9.73	-10.11	-4.96	-8.02	-4.78
-5.5D, h1, x3	-3.98	-4.80	-3.28	-10.81	-18.52	-25.49	-27.84	-25.18	-24.38	-24.17	-23.56	-25.19	-20.89	-20.16	-20.68	-27.56	-26.87	-24.71	-28.89	-33.31	-33.96	-27.59	-22.81	-23.29	-17.83
-5.5D, h2, x3	-3.61	-0.76	-2.01	-3.00	-8.92	-16.52	-19.83	-16.48	-17.41	-13.40	-12.99	-29.63	-32.41	-17.65	-11.57	-11.56	-13.32	-16.57	-14.01	-12.36	-17.10	-10.17	-8.89	-8.58	-10.30
-5.5D, h3, x3	2.57	-2.80	0.88	-6.15	-8.79	-17.00	-18.32	-17.57	-17.93	-14.03	-9.85	-41.48	-68.73	-53.60	-12.80	-14.36	-15.00	-14.13	-13.75	-13.40	-17.97	-12.57	-8.02	-8.60	-6.64
No Object, x1	0.00	0.00	0.00	0.00	0.00	0.00	0.00	0.00	0.00	0.00	0.00	0.00	0.00	0.00	0.00	0.00	0.00	0.00	0.00	0.00	0.00	0.00	0.00	0.00	0.00
No Object, x2	0.00	0.00	0.00	0.00	0.00	0.00	0.00	0.00	0.00	0.00	0.00	0.00	0.00	0.00	0.00	0.00	0.00	0.00	0.00	0.00	0.00	0.00	0.00	0.00	0.00
No Object, x3	0.00	0.00	0.00	0.00	0.00	0.00	0.00	0.00	0.00	0.00	0.00	0.00	0.00	0.00	0.00	0.00	0.00	0.00	0.00	0.00	0.00	0.00	0.00	0.00	0.00
-1.5D, h1, X_tot	-2.17	0.26	-1.26	-0.72	0.84	-1.63	-0.92	-2.57	-1.99	-1.92	-16.77	-35.19	-35.55	-18.09	-1.67	1.72	-2.07	-1.46	-1.31	-0.08	-0.03	-4.13	-2.83	-1.86	-0.70
-1.5D, h2, X_tot	1.15	-3.50	-0.33	-1.94	-1.32	-3.73	-3.38	-5.34	-14.23	-40.97	-78.22	-96.25	-95.14	-75.81	-35.65	-6.85	-1.28	-1.04	-3.49	0.25	-3.72	-4.47	-4.64	-3.66	-1.88
-1.5D, h3, X_tot	-1.68	-1.44	1.79	2.09	3.16	2.58	7.31	8.07	4.33	-20.28	-67.98	-95.33	-97.68	-85.78	-43.31	-3.84	5.12	2.43	3.45	-0.20	-2.48	-4.30	-5.00	-4.80	0.42
-3.5D, h1, X_tot	2.14	-1.67	0.05	-0.25	-7.49	-8.58	-8.00	-9.03	-13.09	-14.94	-15.77	-18.96	-21.34	-18.59	-16.21	-14.61	-16.96	-16.22	-15.09	-17.23	-20.37	-17.85	-14.51	-16.29	-11.36
-3.5D, h2, X_tot	1.56	0.44	1.19	0.93	2.50	-2.86	-3.35	-4.61	-5.95	-9.43	-20.10	-46.06	-65.23	-50.99	-21.84	-8.11	-4.99	-3.25	-3.59	-3.90	-7.93	-5.74	-4.87	-5.95	-4.31
-3.5D, h3, X_tot	1.48	-1.10	-1.16	-1.13	-5.99	-9.46	-8.80	-11.28	-19.17	-38.34	-67.24	-91.66	-98.28	-96.73	-80.98	-49.69	-20.52	-8.25	-4.31	-6.57	-9.06	-9.02	-6.06	-7.82	-2.66
-5.5D, h1, X_tot	-2.70	-6.48	-6.66	-11.96	-19.81	-26.04	-24.54	-25.63	-25.99	-25.56	-23.46	-23.33	-22.00	-19.73	-21.27	-26.15	-27.06	-27.86	-27.52	-32.17	-33.95	-28.11	-24.35	-20.64	-13.70
-5.5D, h2, X_tot	-1.61	-2.73	-2.80	-3.97	-10.91	-17.17	-15.13	-17.71	-19.02	-13.90	-11.34	-28.63	-34.37	-15.52	-10.06	-10.55	-13.41	-17.06	-14.27	-13.57	-15.54	-11.13	-8.11	-8.73	-6.93
-5.5D, h3, X_tot	2.48	-3.42	-2.58	-6.15	-9.92	-17.10	-18.18	-17.86	-19.35	-16.49	-8.67	-40.20	-69.66	-52.18	-14.24	-14.26	-17.54	-14.45	-14.00	-14.99	-15.84	-12.46	-9.77	-8.74	-3.93
No Object, X_tot	0.00	0.00	0.00	0.00	0.00	0.00	0.00	0.00	0.00	0.00	0.00	0.00	0.00	0.00	0.00	0.00	0.00	0.00	0.00	0.00	0.00	0.00	0.00	0.00	0.00

Table B.2: Summary of values for the diameter of bubbles for different configurations.

Configuration	Z1	Z2	Z3	Z4	Z5	Z6	Z7	Z8	Z9	Z10	Z11	Z12	Z13	Z14	Z15	Z16	Z17	Z18	Z19	Z20	Z21	Z22	Z23	Z24	Z25
-1.5D, h1, x1	-0.09	-0.31	-0.14	-0.11	0.28	-0.01	0.36	0.17	0.25	-1.80	-2.38	-3.30	-3.30	-3.63	-1.53	0.13	0.16	0.52	-0.19	-0.20	0.05	0.40	0.09	0.20	1.16
-1.5D, h2, x1	-0.73	-0.94	-0.67	-0.75	0.11	-0.69	-0.59	-0.58	-0.63	-4.04	-5.58	-4.47	-4.25	-5.17	-2.72	-1.36	-0.63	0.01	0.34	0.40	0.13	-0.16	-0.32	0.35	0.84
-1.5D, h3, x1	-0.13	-0.77	-0.78	-0.59	1.08	0.72	1.17	0.23	-0.24	-3.30	-4.99	-0.34	0.12	-3.75	-4.27	-1.55	0.54	1.14	0.43	0.44	0.28	0.46	-0.14	-0.33	0.41
-3.5D, h1, x1	-0.25	-0.21	-1.16	-1.64	-0.69	-0.61	-0.15	-1.35	-1.13	-1.70	-1.90	-2.32	-1.96	-3.80	-2.25	-1.90	-1.71	-1.20	-0.85	-1.43	-1.06	-0.18	-0.98	-0.63	0.62
-3.5D, h2, x1	0.25	-0.72	-0.28	0.14	0.92	0.03	0.36	-0.13	-0.60	-2.47	-3.71	-4.48	-0.93	-4.05	-3.92	-2.69	-1.27	-0.13	-0.14	-1.10	-0.53	-0.31	-0.30	0.02	0.63
-3.5D, h3, x1	1.33	0.48	0.55	0.10	1.03	0.82	0.69	0.13	-0.87	-3.90	-6.33	-4.52	2.92	-4.02	-6.50	-4.16	-1.79	0.36	0.40	0.32	0.61	0.19	0.70	0.79	1.32
-5.5D, h1, x1	-1.69	-2.33	-2.66	-3.14	-1.94	-2.26	-2.48	-3.12	-2.85	-4.02	-3.28	-3.72	-3.20	-4.39	-3.57	-3.58	-4.13	-2.71	-2.61	-2.78	-2.65	-2.81	-2.16	-1.52	-1.02
-5.5D, h2, x1	1.34	0.43	0.13	-0.03	0.51	-0.10	-0.39	-1.32	-0.87	-2.15	-2.79	-0.37	0.04	-3.17	-2.70	-1.94	-1.14	0.23	-0.89	-0.43	0.02	0.41	0.28	0.37	0.53
-5.5D, h3, x1	0.65	0.65	0.43	-0.48	0.59	-0.34	-0.32	-1.23	-0.47	-2.39	-3.51	0.27	7.10	1.17	-3.82	-2.86	-1.68	-0.21	-0.61	-0.55	0.11	-0.06	-0.13	0.61	1.56
-1.5D, h1, x2	-0.23	-0.57	-0.39	-0.17	0.05	0.47	-0.12	0.48	-0.26	-0.52	-2.45	-3.29	-3.09	-2.14	-1.38	-0.11	0.45	0.45	0.43	-0.06	-0.81	0.27	0.70	0.01	0.96
-1.5D, h2, x2	-0.76	-0.62	-0.60	-0.79	-0.53	-0.34	-0.37	-0.61	-1.27	-2.81	-6.03	-3.09	-4.77	-4.70	-2.93	-1.35	-0.13	0.75	0.67	-0.02	-0.35	0.46	0.48	-0.08	0.98
-1.5D, h3, x2	-0.21	-0.63	-0.68	-0.15	0.18	1.49	1.25	0.48	-0.43	-2.74	-6.19	-3.30	4.93	-3.12	-4.46	-1.19	0.72	1.67	0.72	0.36	0.01	-0.27	0.84	-0.03	0.00
-3.5D, h1, x2	0.17	-0.50	-1.00	-0.87	-0.44	0.19	0.39	-0.65	-0.98	-1.12	-2.28	-2.61	-2.13	-2.56	-2.97	-2.30	-1.15	-0.86	-1.51	-1.57	-1.18	-0.85	0.13	-0.77	0.38
-3.5D, h2, x2	-0.05	-0.18	0.21	0.09	0.08	0.45	-0.21	-0.31	-0.48	-1.55	-4.15	-4.01	-2.29	-4.33	-4.09	-1.53	-0.43	-0.31	-0.09	-0.50	-0.75	0.07	0.68	0.00	0.09
-3.5D, h3, x2	0.73	0.59	1.08	0.90	0.57	1.61	0.72	0.18	-1.21	-2.91	-7.72	-5.36	3.16	-3.61	-6.70	-2.96	-0.83	0.60	0.54	0.23	-0.02	0.37	1.34	0.73	1.22
-5.5D, h1, x2	-1.62	-2.68	-2.61	-2.38	-2.65	-2.48	-3.13	-2.49	-3.16	-2.24	-3.62	-3.94	-3.79	-3.55	-4.35	-3.52	-3.42	-2.47	-2.33	-2.86	-3.25	-2.79	-1.90	-2.19	-0.92
-5.5D, h2, x2	0.45	0.52	0.37	0.68	0.34	0.39	-0.82	-1.43	-1.28	-1.39	-2.44	-0.36	1.31	-3.10	-2.89	-1.60	-0.88	-0.33	0.07	-0.02	-0.55	-0.02	0.84	0.25	1.19
-5.5D, h3, x2	0.63	0.50	0.52	0.21	-0.28	0.57	-0.12	-1.15	-1.70	-1.32	-3.79	0.54	7.98	2.33	-4.32	-2.79	-0.61	-0.32	-0.25	-0.45	-0.02	0.79	1.05	0.65	0.91
-1.5D, h1, x3	0.35	-0.09	0.01	-0.29	-0.47	0.08	-0.02	0.30	0.17	-1.31	-2.33	-2.68	-3.20	-3.51	-1.48	-0.01	0.19	0.00	0.19	-0.01	-0.40	0.48	0.40	0.66	0.05
-1.5D, h2, x3	0.22	-1.14	-0.81	-0.57	-1.28	0.43	-0.35	-0.25	-1.12	-3.99	-5.35	-3.34	-4.85	-4.70	-2.87	-0.50	-0.51	-0.08	0.19	0.02	-0.17	0.10	0.29	0.93	0.43
-1.5D, h3, x3	0.30	-0.39	-0.82	-0.30	-0.15	0.57	0.31	0.64	-0.81	-3.33	-5.37	-2.55	2.75	-3.26	-3.79	-0.58	0.52	0.75	0.68	0.20	0.44	0.41	0.06	0.22	0.03
-3.5D, h1, x3	0.52	-0.07	-0.86	-1.09	-0.97	0.07	-0.65	-0.88	-0.78	-1.26	-2.40	-2.61	-2.17	-3.02	-2.75	-1.57	-1.55	-1.63	-1.21	-1.13	-0.92	-0.13	0.22	0.31	-0.01
-3.5D, h2, x3	0.31	0.07	0.11	0.19	0.00	0.60	-0.34	-0.31	-0.86	-2.04	-4.27	-3.73	-1.92	-3.81	-3.68	-1.42	-1.17	-0.51	-0.38	-0.99	-1.33	0.16	0.13	0.65	0.34
-3.5D, h3, x3	1.61	1.04	0.94	1.09	0.23	1.26	0.07	0.19	-0.37	-3.32	-6.90	-4.89	6.46	-4.65	-6.92	-3.74	-1.43	-0.31	0.38	0.43	0.87	0.82	1.04	0.74	1.09
-5.5D, h1, x3	-1.92	-2.12	-2.51	-2.66	-3.39	-2.02	-3.61	-2.98	-2.78	-3.69	-3.46	-3.04	-3.83	-3.76	-3.32	-3.03	-3.86	-3.99	-2.68	-2.59	-3.05	-2.33	-2.24	-0.98	-0.86
-5.5D, h2, x3	1.34	0.67	0.30	-0.13	-0.40	0.63	-0.40	-0.72	-0.89	-1.81	-2.97	-0.48	0.03	-2.94	-2.53	-1.06	-1.16	-0.54	-0.28	-0.04	-0.20	0.17	0.58	0.45	0.44
-5.5D, h3, x3	0.86	0.22	-0.08	-0.04	-0.59	0.23	-0.19	-0.11	-1.14	-2.11	-4.33	0.86	7.65	1.39	-3.87	-2.65	-1.80	-0.99	0.01	0.08	0.25	0.31	0.14	0.87	1.21
No Object, x1	0.00	0.00	0.00	0.00	0.00	0.00	0.00	0.00	0.00	0.00	0.00	0.00	0.00	0.00	0.00	0.00	0.00	0.00	0.00	0.00	0.00	0.00	0.00	0.00	0.00
No Object, x2	0.00	0.00	0.00	0.00	0.00	0.00	0.00	0.00	0.00	0.00	0.00	0.00	0.00	0.00	0.00	0.00	0.00	0.00	0.00	0.00	0.00	0.00	0.00	0.00	0.00
No Object, x3	0.00	0.00	0.00	0.00	0.00	0.00	0.00	0.00	0.00	0.00	0.00	0.00	0.00	0.00	0.00	0.00	0.00	0.00	0.00	0.00	0.00	0.00	0.00	0.00	0.00
-1.5D, h1, X_tot	0.01	-0.32	-0.17	-0.19	-0.05	0.18	0.07	0.32	0.05	-1.21	-2.38	-3.09	-3.20	-3.09	-1.46	0.00	0.27	0.33	0.15	-0.09	-0.39	0.38	0.40	0.29	0.72
-1.5D, h2, X_tot	-0.42	-0.90	-0.69	-0.70	-0.57	-0.20	-0.43	-0.48	-1.01	-3.61	-5.65	-3.64	-4.62	-4.86	-2.84	-1.07	-0.42	0.23	0.40	0.13	-0.13	0.13	0.15	0.40	0.75
-1.5D, h3, X_tot	-0.01	-0.60	-0.76	-0.35	0.37	0.93	0.91	0.45	-0.49	-3.13	-5.52	-2.06	2.60	-3.38	-4.17	-1.11	0.59	1.19	0.61	0.33	0.24	0.20	0.25	-0.05	0.15
-3.5D, h1, X_tot	0.15	-0.26	-1.01	-1.20	-0.70	-0.12	-0.14	-0.96	-0.97	-1.36	-2.20	-2.51	-2.08	-3.13	-2.66	-1.92	-1.47	-1.23	-1.19	-1.38	-1.05	-0.39	-0.21	-0.37	0.33
-3.5D, h2, X_tot	0.17	-0.28	0.01	0.14	0.33	0.36	-0.06	-0.25	-0.65	-2.02	-4.04	-4.07	-1.72	-4.06	-3.90	-1.88	-0.96	-0.32	-0.20	-0.86	-0.87	-0.03	0.17	0.22	0.35
-3.5D, h3, X_tot	1.23	0.71	0.86	0.70	0.61	1.23	0.49	0.17	-0.82	-3.38	-6.98	-4.92	4.18	-4.09	-6.71	-3.62	-1.35	0.22	0.44	0.32	0.49	0.46	1.03	0.75	1.21
-5.5D, h1, X_tot	-1.74	-2.38	-2.60	-2.72	-2.66	-2.25	-3.07	-2.86	-2.93	-3.32	-3.45	-3.56	-3.61	-3.90	-3.75	-3.38	-3.80	-3.06	-2.54	-2.75	-2.99	-2.64	-2.10	-1.56	-0.93
-5.5D, h2, X_tot	1.04	0.54	0.27	0.18	0.15	0.31	-0.54	-1.15	-1.01	-1.78	-2.74	-0.40	0.46	-3.07	-2.71	-1.53	-1.06	-0.21	-0.37	-0.16	-0.24	0.18	0.57	0.36	0.72
-5.5D, h3, X_tot	0.71	0.46	0.29	-0.10	-0.09	0.15	-0.21	-0.83	-1.10	-1.94	-3.87	0.56	7.58	1.63	-4.01	-2.77	-1.36	-0.51	-0.28	-0.31	0.11	0.35	0.36	0.71	1.23
No Object, X_tot	0.00	0.00	0.00	0.00	0.00	0.00	0.00	0.00	0.00	0.00	0.00	0.00	0.00	0.00	0.00	0.00	0.00	0.00	0.00	0.00	0.00	0.00	0.00	0.00	0.00

Table B.3: Summary of values for the streamwise velocity of bubbles for different configurations.

Configuration	Z1	Z2	Z3	Z4	Z5	Z6	Z7	Z8	Z9	Z10	Z11	Z12	Z13	Z14	Z15	Z16	Z17	Z18	Z19	Z20	Z21	Z22	Z23	Z24	Z25
-1.5D, h1, x1	17.24	-7.77	9.10	12.74	27.48	-1.41	-11.72	28.40	56.39	-23.41	-0.61	18.39	76.65	-331.80	-127.36	-176.08	50.42	-85.22	7.06	32.53	-16.86	-4.64	1.70	-2.40	8.01
-1.5D, h2, x1	5.72	-2.90	7.14	23.51	-9.04	-5.32	6.45	25.88	-2.81	-76.41	-204.81	-570.36	1059.42	-1241.43	-507.97	-125.50	-89.53	-36.11	-54.44	44.03	5.96	-18.65	9.90	-7.28	13.16
-1.5D, h3, x1	-12.20	-7.91	-3.74	13.38	7.02	6.66	-2.35	55.63	15.86	-51.91	-184.83	-598.16	1400.58	-1437.68	-484.79	-290.94	51.65	-46.36	-22.03	38.86	6.77	1.96	12.49	-13.26	5.57
-3.5D, h1, x1	-3.68	-22.92	-14.33	12.94	-11.23	-13.13	-28.06	3.53	15.63	-52.72	19.47	-31.08	-66.86	-134.10	-17.51	-139.59	42.70	-70.97	18.17	31.68	-24.39	-15.46	-17.59	-7.97	12.44
-3.5D, h2, x1	-6.53	-11.34	-7.95	12.11	-3.81	-9.78	-13.62	30.14	63.89	-37.45	30.05	29.52	139.93	-450.02	-310.27	-66.66	11.21	-31.87	-2.41	72.27	-5.39	-15.14	-9.52	-5.29	3.86
-3.5D, h3, x1	3.41	2.68	-11.05	14.38	14.01	-4.42	-9.70	3.66	4.98	-30.87	-42.69	-80.23	-575.34	-1228.48	-1164.18	-674.70	-260.32	-55.88	-8.59	28.14	-0.62	-6.11	18.46	-13.35	-1.36
-5.5D, h1, x1	-10.29	-0.27	-14.13	-11.49	-12.41	-14.87	-16.53	-24.21	17.23	-17.61	33.26	-17.04	-75.84	-189.82	13.37	-164.80	-9.01	-6.98	-10.63	24.76	-17.20	-20.84	-7.98	-18.14	-13.03
-5.5D, h2, x1	5.63	-9.56	-3.16	-6.94	-6.98	-0.18	-13.26	-2.69	54.37	-3.62	87.59	45.47	-81.23	69.77	-19.50	-192.55	199.21	-24.82	-7.53	28.77	-28.50	0.80	8.39	-25.36	4.38
-5.5D, h3, x1	-2.25	-6.22	-10.30	24.80	6.07	3.79	-18.34	24.28	85.65	22.71	88.12	183.02	184.02	-45.45	54.13	122.66	125.02	-41.05	2.71	23.59	24.98	5.02	10.25	-5.83	-2.83
-1.5D, h1, x2	0.44	-11.97	7.44	5.38	1.91	-2.55	25.39	19.22	-17.76	-34.02	11.78	-27.44	-895.31	283.96	-114.51	-143.13	-60.97	23.48	-24.87	65.02	-2.69	-13.25	-14.06	22.82	18.30
-1.5D, h2, x2	-8.84	-12.04	4.66	6.40	8.71	-6.74	30.27	18.29	-37.54	-87.73	-210.38	-606.97	-2516.89	2172.01	-444.11	-213.72	-41.05	-29.33	-1.30	18.84	-5.22	-10.61	11.50	-7.55	33.05
-1.5D, h3, x2	-7.50	-8.41	2.99	12.84	9.43	-3.34	28.73	34.70	5.75	-65.22	-192.28	-873.73	-3472.28	2376.69	-503.18	-205.92	-13.98	9.79	-15.85	3.68	10.91	-7.83	-6.68	-10.93	17.81
-3.5D, h1, x2	-13.19	-25.17	0.87	2.73	-12.70	-12.53	10.33	-9.02	6.90	-13.86	33.28	-27.27	-132.01	-62.35	-91.48	-55.62	47.25	-60.05	-42.38	59.78	17.37	-14.33	-21.29	-16.19	-10.00
-3.5D, h2, x2	-10.29	-4.14	4.38	10.44	-1.35	-20.96	22.91	30.19	0.79	-10.87	60.23	3.25	-543.28	429.32	-291.70	-74.83	-21.63	-27.40	-33.30	59.81	-19.73	-25.21	-14.69	-19.26	-5.16
-3.5D, h3, x2	-8.41	-1.20	14.10	15.02	-2.54	-13.50	18.52	21.29	-3.20	-60.21	-123.83	-295.36	1334.90	1709.91	-660.02	-440.78	-65.31	-6.09	0.27	68.25	-0.67	7.64	3.09	-7.29	-6.50
-5.5D, h1, x2	-4.23	-16.23	-6.93	-13.61	4.75	-24.48	37.99	12.39	16.31	-10.91	35.40	-34.08	-284.48	-144.90	-28.88	-36.15	-3.92	-44.83	-8.62	82.26	-10.73	0.48	2.98	-4.02	1.14
-5.5D, h2, x2	7.83	2.98	17.04	-0.96	-3.66	-16.90	32.66	13.71	27.63	17.28	100.44	117.13	-239.64	-365.06	-70.09	-87.89	-64.50	-25.91	-6.81	59.64	10.02	-9.58	-6.09	21.14	-0.51
-5.5D, h3, x2	-0.28	-2.65	0.95	3.73	8.41	-6.93	10.08	36.58	11.04	30.71	121.61	269.56	-1154.73	-8.38	13.83	-46.63	-32.80	26.66	6.00	45.00	12.65	-2.95	2.04	-9.07	25.21
-1.5D, h1, x3	-2.84	5.63	-8.08	0.16	7.48	9.53	-10.86	18.37	56.88	13.61	-55.78	-62.05	-452.62	-459.96	60.44	-605.17	-91.68	-46.74	1.63	-16.70	14.85	-3.24	3.68	3.42	3.04
-1.5D, h2, x3	-11.92	-9.25	-16.96	-5.96	12.03	7.41	-10.44	2.86	11.72	-74.52	-182.75	-337.86	-1699.08	-1374.49	748.48	-1218.67	-9.06	-14.74	-34.51	4.51	6.38	-10.81	-27.19	-8.24	-2.71
-1.5D, h3, x3	-7.77	4.50	-4.46	12.12	23.64	0.22	-11.78	42.78	62.48	-24.08	-137.96	-348.39	-2674.43	-946.71	720.55	-5781.53	-18.45	-10.47	19.24	-33.12	27.84	9.66	-18.51	7.29	-8.20
-3.5D, h1, x3	-20.11	-17.98	-22.83	-30.00	13.37	4.14	-31.51	21.22	25.00	-38.26	-16.49	-54.34	-168.68	63.26	-38.91	1133.57	-104.80	-109.59	-34.96	-26.33	6.41	-27.04	-19.08	-7.06	-20.69
-3.5D, h2, x3	-14.12	-8.76	-1.89	3.65	17.42	11.04	-23.06	-9.50	20.81	-17.02	-10.90	-53.92	-262.59	-333.94	215.09	205.80	35.09	-21.92	-27.87	-11.41	23.49	7.21	-23.10	0.30	-18.11
-3.5D, h3, x3	-5.63	-2.48	-9.44	-7.06	11.86	11.94	-16.60	11.50	37.91	-80.21	-128.38	-206.01	568.80	-1321.77	1379.12	-23401.86	-148.62	-34.46	-17.89	11.38	-2.60	17.72	-15.77	5.40	-3.05
-5.5D, h1, x3	-15.92	-14.96	-12.96	-15.07	1.01	0.53	-27.33	24.43	35.58	-19.24	-22.57	0.42	-362.79	-101.73	22.99	5215.48	36.90	-111.37	-49.00	12.89	44.71	2.01	-29.72	-12.13	-12.22
-5.5D, h2, x3	-9.09	-2.42	-4.19	-3.37	-0.57	6.33	-31.19	12.90	13.65	9.61	46.65	27.70	-175.07	-41.95	-392.86	1839.26	-37.33	-88.43	-17.86	14.19	35.86	10.42	-10.41	-0.48	-17.01
-5.5D, h3, x3	13.61	2.75	2.54	1.50	-1.52	5.69	7.98	23.51	70.30	34.66	95.41	79.31	-296.84	-69.69	-398.73	9422.47	94.79	2.60	0.62	12.62	30.24	21.29	-2.06	16.29	-11.37
No Object, x1	0.00	0.00	0.00	0.00	0.00	0.00	0.00	0.00	0.00	0.00	0.00	0.00	0.00	0.00	0.00	0.00	0.00	0.00	0.00	0.00	0.00	0.00	0.00	0.00	0.00
No Object, x2	0.00	0.00	0.00	0.00	0.00	0.00	0.00	0.00	0.00	0.00	0.00	0.00	0.00	0.00	0.00	0.00	0.00	0.00	0.00	0.00	0.00	0.00	0.00	0.00	0.00
No Object, x3	0.00	0.00	0.00	0.00	0.00	0.00	0.00	0.00	0.00	0.00	0.00	0.00	0.00	0.00	0.00	0.00	0.00	0.00	0.00	0.00	0.00	0.00	0.00	0.00	0.00
-1.5D, h1, X_tot	4.95	-4.70	2.82	6.09	12.29	1.86	0.94	22.00	31.84	-14.61	-14.87	-23.70	-423.76	-169.27	-60.48	-308.13	-34.08	-36.16	-5.39	26.95	-1.57	-7.04	-2.90	7.95	9.79
-1.5D, h2, X_tot	-5.01	-8.06	-1.72	7.98	3.90	-1.55	8.76	15.68	-9.54	-79.55	-199.31	-505.06	-1052.18	-147.97	-67.87	-519.30	-46.55	-26.72	-30.08	22.46	2.37	-13.36	-1.93	-7.69	14.50
-1.5D, h3, X_tot	-9.16	-3.94	-1.74	12.78	13.36	1.18	4.87	44.37	28.03	-47.07	-171.69	-606.76	-1582.04	-2.57	-89.14	-2092.80	6.41	-15.68	-6.21	3.14	15.17	1.26	-4.23	-5.63	5.06
-3.5D, h1, X_tot	-12.32	-22.02	-12.10	-4.78	-3.52	-7.17	-16.41	5.24	15.84	-34.95	12.09	-37.57	-122.52	-44.40	-49.30	312.79	-4.95	-80.20	-19.72	21.71	-0.21	-18.94	-19.32	-10.41	-6.08
-3.5D, h2, X_tot	-10.31	-8.08	-1.82	8.73	4.09	-6.56	-4.59	16.94	28.50	-21.78	26.46	-7.05	-221.98	-118.21	-128.96	21.43	8.22	-27.06	-21.19	40.22	-0.55	-11.04	-15.77	-8.08	-6.47
-3.5D, h3, X_tot	-3.55	-0.33	-2.13	7.45	7.78	-1.99	-2.59	12.15	13.23	-57.10	-98.30	-193.87	442.79	-280.11	-148.36	-8172.45	-158.08	-32.14	-8.74	35.92	-1.30	6.42	1.93	-5.08	-3.64
-5.5D, h1, X_tot	-10.14	-10.48	-11.34	-13.39	-2.22	-12.94	-1.96	4.20	23.04	-15.92	15.36	-16.90	-241.03	-145.49	2.49	1671.51	7.99	-54.39	-22.75	39.97	5.59	-6.12	-11.57	-11.43	-8.04
-5.5D, h2, X_tot	1.46	-3.00	3.23	-3.76	-3.74	-3.58	-3.93	7.98	31.88	7.76	78.23	63.43	-165.31	-112.41	-160.82	519.60	32.46	-46.38	-10.73	34.20	5.79	0.55	-2.70	-1.57	-4.38
-5.5D, h3, X_tot	3.69	-2.04	-2.27	10.01	4.32	0.85	-0.09	28.12	55.66	29.36	101.71	177.30	-422.51	-41.17	-110.26	3166.17	62.34	-3.93	3.11	27.07	22.63	7.79	3.41	0.47	3.67
No Object, X_tot	0.00	0.00	0.00	0.00	0.00	0.00	0.00	0.00	0.00	0.00	0.00	0.00	0.00	0.00	0.00	0.00	0.00	0.00	0.00	0.00	0.00	0.00	0.00	0.00	0.00

Table B.4: Summary of values for the spanwise velocity of bubbles for different configurations.

Configuration	Number of Bubbles	Diameter of Bubbles	Streamwise Velocity	Spanwise Velocity
-1.5D, h1, x1	-5.47	-2.59	-0.53	-17.73
-1.5D, h2, x1	-19.49	-6.63	-1.28	-70.06
-1.5D, h3, x1	-15.80	0.68	-0.57	-61.59
-3.5D, h1, x1	-12.81	-12.76	-1.22	-20.60
-3.5D, h2, x1	-11.47	-5.84	-1.02	-23.76
-3.5D, h3, x1	-26.23	-11.23	-0.77	-163.13
-5.5D, h1, x1	-21.95	-15.68	-2.82	-23.38
-5.5D, h2, x1	-12.44	-10.02	-0.56	3.14
-5.5D, h3, x1	-16.82	-9.63	-0.22	34.34
-1.5D, h1, x2	-5.41	-2.28	-0.45	-35.10
-1.5D, h2, x2	-19.17	-6.17	-1.15	-77.45
-1.5D, h3, x2	-16.07	1.43	-0.43	-114.95
-3.5D, h1, x2	-12.17	-12.00	-1.08	-17.64
-3.5D, h2, x2	-11.26	-5.18	-0.94	-20.10
-3.5D, h3, x2	-26.17	-10.68	-0.67	59.92
-5.5D, h1, x2	-21.82	-15.38	-2.81	-19.33
-5.5D, h2, x2	-13.30	-9.47	-0.43	-18.80
-5.5D, h3, x2	-17.12	-8.86	-0.02	-25.61
-1.5D, h1, x3	-4.97	-2.55	-0.52	-64.68
-1.5D, h2, x3	-19.60	-6.81	-1.17	-170.23
-1.5D, h3, x3	-15.33	0.89	-0.54	-363.82
-3.5D, h1, x3	-12.49	-12.44	-1.06	19.13
-3.5D, h2, x3	-10.44	-5.50	-0.97	-11.93
-3.5D, h3, x3	-26.05	-10.71	-0.57	-933.85
-5.5D, h1, x3	-21.83	-15.63	-2.83	183.60
-5.5D, h2, x3	-13.16	-10.14	-0.48	47.37
-5.5D, h3, x3	-16.40	-9.42	-0.15	366.32
No Object, x1	0.00	0.00	0.00	0.00
No Object, x2	0.00	0.00	0.00	0.00
No Object, x3	0.00	0.00	0.00	0.00
-1.5D, h1, X_tot	-5.28	-2.48	-0.50	-39.17
-1.5D, h2, X_tot	-19.42	-6.54	-1.20	-105.91
-1.5D, h3, X_tot	-15.73	1.00	-0.51	-180.12
-3.5D, h1, X_tot	-12.49	-12.40	-1.12	-6.37
-3.5D, h2, X_tot	-11.06	-5.51	-0.98	-18.60
-3.5D, h3, X_tot	-26.15	-10.88	-0.67	-345.68
-5.5D, h1, X_tot	-21.87	-15.56	-2.82	46.96
-5.5D, h2, X_tot	-12.97	-9.88	-0.49	10.57
-5.5D, h3, X_tot	-16.78	-9.30	-0.13	125.02
No Object, X_tot	0.00	0.00	0.00	0.00